



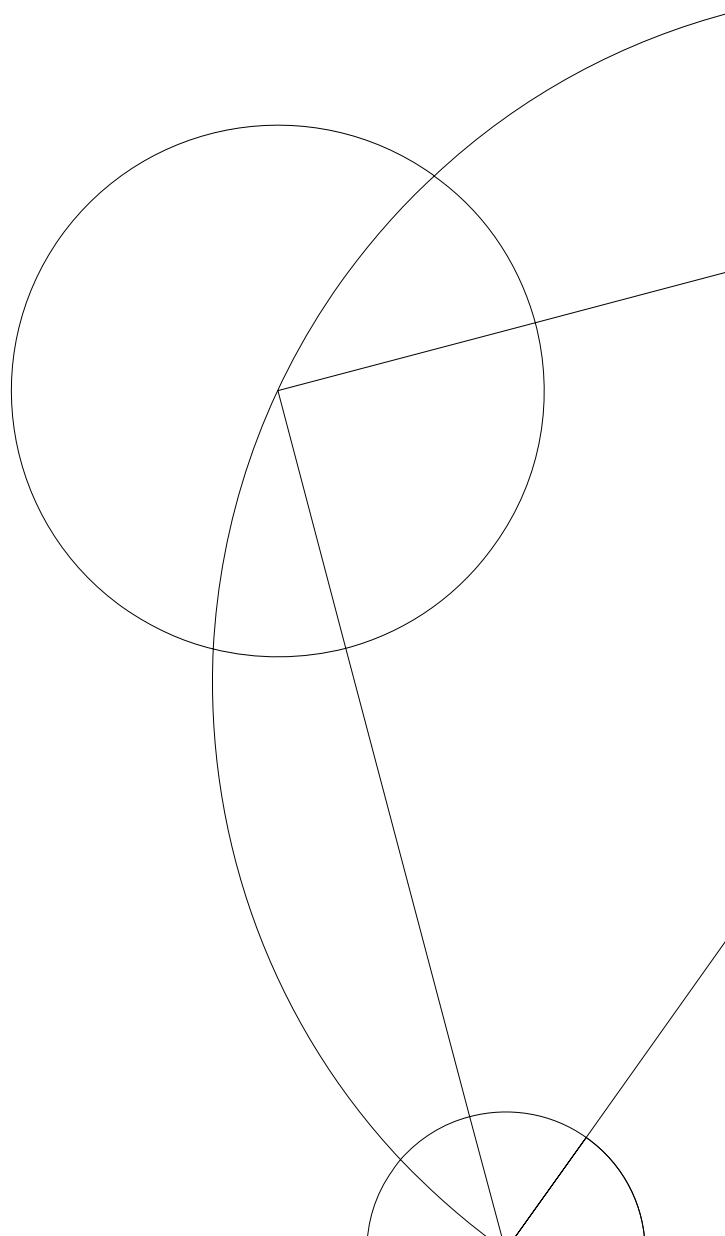
Theoretical Studies of Superconductivity in Sr_2RuO_4

Mercè Roig Server

Niels Bohr Institute
University of Copenhagen
Jagtvej 155, 2200 Copenhagen, Denmark

Master's thesis in Physics
Supervisor: Brian Møller Andersen

Date: May 20, 2021



Abstract

Recent experimental studies have challenged the previous agreement on p -wave spin-triplet superconductivity in Sr_2RuO_4 , leading to the appearance of new exotic proposals constrained by the reported measurements. In this thesis, we construct a three-orbital model adequate to describe superconductivity in Sr_2RuO_4 , including the effect of spin-orbit coupling. Initially, superconductivity is assumed to originate from an on-site attraction, and we solve self-consistently for the order parameter both in momentum and real space. In the latter case, we show that the inclusion of impurities induces an effect far from the defect. A more realistic model is achieved by including the pairings from a spin-fluctuation mechanism. In this case, a thorough study in momentum space is performed, fully classifying the superconducting phases based on a point group theory analysis. We observe a coexistence of a dominant A_{1g} with a subleading B_{1g} irreducible representation below the critical temperature for all Hund's coupling considered, contradicting the previous proposal of an accidental degeneracy. In addition, in agreement with the experimental observations, we find that the previous state breaks time-reversal symmetry, and the dominant solution corresponds to a spin-singlet character. Furthermore, nodes have been observed at the Fermi surface, and the specific heat has been calculated, showing only one phase transition.

Acknowledgments

First of all, I would like to thank my supervisor, Brian Møller Andersen, for his guidance and discussions throughout this year, and for always being ambitious in my project, inspiring me to give my best everyday. Thank you also for encouraging me when I was stuck, showing me the importance of reducing, reducing and reducing, until, surprisingly, the source of the problem always materializes.

I would also like to thank Astrid T. Rømer for enlightening discussions, always encouraging me and answering all my questions, I have really enjoyed all of our meetings. In addition, I want to express my gratitude to Daniel Steffensen for his patience and help in the beginning of the thesis, and to Clara N. Breiø for her advice, especially with my programs in Python.

I would also like to show my appreciation to all my friends, in particular to Alba Torras, Carla Muñoz and Raúl Morral for the comments on the thesis, to Carlos Ruiz for the nice discussions about programming, and also to Santiago Vallés and Marta Carrizo. Thank you all for your emotional support and for the weekly video calls in the last two years.

I would like to express my sincere gratitude to my mother, father, and brother, for their love and encouragement, and for giving me the opportunity to study abroad, always showing interest in my project. Thank you also for always making me feel home when I go back, in particular during the difficult lockdown period.

Last but not least, I would like to thank Roger Morales for the careful proofreading, but more importantly for the never-ending patience and motivation, specially in the last two years and during the lockdown, making me smile everyday. Thank you.

Contents

1	Introduction	1
2	Introduction to Sr_2RuO_4	3
2.1	Electronic structure and multi-orbital physics	4
2.2	Superconductivity in Sr_2RuO_4	6
2.2.1	The role of spin-orbit coupling	7
2.3	Experiments	7
2.3.1	Knight shift	8
2.3.2	Muon spin relaxation and polar Kerr effect	9
2.3.3	Specific heat	10
2.3.4	Scanning tunneling microscopy	11
2.3.5	Summary of the experimental constrains	12
3	Model and motivation	13
3.1	Fermi surface	16
3.2	Linearized gap equation	17
4	BCS theory for multi-orbital systems	19
4.1	Hamiltonian and mean-field treatment	19
4.2	Self-consistent calculations	22
4.3	Numerical implementation	24
5	Systems with on-site interactions	27
5.1	One-band model	28
5.2	Two-band model	30
5.3	Three-band model: effective model for Sr_2RuO_4	33
5.3.1	Point group symmetry for Sr_2RuO_4	38
5.3.2	Irreducible representations of the superconducting order parameter	40

6	Systems with off-site interactions	48
6.1	One-band model	50
7	Spin-fluctuation mediated pairing	55
7.1	Identification of the irreducible representations	58
7.2	Superconducting order parameter in terms of the basis functions for the different neighbors	62
7.2.1	Nearest neighbors	62
7.2.2	Further neighbors	63
7.3	Entropy and specific heat	65
8	Results from spin-fluctuation mediated pairing	67
8.1	Results for the different neighbors	67
8.1.1	Numerical implementation	67
8.1.2	Inclusion of first neighbors	68
8.1.3	Inclusion of up to third neighbors	71
8.1.4	Inclusion of up to sixth neighbors with on-site interactions	73
8.2	Comparison with the linearized gap equation	75
8.3	Effect of spin-orbit coupling	76
8.4	Nodal structure	78
8.5	Time-reversal symmetry	81
8.6	Specific heat	82
8.7	Effect of the boost	84
9	Conclusions and outlook	87
9.1	Conclusions	87
9.2	Outlook	88
A	On-site superconductivity in a one-band model using the spinor notation	93
B	SU(2) Generators and SU(3) Generators	95
C	Character table and product table for the point group D_{4h}	97
D	Representation in Nambu space	99
E	Order parameter for further neighbors	102
F	Nodal structure for different Hund's couplings	107

Chapter 1

Introduction

Superconductivity in strontium ruthenate (Sr_2RuO_4) was discovered in 1994 [1] and, despite the research efforts in the last two decades, the superconducting state seems to remain a mystery. Nevertheless, in the recent years, new experimental evidence has revealed important information constraining its superconducting state, which could lead to a final agreement between all the pieces in this fascinating puzzle.

Soon after the discovery of this material, the superconducting state was thought to be similar to the case of superfluid helium-3 [2, 3], representing one of the few examples known where the Cooper pairs are bound in spin triplets. The first evidences suggested an agreement with this proposal [4, 5], and therefore a lot of theoretical and experimental studies were devoted to confirm this superconducting state. Nonetheless, recent measurements challenged the previous results proving the existence of singlet pairing in Sr_2RuO_4 [6], and the advances in experimental techniques have made possible new observations that have increased even more the controversy. Hence, several measurements seemed to point towards different explanations for the superconducting state, making it challenging to propose a solution reconciling with all evidences.

In particular, theoretical studies in Sr_2RuO_4 are extremely involved due to the multi-orbital nature of the electronic states, with three orbitals contributing to the superconducting state [7]. Moreover, the role of spin-orbit coupling in this material cannot be disregarded [8], which further complicates the analysis. In order to find agreement with all observations, a realistic multi-orbital model including spin-orbit coupling was considered in Ref. [9], based on a spin-fluctuation mechanism giving rise to the interaction. An accidental degeneracy between two superconducting states was proposed, in accordance with the evidence for time-reversal symmetry breaking and singlet pairing in Sr_2RuO_4 . Nevertheless, the results could only be obtained close to the critical temperature. Therefore, a new theoretical formulation is needed in order to investigate the superconducting state at lower temperatures, which could allow for new studies of the coexistence of different symmetries, as well as study the phase transitions observed through the calculation of the specific heat.

In this thesis, we aim to develop a theoretical model and a proper numerical approach capable of determining the leading superconducting state at all temperatures. With this purpose, the first part is devoted to derive a multi-orbital model adequate for describing superconductivity in Sr_2RuO_4 , based on a numerical self-consistent solution of the problem. In this phenomenological model, superconductivity is assumed to originate from an on-site attraction. On the contrary, in the second part, we introduce a more realistic model, considering that superconductivity is arising from a spin-fluctuation mechanism. Thus, we derive a new proposal based on the addition of the interactions with the closest 28 neighbors. Furthermore, in order to establish the most favorable superconducting state, we perform a classification based on group theory, using the particular point group symmetry of Sr_2RuO_4 . The model considered, which successfully allows us to solve for the superconducting state below the transition temperature, could finally reveal if this interaction mechanism can explain all experimental observations until now.

The thesis is structured as follows: in Chapter 2, an introduction to the main characteristics of Sr_2RuO_4 is presented, including its superconducting properties. Moreover, we include a brief outline of the main experimental results for this material. In Chapter 3, we detail the model considered and the motivation supporting it. In Chapter 4, the self-consistent calculations are derived from a general multi-orbital interacting Hamiltonian. After deriving the equations, in Chapters 5 and 6 we consider examples of systems with different orbitals and include on-site attractive interactions and interactions with nearest neighbors, respectively. In order to obtain a more realistic model, in Chapter 7 a new pairing mechanism based on spin-fluctuations is included focusing on the three-orbital case, and the equations for the addition of up to 28 neighbors are derived. In Chapter 8, we present the obtained numerical results with the inclusion of the previous interactions. Finally, in Chapter 9, we summarize our main results and conclusions.

Chapter 2

Introduction to Sr_2RuO_4

After more than two decades of research, understanding superconductivity in Sr_2RuO_4 is still an open problem in condensed matter physics. The main challenge in recent studies has been to propose a consistent explanation in agreement with all experimental observations. In this section, a brief overview of the most important features for Sr_2RuO_4 relevant for the present thesis will be discussed. In particular, special emphasis is made in the electronic structure and the superconducting state. In order to understand the present situation, it is also very important to introduce the main experimental results, which constrain the theoretical models.

The discussions regarding the superconducting state arose since the discovery of Sr_2RuO_4 . Initially, it was thought that superconductivity in this material would be similar to the copper based superconductors, due to an almost identical crystal structure to that of La_2CuO_4 , as seen in Figure 2.1. In contrast to the cuprate superconductors, in the case of strontium ruthenate a remarkably low transition temperature to the superconducting state was observed around 1.5 K [1]. Furthermore, it was soon reported as a type II superconductor, since the upper critical field was measured [10]. More importantly, Sr_2RuO_4 allows for the growth of extremely high-quality single crystals, which implies that disorder is not an experimental complication factor as it is in other materials [11]. In fact, one of the main reasons why the superconducting state is believed to be unconventional is due to the sensitivity to impurities [12].

After some years and the appearance of new experimental evidence, it was commonly accepted that its superconductivity was more similar to the unique case of superfluid helium-3 (^3He). Nevertheless, recent experiments and theoretical studies have contradicted the previous result, suggesting that superconductivity in this material could be much more complicated than previously thought. Moreover, as we will see in more detail in this Chapter, the multi-orbital nature of the electronic states [7] and the presence of a sizable spin-orbit coupling further complicate the analysis. The situation is even more intriguing since earlier studies reported that, in contrast to the complex superconducting state, in the normal state it behaves as a well-known Fermi liquid, confirmed by the observation of the T^2 dependence of the resistivity [13, 14].

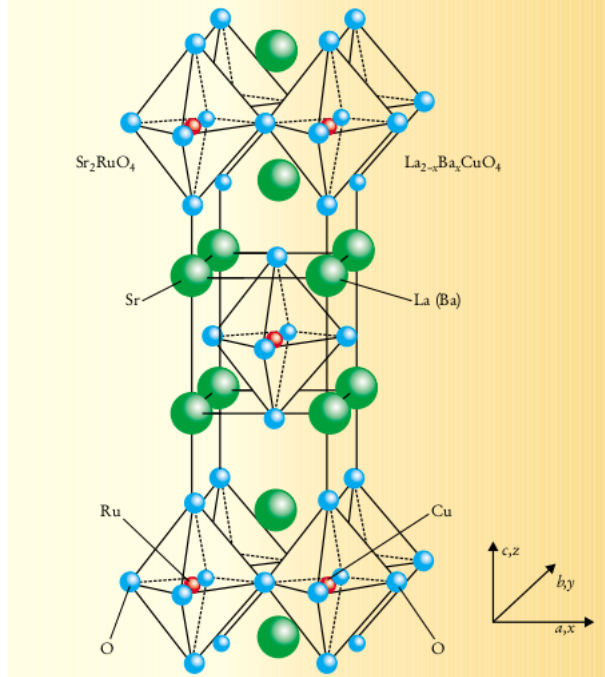


Figure 2.1: Schematic crystal structure of the superconductors Sr_2RuO_4 and $\text{La}_{2-x}\text{Ba}_x\text{CuO}_4$. The RuO_2 layers are separated by Sr layers, and the Ru ions are located at the center of an octahedron of O ions. Image taken from [15].

2.1 Electronic structure and multi-orbital physics

First of all, to address the electronic structure, it is important to remember the effect of the crystal field, which is an electric field derived from neighboring atoms in the crystal, and plays a major role in the energy levels of an atom. Moreover, to understand the model considered, it must be recalled that the valence of the ruthenium ion is Ru^{4+} and, therefore, four electrons remain in the $4d$ shell. As seen from Figure 2.1, the crystal's RuO_4 layers are separated by Sr layers, and each Ru ion is located at the center of an octahedron of O ions. Consequently, the negative charge of the O^{2-} ions located at the vertices of an octahedron splits the five $4d$ states into two groups, the threefold referred as t_{2g} orbitals and a twofold designated as e_g orbitals, and their energies depend on the orientation of the orbitals.

To further understand this, it is necessary to recall the shapes of the atomic orbitals, shown in Figure 2.2 for the t_{2g} orbitals. Since the orbitals d_{z^2} and $d_{x^2-y^2}$ point directly towards the negative charges, an electron in these two orbitals will have a higher energy. By contrast, the lobes of the orbitals d_{xz} , d_{yz} , d_{xy} are oriented between the negative charges and, as a consequence, they will have a lower energy. Therefore, in a low-energy model, the electrons in these three orbitals are the ones forming the Fermi surface, which has been experimentally determined with

high accuracy [16–18], as shown in Figure 2.3. Importantly, it separates into three bands, one of xy character (γ band) and two of xz and yz mixed characters (α and β bands, respectively), all contributing to the superconducting state. In addition, only the mixing of xz and yz orbitals is considered, known as the hybridization. The mixing between the xy and the xz/yz orbitals is prevented due to the difference under parity transformation $z \rightarrow -z$ around the center of a RuO_2 plane.

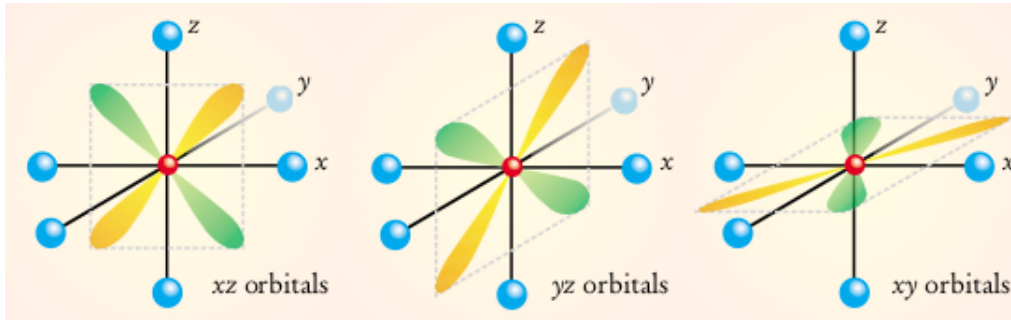


Figure 2.2: $4d t_{2g}$ orbitals responsible for superconductivity in Sr_2RuO_4 . Image taken from [15].

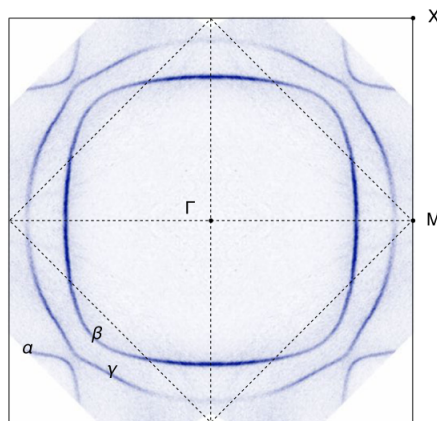


Figure 2.3: Fermi surface of Sr_2RuO_4 . The data was acquired at 5 K on a CO passivated surface with a photon energy of 11 eV and p polarization for measurements along the ΓX symmetry line. The Brillouin zone of the reconstructed surface layer is indicated by diagonal dashed lines. Image taken from [18].

2.2 Superconductivity in Sr_2RuO_4

We will begin this section by reviewing the basic concepts of the Bardeen-Cooper-Schrieffer (BCS) theory, and then we will focus on the superconducting state of strontium ruthenate. The BCS microscopic theory of superconductivity was developed in 1957 [19], based on the observations of the instability of the electron gas, which showed that below a critical temperature T_c a new ground state is formed by electron pairs bound in time-reversed states, known as the Cooper pairs. These quasiparticles are formed near the Fermi level and are the origin of the superconducting state.

It is well-known that the BCS theory describes accurately enough the behavior of conventional superconductors, usually characterized by Cooper pairs bound with a zero orbital angular momentum, considering that close to the Fermi surface the exchange of phonons induces an attraction capable of overcoming the electron's Coulomb repulsion. The order parameter of superconductivity is generally represented by the gap function $\Delta(\mathbf{k})$, which is a complex function with both an amplitude and a phase that describes the macroscopic quantum states of the Cooper pairs. The gap function in a simple one-orbital model can be parametrized by a 2×2 matrix. For a spin singlet, only a scalar function $\psi(\mathbf{k})$ is needed, which satisfies $\psi(\mathbf{k}) = \psi(-\mathbf{k})$. For the spin triplet case, three components are needed, introduced as the vector function $\mathbf{d}(\mathbf{k})$, fulfilling $\mathbf{d}(\mathbf{k}) = -\mathbf{d}(-\mathbf{k})$.

To understand the symmetry of the order parameter, we must remember that a fermion pair requires an antisymmetric wave function under the exchange of two electrons. Since the pair wave function $\Psi_{\sigma\sigma'}(\mathbf{k}) = f(\mathbf{k})\chi_{\sigma\sigma'}$ has a spatial part ($f(\mathbf{k})$) and a spin part ($\chi_{\sigma\sigma'}$), orbital wave functions with even values of the orbital angular momentum ($l = 0, 2, 4, \dots$) must correspond to a spin singlet ($S = 0$). On the contrary, orbital wave functions with odd values of the angular momentum ($l = 1, 3, 5, \dots$) correspond to spin triplets ($S = 1$) [20]. In analogy with the notation for the atomic states, the singlet superconductor with an even function of the momentum \mathbf{k} is denoted as s -wave for $l = 0$, d -wave for $l = 2$, etc. In the same way, a triplet superconductor with an odd function of the momentum \mathbf{k} is called p -wave for $l = 1$, f -wave for $l = 3$, etc. We can distinguish between the different possibilities depending on how the order parameter transforms under the different operations of the tetragonal group. In addition, within a certain state we can have a gap structure, determined by the \mathbf{k} -dependence of the order parameter.

Experimental observations showed that unconventional superconductivity became the most feasible answer to explain the behavior of Sr_2RuO_4 [12]. Therefore, a lot of questions arose to be answered, such as the spin character, the angular momentum of the Cooper pairs or the mechanism capable of inducing superconductivity. In addition, a natural question that appears is in what cases more complicated superconducting states would be favorable. To understand this intuitively, we need to consider the existence of a strong on-site Coulomb repulsion, as occurs in the case of Sr_2RuO_4 . To reduce the repulsion energy, the formation of a Cooper pair with a large amplitude of the wave function is favored, which can be achieved when the electrons in

the condensate have a finite relative orbital angular momentum [21]. Regarding the mechanism inducing superconductivity, different speculations were made. After reporting the presence of spin-fluctuations [22], a reasonable suggestion was that it could give rise to the interaction.

As previously mentioned, due to the similarities in the superconducting state of strontium ruthenate with ^3He , initially a p -wave state was proposed, hence corresponding to a spin-triplet pairing [2, 3]. In particular, in agreement with the evidence of time-reversal symmetry (TRS) breaking [5], they considered a state of the form $p_x + ip_y$, known as chiral, remembering that TRS implies a complex conjugation of the state. Nevertheless, as will be detailed in the following sections, later experiments no longer supported the existence of a superconducting state using only spin-triplet superconductivity. Moreover, the chiral p -wave state is supposed to spontaneously generate supercurrents at sample edges and domain boundaries, which would produce measurable edge magnetic fields. However, the observation of such currents has been elusive until now [23–25].

2.2.1 The role of spin-orbit coupling

The importance of spin-orbit coupling was later stressed [8, 26–28], which has profound implications in the characterization of the shape and the orbital character of the Fermi surface sheets. In this way, it is crucial to add this effect in the calculations, although its influence will depend on the pairing mechanism and the band structure considered.

Due to the presence of spin-orbit coupling, spin is no longer a good quantum number. As a result, the distinction between spin-triplet and spin-singlet to describe the superconducting state becomes misleading, and it appears the possibility of a state where the two spins characters are strongly mixed. Thus, a more appropriate description for the symmetry of the superconducting state corresponds to odd or even parity, characterizing both the spatial and the spin and orbital spaces. The important role of spin-orbit coupling called for a review of the previous accepted theories, based only on triplet p -wave superconductivity in Sr_2RuO_4 . Consequently, other order parameter symmetries that included the effect of spin-orbit coupling were proposed theoretically [29–31], and models based on a realistic Fermi surface parametrization have found that many different even and odd parity order parameters are close to being degenerate [32, 33].

2.3 Experiments

The current challenge in strontium ruthenate is to identify the superconducting state compatible with all the experimental observations. Since the discovery of superconductivity in Sr_2RuO_4 , different experiments have provided valuable information regarding the symmetries of the superconducting phase. Nevertheless, important discrepancies have arisen in the recent years, see Ref. [32] for a review in the topic. In this section, we aim to briefly introduce the most important measurements performed, which contributed to the present understanding of this material.

2.3.1 Knight shift

The Knight shift experiments measure the change in the frequency in nuclear magnetic resonance (NMR) owing to the spin polarization of the electrons under an applied magnetic field. In the case of a Cooper pair formed by spin singlets, the electrons would not be polarized at all with the small fields applied in NMR experiments. Thus, the Knight shift should vanish at zero temperature. On the contrary, for a triplet superconductor, when a magnetic field is applied the number of pairs with spin parallel and antiparallel would change, and therefore the Knight shift should not vanish. Hence, one of the predictions for an even parity superconductor is a strong drop in the spin susceptibility below the transition temperature. However, the inclusion of a large spin-orbit coupling complicates this analysis.

At an earlier stage, Knight shift measurements identified spin-triplet superconductivity in Sr_2RuO_4 [4], and all experiments reported at that time seemed to be consistent, since no drop of the spin susceptibility was reported [34, 35]. Nevertheless, very recent Knight shift experiments have contradicted previous NMR work, finding a drop below the critical temperature [6, 36], as seen in Figure 2.4. Consequently, previous results were associated with a heating effect of the sample due to the application of high amplitude radio frequency pulses when measuring the Knight shift. After the new revealing measurements, the previous agreement on a chiral spin-triplet p -wave superconductor was questioned.

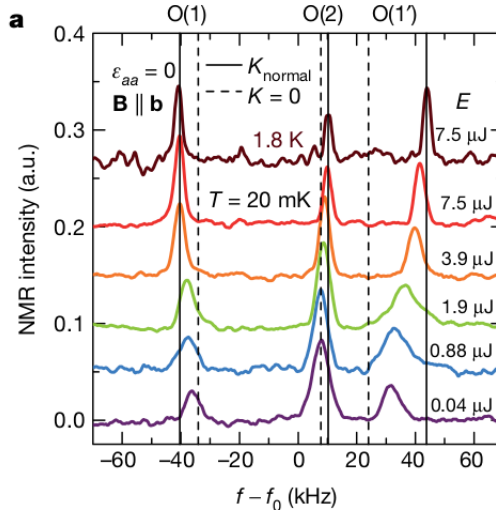


Figure 2.4: NMR spectra for varying pulse energy at the base temperature $T = 20$ mK. The O(1) and O(1') peak shifts indicate smaller intensity for a smaller pulse energy (E). For each site, the normal-state position is marked by the solid vertical line and the estimated zero Knight shift ($K=0$) position by the dashed line. Image taken from [6].

2.3.2 Muon spin relaxation and polar Kerr effect

In muon spin relaxation (μ SR) experiments, spin-polarized positive muons are injected into the sample. After quickly coming to rest, their spins evolve in the local magnetic environment, and then they decay emitting a positron. The muon polarization as a function of time can be obtained from time histograms of these positrons. Thus, when there is a magnetically ordered state, an increase in the relaxation rate will be observed. In the case of Sr_2RuO_4 , muon spin rotation indicated the development of spontaneous magnetism near the muon implantation sites, even when the samples were cooled at zero external field [5], implying that time-reversal symmetry (TRS) is broken. In Figure 2.5 the observed increase in the measured relaxation rate is shown.

The previous results were confirmed later on by measurements of magneto-optic polar Kerr rotation [37]. Polar Kerr effect experiments measure the rotation of the direction of the reflected linearly polarized light normally incident to the superconducting planes. Since this type of experiment allows to measure the existence of an antisymmetric contribution to the real and imaginary parts of the frequency-dependent dielectric tensor, it is consequently sensitive to time-reversal symmetry breaking.

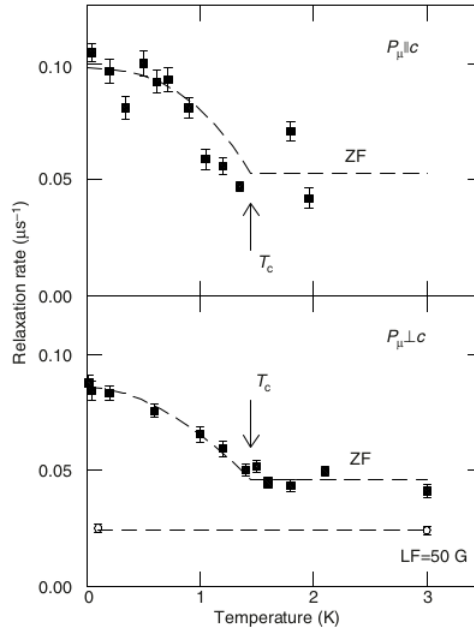


Figure 2.5: Zero field (ZF) relaxation rate for the initial muon spin polarization parallel (top) and perpendicular (bottom) to the c axis, where T_c is indicated by arrows. Circles in bottom figure give relaxation rate in a weak applied longitudinal field, discarding the possibility of fluctuating magnetic fields. Image taken from [5].

When time-reversal symmetry breaking was reported, it was considered a further proof of the chiral $p_x + ip_y$ state. However, in view of the recent NMR experiments, new complex proposals have to be made considering a degeneracy between two order parameters, such as $s + id$, which also corresponds to a state breaking TRS.

2.3.3 Specific heat

The first measurements of the specific heat for Sr_2RuO_4 were done by Nishizaki *et al.* [38], which can be seen in Figure 2.6a. Since the temperature dependence of the electronic specific heat divided by temperature was linear, and not exponential as expected from previous proposals, their results seemed inconsistent with the chiral superconductivity considered until then.

In addition, as shown in Figure 2.6b, it has recently been measured that under uniaxial applied strain no second transition is observed, as would be expected for a two-component order parameter of the form $p_x + ip_y$ [39].

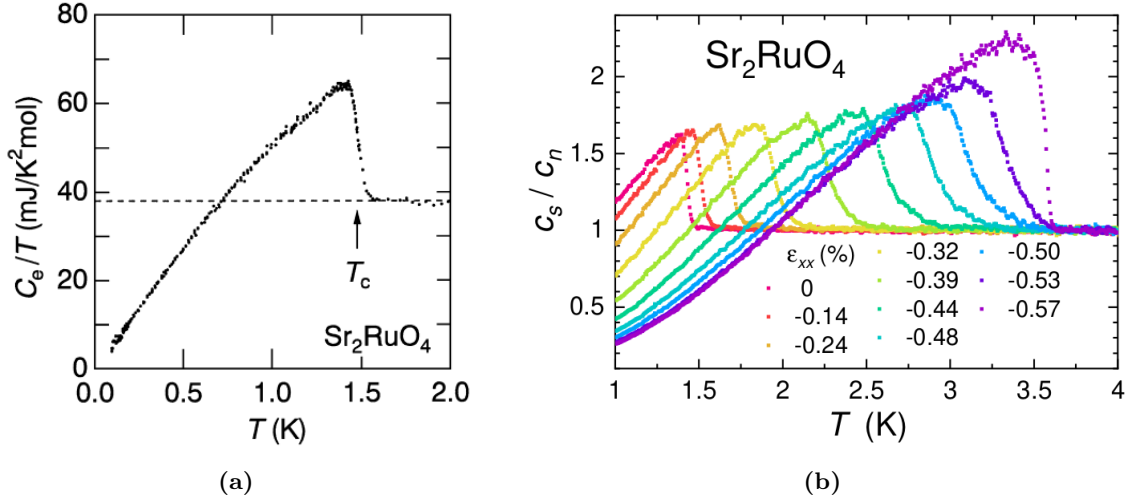


Figure 2.6: a) Electronic specific heat divided by temperature, C_e/T , plotted against temperature of Sr_2RuO_4 under zero applied field. Image taken from [38]. b) Superconducting state heat capacity normalized to the normal-state value, showing the evolution of the anomaly height c_s/c_n with T_c under applied strain. Image taken from [39].

2.3.4 Scanning tunneling microscopy

A scanning tunneling microscope (STM) uses an extremely sharp metallic tip located a few Å above an electrically conducting sample to image the surface. Then, a bias voltage V applied between the tip and the sample results in a current, which can be measured as a function of the location and the applied voltage. By changing the bias voltage and measuring the tunneling current I , keeping fixed the distance between the tip and the sample, the density of states can be obtained, which is proportional to the conductance dI/dV . Thus, STM directly provides information of the superconducting gap.

As seen in Figure 2.7, STM experiments have been able to resolve the small gap of Sr_2RuO_4 [40, 41]. Moreover, a linear decrease is observed for the conductance as a function of the energy, until reaching a minimum at zero energy. These results confirm that the superconducting state is not a simple s-wave, since in this case we would observe a sharp decrease of the conductance. Therefore, the shape of the spectrum is consistent with a nodal gap structure, which implies that the order parameter should present some zero values at the Fermi surface.

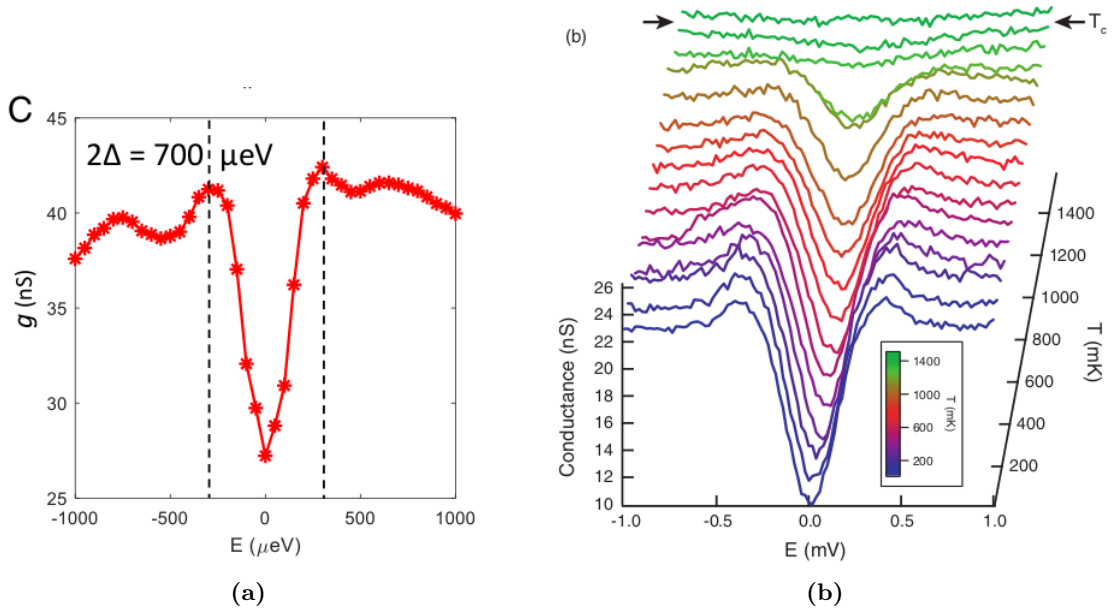


Figure 2.7: a) Spatially averaged superconducting tunneling spectrum showing the full energy gap $\Delta \approx 350 \mu\text{eV}$ measured at $T = 90 \text{ mK}$. Image taken from [41]. b) Differential conductance spectra for a sample temperature range between 20 mK and 1.5 K. The observed gap becomes zero above the superconducting critical temperature $T_c = 1.45 \text{ K}$, indicated by arrows, as one would expect for the superconducting gap $\Delta(T)$. The shape of this spectrum is very consistent with a nodal gap structure. The gap magnitude is of $\sim 350 \mu\text{eV}$. Image taken from [40].

2.3.5 Summary of the experimental constrains

Since in this thesis we aim to find agreement with all experimental observations, we summarize here the requirements for the gap presented in the previous sections:

1. The superconducting state has to be compatible with a Knight shift reduction, and therefore it should have a leading spin-singlet component;
2. Muon spin relaxation and polar Kerr effect measurements reveal that the superconducting state has to break time-reversal symmetry;
3. The evidence for time-reversal symmetry breaking implies the existence of complex combinations of several order parameters (examples include $p_x + ip_y$, $s + id$, etc), and therefore the superconducting condensate must be comprised of two components;
4. The structure of the gap must present nodes, in agreement with STM experiments.

Chapter 3

Model and motivation

Once the main characteristics of Sr_2RuO_4 have been presented, in this Chapter we proceed to describe the model that we will use in this thesis. Moreover, we will emphasize the motivation behind it and explain why it could reveal new information on the superconducting state, always remembering that we are seeking agreement with all experimental observations.

Since the layered structure of Sr_2RuO_4 prevents a strong overlap of the orbitals along the c -axis (see Figure 2.1), to a first approximation the electronic structure can be considered two-dimensional [42]. Therefore, we can consider a two-dimensional lattice mode, where each site corresponds to a ruthenium atom and includes the interactions with the neighboring oxygen atoms in the octahedral environment.

The aim of this project is to construct a three-orbital model adequate for Sr_2RuO_4 and to solve for the superconducting order parameter at all temperatures, implementing realistic interactions based on a spin-fluctuation mechanism. To achieve this purpose, we need to consider a Hamiltonian for a multi-orbital system and perform a mean-field decoupling in the Cooper channel. Thus, this allows us to construct the Bogoliubov-de Gennes Hamiltonian (BdG) and solve self-consistently for the superconducting gap by introducing the Bogoliubov transformations. Nonetheless, it is important to remember that in this material the spin-orbit coupling has a very important effect. As a consequence, we will need to solve the full BdG Hamiltonian, including three orbitals and the spin configurations. In our approach of the problem, we are interested in solving for the order parameter in both momentum and real space. The former one allows us to study the homogeneous case, whereas the latter is needed to study how impurities affect the system.

In the first part of the thesis, a phenomenological study of superconductivity is done for Sr_2RuO_4 , considering that it is originated from an on-site attraction. In this case, both solutions in momentum and real space are presented for an effective three-band model. In the second part, superconductivity is considered as spin-fluctuation driven, and a thorough study is performed in momentum space, aiming to classify the symmetry of the superconducting order parameter

and study important physical quantities such as the specific heat.

The motivation behind this research is based on the previous works in Refs. [9, 43]. In these studies, a realistic model for Sr_2RuO_4 is considered in order to solve the linearized gap equation at the transition temperature and determine the leading symmetry for the order parameter. Nevertheless, the main drawback is that no information can be provided below the critical temperature. Consequently, the self-consistent formulation becomes essential to investigate what occurs at a lower temperature, being able to reveal if there is a coexistence of different superconducting phases and to study the possibility of different phase transitions by calculating the specific heat.

Therefore, we will consider the same model as in Ref. [9], where Sr_2RuO_4 has been studied by taking the Hamiltonian

$$H = H_0 + H_{\text{SOC}} + H_{\text{int}}. \quad (3.1)$$

In the equation above, the first term corresponds to the bare Hamiltonian,

$$H_0 = \begin{pmatrix} \xi^{xz}(\mathbf{k}) & g(\mathbf{k}) & 0 \\ g(\mathbf{k}) & \xi^{yz}(\mathbf{k}) & 0 \\ 0 & 0 & \xi^{xy}(\mathbf{k}) \end{pmatrix} \otimes \mathbf{1}_\sigma, \quad (3.2)$$

considering the basis $\{xz \uparrow, xz \downarrow, yz \uparrow, yz \downarrow, xy \uparrow, xy \downarrow\}$. The dispersions for the three orbitals are given by $\xi^{xz}(\mathbf{k}) = -2t_1 \cos k_x - 2t_2 \cos k_y - \mu$, $\xi^{yz}(\mathbf{k}) = -2t_2 \cos k_x - 2t_1 \cos k_y - \mu$ and $\xi^{xy}(\mathbf{k}) = -2t_3(\cos k_x + \cos k_y) - 4t_4 \cos k_x \cos k_y - 2t_5(\cos 2k_x + \cos 2k_y) - \mu$. As in Ref. [44], we parametrize the band by $\{t_1, t_2, t_3, t_4, t_5\} = \{88, 9, 80, 40, 5\}$ meV, and the chemical potential is given by $\mu = 109$ meV. The hybridization between xz and yz orbitals is taken as $g(\mathbf{k}) = -4t' \sin k_x \sin k_y$, parametrized by $t' = 4.4$ meV [45].

The second term in equation (3.1) includes the effect of spin-orbit coupling, and is given by

$$H_{\text{SOC}} = \lambda_{\text{SOC}} \mathbf{L} \cdot \mathbf{S}, \quad (3.3)$$

considering $\lambda_{\text{SOC}} = 35$ meV [46]. In the previous basis it can be written as

$$H_{\text{SOC}} = \frac{\lambda_{\text{SOC}}}{2} \begin{pmatrix} 0 & 0 & -i & 0 & 0 & i \\ 0 & 0 & 0 & i & i & 0 \\ i & 0 & 0 & 0 & 0 & -1 \\ 0 & -i & 0 & 0 & 1 & 0 \\ 0 & -i & 0 & 1 & 0 & 0 \\ -i & 0 & -1 & 0 & 0 & 0 \end{pmatrix}, \quad (3.4)$$

obtained by rewriting the product $\mathbf{L} \cdot \mathbf{S}$ in terms of the lowering and raising spin operators. In this way, since the three t_{2g} orbitals d_{xz}, d_{yz}, d_{xy} can be expressed in terms of the spherical harmonics, we can calculate how the angular momentum operators act on them. By adding this term to the previous Hamiltonian we obtain the total non-interacting Hamiltonian, $H_{\text{non-int}} = H_0 + H_{\text{SOC}}$.

Finally, the third term in equation (3.1) accounts for the interactions, which are derived from the multi-orbital Hubbard type Hamiltonian

$$\begin{aligned}
H_{\text{int}} = & U \sum_{i,\mu} \hat{n}_{i\mu\uparrow} \hat{n}_{i\mu\downarrow} + U' \sum_{i,\mu<\nu,\sigma} \hat{n}_{i\mu\sigma} \hat{n}_{i\nu\bar{\sigma}} + (U' - J) \sum_{i,\mu<\nu,\sigma} \hat{n}_{i\mu\sigma} \hat{n}_{i\nu\sigma} \\
& + J \sum_{i,\mu<\nu,\sigma} \hat{c}_{i\mu\sigma}^\dagger \hat{c}_{i\nu\bar{\sigma}}^\dagger \hat{c}_{i\mu\bar{\sigma}} \hat{c}_{i\nu\sigma} + J' \sum_{i,\mu<\nu,\sigma} \hat{c}_{i\mu\sigma}^\dagger \hat{c}_{i\mu\bar{\sigma}}^\dagger \hat{c}_{i\nu\bar{\sigma}} \hat{c}_{i\nu\sigma},
\end{aligned} \tag{3.5}$$

where i is the site index, μ, ν are orbital indices, $\sigma = -\bar{\sigma}$ correspond to the electronic spins, and we denote $\hat{n}_{i\mu\sigma} = \hat{c}_{i\mu\sigma}^\dagger \hat{c}_{i\mu\sigma}$. Assuming rotational symmetry, the relations $U' = U - 2J$ and $J = J'$ hold. In the previous Hamiltonian, the first term corresponds to an intraorbital Coulomb interaction between electrons with opposite spin, while the second one corresponds to an interorbital interaction between electrons, also with opposite spin. The third term represents the interorbital interaction of electrons with the same spin. The fourth contribution corresponds to the Hund's coupling interaction, and finally the last part is the pair hopping energy. In the case of Sr_2RuO_4 , the importance of a sizeable Hund's coupling has been estimated to be $J/U \simeq 0.1$ [47].

Considering only the previous bare interactions and restricting to the Cooper channel, the Hamiltonian in momentum space reads

$$H_{\text{int}} = \frac{1}{2} \sum_{\mathbf{k}, \mathbf{k}', \{\tilde{\mu}\}} [U]_{\tilde{\mu}_3, \tilde{\mu}_4}^{\tilde{\mu}_1, \tilde{\mu}_2} c_{\mathbf{k}\tilde{\mu}_1}^\dagger c_{-\mathbf{k}\tilde{\mu}_3}^\dagger c_{-\mathbf{k}'\tilde{\mu}_2} c_{\mathbf{k}'\tilde{\mu}_4}, \tag{3.6}$$

where the notation $\tilde{\mu}_i = \{\mu_i, \sigma_i\}$ denotes both orbital and spin indices, and the electron-electron interactions correspond to

$$\begin{aligned}
[U]_{\mu\bar{\sigma}, \mu\bar{\sigma}}^{\mu\sigma, \mu\sigma} = U, & \quad [U]_{\mu\bar{\sigma}, \mu\bar{\sigma}}^{\nu\sigma, \nu\sigma} = U', & \quad [U]_{\nu\bar{\sigma}, \nu\bar{\sigma}}^{\mu\sigma, \nu\sigma} = J, & \quad [U]_{\mu\bar{\sigma}, \nu\bar{\sigma}}^{\mu\sigma, \nu\sigma} = J', & \quad [U]_{\nu\sigma, \nu\sigma}^{\mu\sigma, \mu\sigma} = U' - J, \\
[U]_{\mu\bar{\sigma}, \mu\bar{\sigma}}^{\mu\sigma, \mu\bar{\sigma}} = -U, & \quad [U]_{\mu\bar{\sigma}, \nu\bar{\sigma}}^{\nu\sigma, \mu\bar{\sigma}} = -U', & \quad [U]_{\nu\bar{\sigma}, \nu\bar{\sigma}}^{\mu\sigma, \mu\bar{\sigma}} = -J, & \quad [U]_{\mu\bar{\sigma}, \nu\bar{\sigma}}^{\mu\sigma, \nu\bar{\sigma}} = -J', & \quad [U]_{\nu\sigma, \mu\sigma}^{\mu\sigma, \nu\sigma} = -(U' - J).
\end{aligned} \tag{3.7}$$

In the first approach to build a three band model for Sr_2RuO_4 , U will be considered attractive, in order to stabilize superconductivity. In the second part, we will account for the effective interactions mediated by spin fluctuations,

$$H_{\text{SC}}^{\text{SF}} = \frac{1}{2} \sum_{\mathbf{k}, \mathbf{k}', \{\tilde{\mu}\}} [V(\mathbf{k}, \mathbf{k}')]_{\tilde{\mu}_3, \tilde{\mu}_4}^{\tilde{\mu}_1, \tilde{\mu}_2} c_{\mathbf{k}\tilde{\mu}_1}^\dagger c_{-\mathbf{k}\tilde{\mu}_3}^\dagger c_{-\mathbf{k}'\tilde{\mu}_2} c_{\mathbf{k}'\tilde{\mu}_4}, \tag{3.8}$$

where the pairing interaction $[V(\mathbf{k}, \mathbf{k}')]_{\tilde{\mu}_3, \tilde{\mu}_4}^{\tilde{\mu}_1, \tilde{\mu}_2}$ includes the contributions from the bare interactions, as well as the sum of higher order diagrams to infinite order, which will be briefly discussed in Chapter 7.

3.1 Fermi surface

Once the relevant model has been presented, it is also instructive to plot the Fermi surface. With this purpose, we need to diagonalize the Hamiltonian and plot the contour where the eigenenergies are zero. In Figure 3.1a, only the Hamiltonian containing the electronic dispersions is studied, whereas in Figure 3.1b the spin-orbit coupling Hamiltonian is also included. In the latter case, we can distinguish three different bands corresponding to the inner β and the outer α pockets and, in between them, the γ band, in agreement with the Fermi surface measurements shown in Figure 2.3.

It is also interesting to calculate the dominant orbital contribution to the three bands at each point of the Fermi surface. With this purpose, it is important to notice that the non-interacting Hamiltonian is originally written in orbital space and, after diagonalization, the energies are given in band space. Therefore, with a change of basis given by the coefficients $u_{n\mu\mathbf{k}}$, we can transform from one space to the other,

$$\hat{c}_{n\mathbf{k}} = \sum_{\mu} u_{n\mu\mathbf{k}} \hat{c}_{\mu\mathbf{k}}, \quad (3.9)$$

where $\hat{c}_{n\mathbf{k}}$ and $\hat{c}_{\mu\mathbf{k}}$ correspond to band and orbital space, respectively. From the expression above, we can see that the leading orbital contributing to a certain band for each \mathbf{k} point is given by the largest weight $|u_{n\mu\mathbf{k}}|^2$. Hence, simply by comparing the coefficients we can obtain the information of the dominant orbital xz, yz or xy . As seen in Figure 3.1, when spin-orbit coupling is included in the model, the dominant orbital contribution is mixed in all bands depending on the value of \mathbf{k} .

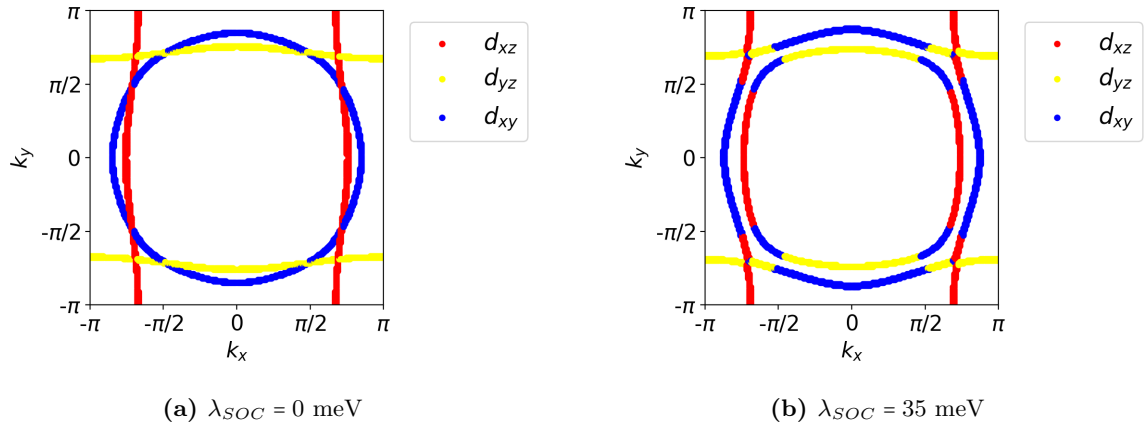


Figure 3.1: Sr_2RuO_4 Fermi surface without and with spin-orbit coupling, with the values given in each caption. In both plots, the dominant orbital contribution is shown, where xy orbital is blue, xz is red, and yz is yellow.

3.2 Linearized gap equation

In this section, we present the results obtained in Ref. [9] using the linearized gap equation. This will become important later, since an agreement with the self-consistent solution should be found at the critical temperature. First of all, we will briefly introduce the linearized gap equation approach to the problem for the case of a one-band model, while the complete derivation can be found in Ref. [48]. The BCS gap equation is given by

$$\Delta_{\mathbf{k}} = \sum_{\mathbf{k}'} V_{\mathbf{k}\mathbf{k}'} \frac{\Delta_{\mathbf{k}'}}{2E_{\mathbf{k}'}} \tanh \frac{E_{\mathbf{k}'}}{2k_B T}, \quad (3.10)$$

as derived in Appendix A for the one-band model. In general, the previous equation must be solved self-consistently, but the idea behind the linearized gap equation is to consider a solution of the gap for a temperature just below the superconducting transition temperature, where the mean field order parameter $\Delta_{\mathbf{k}}$ is expected to be very small. Hence, we can take the approximation

$$E_{\mathbf{k}} = \sqrt{\xi_{\mathbf{k}}^2 + |\Delta_{\mathbf{k}}|^2} \approx |\xi_{\mathbf{k}}|. \quad (3.11)$$

Using this assumption, the BCS gap equation can be written as

$$\Delta_{\mathbf{k}} = \underbrace{\left[-\frac{1}{2(2\pi)^2} \int_{FS} \frac{d\mathbf{k}'}{|v_{\mathbf{k}'}} V_{\mathbf{k}\mathbf{k}'} \Delta_{\mathbf{k}'} \right]}_{\lambda \Delta_{\mathbf{k}}} \int_{-\xi_c}^{\xi_c} d\xi \frac{1}{2|\xi|} \tanh \left(\frac{|\xi|}{2k_B T} \right), \quad (3.12)$$

where the Fermi velocity is given by $v_{\mathbf{k}} = \frac{d\xi_{\mathbf{k}}}{d\mathbf{k}}$, ξ_c corresponds to the energy cutoff, and the first integral is performed over the Fermi surface (FS). The energy integral can be solved approximately in the limit where $\xi_c < k_B T$. The remaining part of the linearized gap equation can be expressed as an eigenvalue problem, denoted by λ , and solved by diagonalizing the matrix dependent on \mathbf{k} and \mathbf{k}' . Therefore, the largest eigenvalue will correspond to the leading superconducting stability, since it gives rise to the largest superconducting transition temperature. The linearized gap equation can be extended to a multi-orbital system, leading to the eigenvalue problem stated in equation (6) if Ref. [9], for the particular case of Sr_2RuO_4 .

In Figure 3.2, the phase diagram found using the linearized gap equation is shown, for the Fermi surface plotted in the inset. Remarkably, there are three leading superconducting instabilities depending on the spin-orbit coupling and the Hund's coupling, corresponding to an s -wave, a d -wave and a helical solution. The first two correspond to even-parity states, whereas the last one is of odd parity. The distinction between the different states is given according to how the order parameter transforms under all operations of the tetragonal point group, as we will see in detail in the next Chapter.

As previously mentioned, this approach only obtains results for the gap close to the critical temperature. Therefore, to overcome this problem we can use the BdG formulation, which will allow us to investigate further under the transition temperature and see which is the most

favourable order parameter symmetry for Sr_2RuO_4 . Nevertheless, to classify the state through the self-consistent formulation we have to use that Sr_2RuO_4 has a tetragonal symmetry, so that a complete group theoretical classification can be done. As a consequence, the main concepts regarding group theory will be introduced in Chapter 5.

To explain the experimental evidence for time-reversal symmetry (TRS) breaking, in Ref. [9] it was proposed that the system is close to a phase boundary, in particular in the accidentally degenerate state $s + id$. With the BdG self-consistent calculation we can verify if this state is an accidental degeneracy and determine if TRS is broken below the transition temperature.

In addition, states of the previous form would involve two phase transitions. First, the system is expected to be in a certain superconducting symmetry and, at a lower temperature, achieve the combination of two phases that breaks TRS. Contrarily, experimentally only one peak has been observed both under no strain [38], as well as under strain [39], as shown in Figure 2.6. By solving the homogeneous system, we can calculate the heat capacity under the critical temperature and observe the phase transitions.

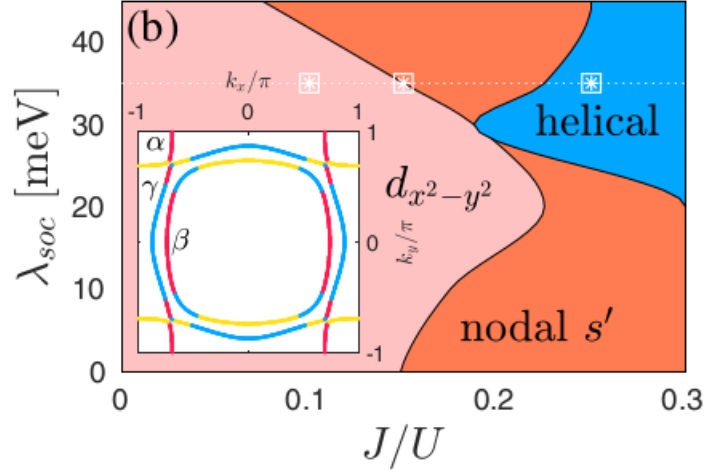


Figure 3.2: Leading superconducting instability as a function of SOC amplitude λ_{SOC} and Hund's coupling J for $\mu = 109$ meV. The Fermi surface with the α , β , and γ bands is shown in the inset, with the dominating orbital content displayed by colors: xy orbital is blue, xz is red, and yz is yellow. Image taken from [9].

Chapter 4

BCS theory for multi-orbital systems

4.1 Hamiltonian and mean-field treatment

In this section, we will introduce the general form of the multi-orbital Hamiltonian and the mean-field approximation used in order to solve for the superconducting order parameter. To begin with, we consider a general Hamiltonian of the form

$$H = H_0 + H_{\text{int}}, \quad (4.1)$$

where H_0 corresponds to the kinetic part and H_{int} to the interacting term, which in our case will give rise to superconductivity.

For the first term, we consider a multi-orbital tight-binding model,

$$H_0 = - \sum_{\mathbf{R}, \mathbf{R}'} \sum_{\mu, \nu} \sum_{\sigma} t_{\mathbf{R}, \mathbf{R}'}^{\mu, \nu} \hat{c}_{\mathbf{R}\mu\sigma}^\dagger \hat{c}_{\mathbf{R}'\nu\sigma} - \mu_0 \sum_{\mathbf{R}} \sum_{\mu} \sum_{\sigma} \hat{c}_{\mathbf{R}\mu\sigma}^\dagger \hat{c}_{\mathbf{R}\mu\sigma}, \quad (4.2)$$

where the operators $\hat{c}_{\mathbf{R}\mu\sigma}^\dagger$ ($\hat{c}_{\mathbf{R}\mu\sigma}$) create (annihilate) an electron at site \mathbf{R} in the orbital μ with spin σ , and μ_0 is the chemical potential. In the particular case of Sr_2RuO_4 , the indices μ and ν will run from 1 to 3 denoting the three orbitals d_{xz} , d_{yz} and d_{xy} , respectively. Therefore, electrons are allowed to jump on the square lattice from the site \mathbf{R}' in orbital ν to the site \mathbf{R} in orbital μ .

The second term in equation (4.1) is given by the general interacting Hamiltonian

$$H_{\text{int}} = \frac{1}{2} \sum_{\mathbf{R}, \mathbf{R}'} \sum_{\substack{\mu_1, \mu_2 \\ \mu_3, \mu_4}} \sum_{\substack{\sigma_1, \sigma_2 \\ \sigma_3, \sigma_4}} [V_{\mathbf{R}, \mathbf{R}'}]_{\mu_4\sigma_4, \mu_3\sigma_3}^{\mu_2\sigma_2, \mu_1\sigma_1} \hat{c}_{\mathbf{R}\mu_2\sigma_2}^\dagger \hat{c}_{\mathbf{R}'\mu_4\sigma_4}^\dagger \hat{c}_{\mathbf{R}'\mu_3\sigma_3} \hat{c}_{\mathbf{R}\mu_1\sigma_1}. \quad (4.3)$$

As previously mentioned, in the first part of the project we will consider that it is described by a BCS term of the form

$$H_{\text{BCS}} = \frac{1}{2} \sum_{\mathbf{R}, \mathbf{R}'} \sum_{\substack{\mu_1, \mu_2 \\ \mu_3, \mu_4}} \sum_{\substack{\sigma_1, \sigma_2 \\ \sigma_3, \sigma_4}} [U]_{\mu_4\sigma_4, \mu_3\sigma_3}^{\mu_2\sigma_2, \mu_1\sigma_1} \hat{c}_{\mathbf{R}\mu_2\sigma_2}^\dagger \hat{c}_{\mathbf{R}'\mu_4\sigma_4}^\dagger \hat{c}_{\mathbf{R}'\mu_3\sigma_3} \hat{c}_{\mathbf{R}\mu_1\sigma_1}, \quad (4.4)$$

where $[U]_{\mu\sigma,\mu\bar{\sigma}}^{\mu\sigma,\mu\bar{\sigma}}$ denotes the strength of an effective attractive on-site interaction. Later on, the driving force for the attraction will be considered to originate through a spin-fluctuation mechanism.

Thus, using the shorthand notation $\tilde{\mu}_i = \{\mu_i, \sigma_i\}$ to include both orbitals and spin, we can rewrite the whole Hamiltonian in equation (4.1) as

$$H = - \sum_{\mathbf{R}, \mathbf{R}'} \sum_{\mu, \nu} \sum_{\sigma} (t_{\mathbf{R}, \mathbf{R}'}^{\mu, \nu} + \mu_0 \delta_{\mathbf{R}, \mathbf{R}'} \delta_{\mu\nu}) \hat{c}_{\mathbf{R}\mu\sigma}^\dagger \hat{c}_{\mathbf{R}'\nu\sigma} + \frac{1}{2} \sum_{\mathbf{R}, \mathbf{R}'} \sum_{\substack{\tilde{\mu}_1, \tilde{\mu}_2 \\ \tilde{\mu}_3, \tilde{\mu}_4}} [V_{\mathbf{R}, \mathbf{R}'}]_{\tilde{\mu}_4, \tilde{\mu}_3}^{\tilde{\mu}_2, \tilde{\mu}_1} \hat{c}_{\mathbf{R}\tilde{\mu}_2}^\dagger \hat{c}_{\mathbf{R}'\tilde{\mu}_4}^\dagger \hat{c}_{\mathbf{R}'\tilde{\mu}_3} \hat{c}_{\mathbf{R}\tilde{\mu}_1}. \quad (4.5)$$

After introducing the microscopic Hamiltonian, we need to impose some approximations in order to study it using numerical methods. With this purpose, we notice that to diagonalize the Hamiltonian it must be quadratic in the electron operators. At this point, it is important to recall mean-field theory, which consists in the decoupling of the four-fermion operators into a sum of all possible bilinear terms in creation and annihilation operators plus constant terms. To do so, it is assumed that the operators deviate slightly from their expectation values,

$$\hat{c}_{\mathbf{R}\tilde{\mu}_2}^\dagger \hat{c}_{\mathbf{R}'\tilde{\mu}_4}^\dagger = \left\langle \hat{c}_{\mathbf{R}\tilde{\mu}_2}^\dagger \hat{c}_{\mathbf{R}'\tilde{\mu}_4}^\dagger \right\rangle + \left\{ \hat{c}_{\mathbf{R}\tilde{\mu}_2}^\dagger \hat{c}_{\mathbf{R}'\tilde{\mu}_4}^\dagger - \left\langle \hat{c}_{\mathbf{R}\tilde{\mu}_2}^\dagger \hat{c}_{\mathbf{R}'\tilde{\mu}_4}^\dagger \right\rangle \right\} \approx \left\langle \hat{c}_{\mathbf{R}\tilde{\mu}_2}^\dagger \hat{c}_{\mathbf{R}'\tilde{\mu}_4}^\dagger \right\rangle - \delta_{cc}, \quad (4.6)$$

where δ_{cc} represents the fluctuations.

Hence, by using the mean-field approximation we can simplify the previous general Hamiltonian. Since we want to study only the superconducting effects, we choose to mean-field decouple the Hamiltonian in the Cooper (particle-particle) channel. Had we wanted to consider the effect of magnetism, we should have also included the decoupling in the particle-hole channel. Therefore, the mean-field interacting Hamiltonian to linear order in the fluctuations is given by

$$H_{\text{int}}^{\text{MF}} = \frac{1}{2} \sum_{\mathbf{R}, \mathbf{R}'} \sum_{\substack{\tilde{\mu}_1, \tilde{\mu}_2 \\ \tilde{\mu}_3, \tilde{\mu}_4}} [V_{\mathbf{R}, \mathbf{R}'}]_{\tilde{\mu}_4, \tilde{\mu}_3}^{\tilde{\mu}_2, \tilde{\mu}_1} \left(\left\langle \hat{c}_{\mathbf{R}\tilde{\mu}_2}^\dagger \hat{c}_{\mathbf{R}'\tilde{\mu}_4}^\dagger \right\rangle \hat{c}_{\mathbf{R}'\tilde{\mu}_3} \hat{c}_{\mathbf{R}\tilde{\mu}_1} + \hat{c}_{\mathbf{R}\tilde{\mu}_2}^\dagger \hat{c}_{\mathbf{R}'\tilde{\mu}_4}^\dagger \left\langle \hat{c}_{\mathbf{R}'\tilde{\mu}_3} \hat{c}_{\mathbf{R}\tilde{\mu}_1} \right\rangle - \text{const.} \right). \quad (4.7)$$

Defining the superconducting order parameter as

$$[\Delta_{\mathbf{R}, \mathbf{R}'}]_{\tilde{\mu}_j}^{\tilde{\mu}_i} = \sum_{\tilde{\mu}_k, \tilde{\mu}_l} [V_{\mathbf{R}, \mathbf{R}'}]_{\tilde{\mu}_j, \tilde{\mu}_l}^{\tilde{\mu}_i, \tilde{\mu}_k} \left\langle \hat{c}_{\mathbf{R}'\tilde{\mu}_l} \hat{c}_{\mathbf{R}\tilde{\mu}_k} \right\rangle, \quad (4.8)$$

and omitting the constant term, we can write the mean-field Hamiltonian so that it is given by

$$H^{\text{MF}} = - \sum_{\mathbf{R}, \mathbf{R}'} \sum_{\mu, \nu} \sum_{\sigma} (t_{\mathbf{R}, \mathbf{R}'}^{\mu, \nu} + \mu_0 \delta_{\mathbf{R}, \mathbf{R}'} \delta_{\mu\nu}) \hat{c}_{\mathbf{R}\mu\sigma}^\dagger \hat{c}_{\mathbf{R}'\nu\sigma} + \frac{1}{2} \sum_{\mathbf{R}, \mathbf{R}'} \sum_{\tilde{\mu}_2, \tilde{\mu}_4} ([\Delta_{\mathbf{R}, \mathbf{R}'}]_{\tilde{\mu}_4}^{\tilde{\mu}_2} \hat{c}_{\mathbf{R}\tilde{\mu}_2}^\dagger \hat{c}_{\mathbf{R}'\tilde{\mu}_4}^\dagger + \text{h.c.}), \quad (4.9)$$

where h.c. denotes the hermitian conjugate.

In addition, we can also write the general Hamiltonian of equation (4.1) in momentum space,

$$H = \sum_{\substack{\mathbf{k}, \sigma \\ \mu, \nu}} \xi_{\mathbf{k}}^{\mu\nu} \hat{c}_{\mathbf{k}\mu\sigma}^\dagger \hat{c}_{\mathbf{k}\nu\sigma} + \frac{1}{2} \sum_{\mathbf{k}, \mathbf{k}', \{\tilde{\mu}\}} [V_{\mathbf{k}, \mathbf{k}'}]_{\tilde{\mu}_4, \tilde{\mu}_3}^{\tilde{\mu}_2, \tilde{\mu}_1} \hat{c}_{\mathbf{k}\tilde{\mu}_2}^\dagger \hat{c}_{-\mathbf{k}\tilde{\mu}_4}^\dagger \hat{c}_{-\mathbf{k}'\tilde{\mu}_3} \hat{c}_{\mathbf{k}'\tilde{\mu}_1}, \quad (4.10)$$

where the first term corresponds to the Fourier transform ($\hat{c}_{\mathbf{R}\tilde{\mu}_i} = \frac{1}{\sqrt{\mathcal{N}}} \sum_{\mathbf{k}} e^{i\mathbf{k}\cdot\mathbf{R}} \hat{c}_{\mathbf{k}\tilde{\mu}_i}$) of the kinetic part, and the second term is the transformation of the interaction. In the Fourier transform, \mathcal{N} corresponds to the normalization factor, and in a numerical approach is given by $\mathcal{N} = N_x \times N_y$, where N_x and N_y represent the lattice size in the x and y directions, respectively.

Similar to the real space case, the mean-field decoupling for the interaction term in equation (4.10) can be written as

$$H_{\text{int}}^{\text{MF}} = \sum_{\mathbf{R}, \mathbf{R}'} \sum_{\tilde{\mu}_2, \tilde{\mu}_4} \frac{1}{\mathcal{N}} [\Delta_{\mathbf{R}, \mathbf{R}'}]_{\tilde{\mu}_4}^{\tilde{\mu}_2} \sum_{\mathbf{k}', \mathbf{k}''} e^{-i(\mathbf{k}'\cdot\mathbf{R} + \mathbf{k}''\cdot\mathbf{R}')} \hat{c}_{\mathbf{k}'\tilde{\mu}_2}^\dagger \hat{c}_{\mathbf{k}''\tilde{\mu}_4}^\dagger. \quad (4.11)$$

Replacing $\mathbf{k}' \rightarrow \mathbf{k} + \frac{\mathbf{q}}{2}$, $\mathbf{k}'' \rightarrow -\mathbf{k} + \frac{\mathbf{q}}{2}$ in the expression above, the total mean-field decoupled Hamiltonian in momentum space given in equation (4.10) reads

$$H^{\text{MF}} = \sum_{\substack{\mathbf{k}, \sigma \\ \mu, \nu}} \xi_{\mathbf{k}}^{\mu\nu} \hat{c}_{\mathbf{k}\mu\sigma}^\dagger \hat{c}_{\mathbf{k}\nu\sigma} + \frac{1}{2} \sum_{\mathbf{k}, \mathbf{q}} \sum_{\tilde{\mu}_2, \tilde{\mu}_4} \left([\Delta_{\mathbf{k}, \mathbf{q}}]_{\tilde{\mu}_4}^{\tilde{\mu}_2} \hat{c}_{\mathbf{k} + \frac{\mathbf{q}}{2}\tilde{\mu}_2}^\dagger \hat{c}_{-\mathbf{k} + \frac{\mathbf{q}}{2}\tilde{\mu}_4}^\dagger + \text{h.c.} \right), \quad (4.12)$$

with the order parameter given by

$$[\Delta_{\mathbf{k}, \mathbf{q}}]_{\tilde{\mu}_j}^{\tilde{\mu}_i} = \frac{1}{\mathcal{N}} \sum_{\mathbf{R}, \mathbf{R}'} [\Delta_{\mathbf{R}, \mathbf{R}'}]_{\tilde{\mu}_j}^{\tilde{\mu}_i} e^{-i(\mathbf{R} - \mathbf{R}')\cdot\mathbf{k}} e^{-i\left(\frac{\mathbf{R} + \mathbf{R}'}{2}\right)\cdot\mathbf{q}}. \quad (4.13)$$

This expression for the order parameter is convenient since we can see that \mathbf{q} corresponds to the center of mass momenta of the Cooper pairs.

Considering equation (4.8), we can transform the operators to momentum space, so that we obtain

$$[\Delta_{\mathbf{R}, \mathbf{R}'}]_{\tilde{\mu}_j}^{\tilde{\mu}_i} = \sum_{\tilde{\mu}_k, \tilde{\mu}_l} [V_{\mathbf{R}, \mathbf{R}'}]_{\tilde{\mu}_j, \tilde{\mu}_l}^{\tilde{\mu}_i, \tilde{\mu}_k} \sum_{\mathbf{k}', \mathbf{q}'} e^{i(\mathbf{R} - \mathbf{R}')\cdot\mathbf{k}'} e^{i\left(\frac{\mathbf{R} + \mathbf{R}'}{2}\right)\cdot\mathbf{q}'} \left\langle \hat{c}_{-\mathbf{k}' + \frac{\mathbf{q}'}{2}\tilde{\mu}_l} \hat{c}_{\mathbf{k}' + \frac{\mathbf{q}'}{2}\tilde{\mu}_k} \right\rangle. \quad (4.14)$$

Thus, replacing this expression in equation (4.13), the superconducting order parameter is given by

$$[\Delta_{\mathbf{k}, \mathbf{q}}]_{\tilde{\mu}_j}^{\tilde{\mu}_i} = \frac{1}{\mathcal{N}} \sum_{\mathbf{k}', \mathbf{q}'} \sum_{\tilde{\mu}_k, \tilde{\mu}_l} [V_{\mathbf{k} - \mathbf{k}', \mathbf{q} - \mathbf{q}'}]_{\tilde{\mu}_j, \tilde{\mu}_l}^{\tilde{\mu}_i, \tilde{\mu}_k} \left\langle \hat{c}_{-\mathbf{k}' + \frac{\mathbf{q}'}{2}\tilde{\mu}_l} \hat{c}_{\mathbf{k}' + \frac{\mathbf{q}'}{2}\tilde{\mu}_k} \right\rangle, \quad (4.15)$$

where we have taken the interaction potential in the wave-vector basis as

$$[V_{\mathbf{k} - \mathbf{k}', \mathbf{q} - \mathbf{q}'}]_{\tilde{\mu}_j, \tilde{\mu}_l}^{\tilde{\mu}_i, \tilde{\mu}_k} = \sum_{\mathbf{R}, \mathbf{R}'} [V_{\mathbf{R}, \mathbf{R}'}]_{\tilde{\mu}_j, \tilde{\mu}_l}^{\tilde{\mu}_i, \tilde{\mu}_k} e^{-i(\mathbf{R} - \mathbf{R}')\cdot(\mathbf{k} - \mathbf{k}')} e^{-i\left(\frac{\mathbf{R} + \mathbf{R}'}{2}\right)\cdot(\mathbf{q} - \mathbf{q}')}. \quad (4.16)$$

To simplify the expression for the interaction potential we can assume it to be translational invariant, so that it fulfills $[V_{\mathbf{R}, \mathbf{R}'}]_{\tilde{\mu}_j, \tilde{\mu}_l}^{\tilde{\mu}_i, \tilde{\mu}_k} \equiv [V_{\mathbf{R} - \mathbf{R}'}]_{\tilde{\mu}_j, \tilde{\mu}_l}^{\tilde{\mu}_i, \tilde{\mu}_k}$. We will consider this assumption to hold even in the presence of impurities, where we have a disordered system. In this case, replacing in equation (4.16) the Fourier transformation of the translational invariant interaction potential

$$[V_{\mathbf{R} - \mathbf{R}'}]_{\tilde{\mu}_j, \tilde{\mu}_l}^{\tilde{\mu}_i, \tilde{\mu}_k} = \frac{1}{\mathcal{N}} \sum_{\mathbf{p}} [V_{\mathbf{p}}]_{\tilde{\mu}_j, \tilde{\mu}_l}^{\tilde{\mu}_i, \tilde{\mu}_k} e^{i\mathbf{p}\cdot(\mathbf{R} - \mathbf{R}')}, \quad (4.17)$$

and performing the sums over \mathbf{R} and \mathbf{R}' , we obtain

$$[V_{\mathbf{k}-\mathbf{k}', \mathbf{q}-\mathbf{q}'}]_{\tilde{\mu}_j, \tilde{\mu}_l}^{\tilde{\mu}_i, \tilde{\mu}_k} = \mathcal{N}[V_{\mathbf{k}-\mathbf{k}'}]_{\tilde{\mu}_j, \tilde{\mu}_l}^{\tilde{\mu}_i, \tilde{\mu}_k} \delta_{\mathbf{q}, \mathbf{q}'}. \quad (4.18)$$

Hence, the expression for the order parameter in equation (4.15) becomes

$$[\Delta_{\mathbf{k}, \mathbf{q}}]_{\tilde{\mu}_j}^{\tilde{\mu}_i} = \frac{1}{\mathcal{N}} \sum_{\mathbf{k}'} \sum_{\tilde{\mu}_k, \tilde{\mu}_l} [V_{\mathbf{k}-\mathbf{k}'}]_{\tilde{\mu}_j, \tilde{\mu}_l}^{\tilde{\mu}_i, \tilde{\mu}_k} \left\langle \hat{c}_{-\mathbf{k}'+\frac{\mathbf{q}}{2} \tilde{\mu}_l} \hat{c}_{\mathbf{k}'+\frac{\mathbf{q}}{2} \tilde{\mu}_k} \right\rangle. \quad (4.19)$$

Since we are interested in the case of a zero total momentum of the Cooper pairs, we can set \mathbf{q} to zero, and therefore we consider $[\Delta_{\mathbf{k}, \mathbf{q}=\mathbf{0}}]_{\tilde{\mu}_j}^{\tilde{\mu}_i} \equiv [\Delta_{\mathbf{k}}]_{\tilde{\mu}_j}^{\tilde{\mu}_i}$. Under this assumption, the mean-field Hamiltonian in equation (4.12) corresponds to

$$H^{\text{MF}} = \sum_{\mathbf{k}, \sigma} \xi_{\mathbf{k}}^{\mu\nu} \hat{c}_{\mathbf{k}\mu\sigma}^\dagger \hat{c}_{\mathbf{k}\nu\sigma} + \frac{1}{2} \sum_{\mathbf{k}} \sum_{\tilde{\mu}_2, \tilde{\mu}_4} \left([\Delta_{\mathbf{k}}]_{\tilde{\mu}_4}^{\tilde{\mu}_2} \hat{c}_{\mathbf{k}\tilde{\mu}_2}^\dagger \hat{c}_{-\mathbf{k}\tilde{\mu}_4}^\dagger + \text{h.c.} \right), \quad (4.20)$$

with

$$[\Delta_{\mathbf{k}}]_{\tilde{\mu}_j}^{\tilde{\mu}_i} = \frac{1}{\mathcal{N}} \sum_{\mathbf{k}'} \sum_{\tilde{\mu}_k, \tilde{\mu}_l} [V_{\mathbf{k}-\mathbf{k}'}]_{\tilde{\mu}_j, \tilde{\mu}_l}^{\tilde{\mu}_i, \tilde{\mu}_k} \left\langle \hat{c}_{-\mathbf{k}' \tilde{\mu}_l} \hat{c}_{\mathbf{k}' \tilde{\mu}_k} \right\rangle. \quad (4.21)$$

Due to fermionic statistics, the following relations for the interaction potential hold:

$$[V_{\mathbf{R}-\mathbf{R}'}]_{\tilde{\mu}_j, \tilde{\mu}_l}^{\tilde{\mu}_i, \tilde{\mu}_k} = -[V_{\mathbf{R}-\mathbf{R}'}]_{\tilde{\mu}_i, \tilde{\mu}_l}^{\tilde{\mu}_j, \tilde{\mu}_k} = -[V_{\mathbf{R}-\mathbf{R}'}]_{\tilde{\mu}_j, \tilde{\mu}_k}^{\tilde{\mu}_i, \tilde{\mu}_l}, \quad (4.22)$$

$$[V_{\mathbf{k}-\mathbf{k}'}]_{\tilde{\mu}_j, \tilde{\mu}_l}^{\tilde{\mu}_i, \tilde{\mu}_k} = -[V_{\mathbf{k}+\mathbf{k}'}]_{\tilde{\mu}_j, \tilde{\mu}_l}^{\tilde{\mu}_i, \tilde{\mu}_k} = -[V_{-\mathbf{k}-\mathbf{k}'}]_{\tilde{\mu}_j, \tilde{\mu}_l}^{\tilde{\mu}_i, \tilde{\mu}_k}. \quad (4.23)$$

These symmetries are obtained by using the anticommutation relations for the fermionic operators in the Hamiltonian, remembering that we are summing over all orbitals and spin. For the superconducting order parameter, they lead to the symmetries

$$[\Delta_{\mathbf{R}, \mathbf{R}'}]_{\tilde{\mu}_j}^{\tilde{\mu}_i} = [\Delta_{\mathbf{R}', \mathbf{R}}]_{\tilde{\mu}_j}^{\tilde{\mu}_i} = -[\Delta_{\mathbf{R}, \mathbf{R}'}]_{\tilde{\mu}_i}^{\tilde{\mu}_j}, \quad (4.24)$$

$$[\Delta_{\mathbf{k}}]_{\tilde{\mu}_j}^{\tilde{\mu}_i} = -[\Delta_{-\mathbf{k}}]_{\tilde{\mu}_i}^{\tilde{\mu}_j}. \quad (4.25)$$

Therefore, it will be odd under quantum number exchange. As we will see in later sections, these will turn out to be very important when classifying the symmetries of the gap.

4.2 Self-consistent calculations

In this section, we will start from the previous general Hamiltonian and derive a self-consistent approach to solve for the superconducting order parameter. To do so, we realize that the mean-field decoupled Hamiltonian in equation (4.20) can be written in matrix form,

$$H^{\text{MF}} = \frac{1}{2} \sum_{\mathbf{k}} \hat{\Psi}_{\mathbf{k}}^\dagger \hat{\mathcal{H}}_{\mathbf{k}}^{\text{BdG}} \hat{\Psi}_{\mathbf{k}}, \quad \text{where} \quad \hat{\mathcal{H}}_{\mathbf{k}}^{\text{BdG}} = \begin{pmatrix} \hat{h}_{\mathbf{k}} & \hat{\Delta}_{\mathbf{k}} \\ \hat{\Delta}_{\mathbf{k}}^\dagger & -\hat{h}_{-\mathbf{k}}^T \end{pmatrix}. \quad (4.26)$$

Here, $\hat{\mathcal{H}}_{\mathbf{k}}^{\text{BdG}}$ corresponds to the Bogoliubov-de Gennes (BdG) Hamiltonian, and the spinor is given by $\hat{\Psi}_{\mathbf{k}} = (\{\hat{c}_{\mathbf{k}\tilde{\mu}_i}\}, \{\hat{c}_{-\mathbf{k}\tilde{\mu}_i}^\dagger\})^T$, including the different orbital and spin configurations. For instance, for a one-band model the spinor is given by $\hat{\Psi}_{\mathbf{k}} = (\hat{c}_{\mathbf{k}\uparrow}, \hat{c}_{\mathbf{k}\downarrow}, \hat{c}_{-\mathbf{k}\uparrow}, \hat{c}_{-\mathbf{k}\downarrow})^T$. In the previous form for the BdG Hamiltonian, $\hat{h}_{\mathbf{k}}$ and $\hat{\Delta}_{\mathbf{k}}$ are matrices in orbital and spin space, with the former one including the kinetic term and the spin-orbit coupling, whereas the latter one corresponds to the order parameter. Notice that the BdG description is redundant, since in Nambu space we are also including the hole states, consequently doubling the dimensions of the Hamiltonian.

To diagonalize the BdG Hamiltonian, we introduce the spin-generalized Bogoliubov transformations, defined by the unitary transformations

$$\begin{cases} \hat{c}_{\mathbf{k}\tilde{\mu}_i}^\dagger = \sum_n \left(u_{\mathbf{k}\tilde{\mu}_i}^{n*} \hat{\gamma}_{\mathbf{k}n}^\dagger + v_{\mathbf{k}\tilde{\mu}_i}^n \hat{\gamma}_{-\mathbf{k}n} \right), \\ \hat{c}_{\mathbf{k}\tilde{\mu}_i} = \sum_n \left(u_{\mathbf{k}\tilde{\mu}_i}^n \hat{\gamma}_{\mathbf{k}n} + v_{\mathbf{k}\tilde{\mu}_i}^{n*} \hat{\gamma}_{-\mathbf{k}n}^\dagger \right), \end{cases} \quad (4.27)$$

with $\hat{\gamma}, \hat{\gamma}^\dagger$ being the Bogoliubov operators, and where $\{u_{\mathbf{k}\tilde{\mu}_i}^n\}, \{v_{\mathbf{k}\tilde{\mu}_i}^n\}$ are the set of eigenvectors that diagonalize the Hamiltonian corresponding to the particle and the hole states, respectively. The index n sums over all eigenstates (including orbital and spin) with positive eigenenergy. With this transformation, the diagonalized Hamiltonian is given by $H = \text{GS} + \sum_{\mathbf{k},n} E_{\mathbf{k}n} \hat{\gamma}_{\mathbf{k}n}^\dagger \hat{\gamma}_{\mathbf{k}n}$, where the first term is the ground state energy.

Therefore, by introducing the transformation of equation (4.27), we can rewrite the order parameter in expression (4.21) in terms of the eigenvector components as

$$[\Delta_{\mathbf{k}}]_{\tilde{\mu}_j}^{\tilde{\mu}_i} = \frac{1}{\mathcal{N}} \sum_{\mathbf{k}'} \sum_{\tilde{\mu}_k, \tilde{\mu}_l} [V_{\mathbf{k}-\mathbf{k}'}]_{\tilde{\mu}_j, \tilde{\mu}_l}^{\tilde{\mu}_i, \tilde{\mu}_k} \sum_{n, n'} \left(\left(u_{-\mathbf{k}'\tilde{\mu}_l}^n \hat{\gamma}_{-\mathbf{k}'n} + v_{-\mathbf{k}'\tilde{\mu}_l}^{n*} \hat{\gamma}_{\mathbf{k}'n}^\dagger \right) \left(u_{\mathbf{k}'\tilde{\mu}_k}^{n'} \hat{\gamma}_{\mathbf{k}'n'} + v_{\mathbf{k}'\tilde{\mu}_k}^{n'*} \hat{\gamma}_{-\mathbf{k}'n'}^\dagger \right) \right). \quad (4.28)$$

Since the Bogoliubov operators are fermionic, they fulfill the relations $\langle \hat{\gamma}_{\mathbf{k}n'} \hat{\gamma}_{\mathbf{k}n} \rangle = 0$ and $\langle \hat{\gamma}_{\mathbf{k}n'}^\dagger \hat{\gamma}_{\mathbf{k}n} \rangle = f(E_{\mathbf{k}n}) \delta_{n, n'}$. In this expression, $f(E_{\mathbf{k}n}) = (1 + e^{\beta E_{\mathbf{k}n}})^{-1}$ is the Fermi function, where $\beta = 1/T$, considering units with $k_B = 1$. Thus, the previous equation reads

$$\begin{aligned} [\Delta_{\mathbf{k}}]_{\tilde{\mu}_j}^{\tilde{\mu}_i} &= \frac{1}{\mathcal{N}} \sum_{\mathbf{k}'} \sum_{\tilde{\mu}_k, \tilde{\mu}_l} [V_{\mathbf{k}-\mathbf{k}'}]_{\tilde{\mu}_j, \tilde{\mu}_l}^{\tilde{\mu}_i, \tilde{\mu}_k} \sum_n \left[u_{\mathbf{k}'\tilde{\mu}_k}^n v_{-\mathbf{k}'\tilde{\mu}_l}^{n*} f(E_{\mathbf{k}'n}) + u_{-\mathbf{k}'\tilde{\mu}_l}^n v_{\mathbf{k}'\tilde{\mu}_k}^{n*} (1 - f(E_{-\mathbf{k}'n})) \right] \\ &= -\frac{1}{\mathcal{N}} \sum_{\mathbf{k}'} \sum_{\tilde{\mu}_k, \tilde{\mu}_l} [V_{\mathbf{k}-\mathbf{k}'}]_{\tilde{\mu}_j, \tilde{\mu}_l}^{\tilde{\mu}_i, \tilde{\mu}_k} \sum_n u_{\mathbf{k}'\tilde{\mu}_k}^n v_{-\mathbf{k}'\tilde{\mu}_l}^{n*} \tanh\left(\frac{\beta E_{\mathbf{k}'n}}{2}\right), \end{aligned} \quad (4.29)$$

where in the last line we have used the symmetry of the interaction potential written in equation (4.23). In addition, it is common to fix the electron density, which can be also calculated self-consistently by introducing the Bogoliubov transformations, and is given by

$$\begin{aligned} \langle n \rangle &= \frac{1}{\mathcal{N}} \sum_{\mathbf{k}, \mu, \sigma} \langle \hat{c}_{\mathbf{k}\mu\sigma}^\dagger \hat{c}_{\mathbf{k}\mu\sigma} \rangle \\ &= \frac{1}{\mathcal{N}} \sum_{\mathbf{k}, \mu, \sigma} \sum_n \left[|u_{\mathbf{k}\mu\sigma}^n|^2 f(E_{\mathbf{k}n}) + |v_{\mathbf{k}\mu\sigma}^n|^2 (1 - f(E_{-\mathbf{k}n})) \right]. \end{aligned} \quad (4.30)$$

Similarly, in the real space representation, the Bogoliubov transformations correspond to

$$\begin{cases} \hat{c}_{\mathbf{R}\tilde{\mu}_i}^\dagger = \sum_n (u_{\mathbf{R}\tilde{\mu}_i}^{n*} \hat{\gamma}_n^\dagger + v_{\mathbf{R}\tilde{\mu}_i}^n \hat{\gamma}_n), \\ \hat{c}_{\mathbf{R}\tilde{\mu}_i} = \sum_n (u_{\mathbf{R}\tilde{\mu}_i}^n \hat{\gamma}_n + v_{\mathbf{R}\tilde{\mu}_i}^{n*} \hat{\gamma}_n^\dagger). \end{cases} \quad (4.31)$$

Replacing them in equation (4.8), the order parameter in the real space basis becomes

$$\begin{aligned} [\Delta_{\mathbf{R},\mathbf{R}'}]_{\tilde{\mu}_j}^{\tilde{\mu}_i} &= \sum_{\tilde{\mu}_k,\tilde{\mu}_l} [V_{\mathbf{R}-\mathbf{R}'}]_{\tilde{\mu}_j,\tilde{\mu}_l}^{\tilde{\mu}_i,\tilde{\mu}_k} \sum_n \left[u_{\mathbf{R}\tilde{\mu}_k}^n v_{\mathbf{R}'\tilde{\mu}_l}^{n*} f(E_n) + u_{\mathbf{R}'\tilde{\mu}_l}^n v_{\mathbf{R}\tilde{\mu}_k}^{n*} (1 - f(E_n)) \right] \\ &= \sum_{\tilde{\mu}_k,\tilde{\mu}_l} [V_{\mathbf{R}-\mathbf{R}'}]_{\tilde{\mu}_j,\tilde{\mu}_l}^{\tilde{\mu}_i,\tilde{\mu}_k} \sum_n \left[u_{\mathbf{R}\tilde{\mu}_k}^n v_{\mathbf{R}'\tilde{\mu}_l}^{n*} f(E_n) - u_{\mathbf{R}'\tilde{\mu}_k}^n v_{\mathbf{R}\tilde{\mu}_l}^{n*} (1 - f(E_n)) \right], \end{aligned} \quad (4.32)$$

using the symmetry in equation (4.22) for the interaction potential in real space. In this case, the electron density is given by

$$\begin{aligned} \langle n \rangle &= \frac{1}{\mathcal{N}} \sum_{\mathbf{R},\mu,\sigma} \langle \hat{c}_{\mathbf{R}\mu\sigma}^\dagger \hat{c}_{\mathbf{R}\mu\sigma} \rangle \\ &= \frac{1}{\mathcal{N}} \sum_{\mathbf{R},\mu,\sigma} \sum_n \left[|u_{\mathbf{R}\mu\sigma}^n|^2 f(E_n) + |v_{\mathbf{R}\mu\sigma}^n|^2 (1 - f(E_n)) \right]. \end{aligned} \quad (4.33)$$

Finally, we need to describe the inclusion of non-magnetic impurities. As previously stated, we first want to study the homogeneous case, and therefore it is only necessary to solve for the order parameter in momentum space. Nevertheless, since we also want to see how impurities affect our system, we need to add the following term to the Hamiltonian:

$$H_{\text{imp}} = V_{\text{imp}} \sum_{\mathbf{R},\mu,\sigma} \hat{c}_{\mathbf{R}\mu\sigma}^\dagger \hat{c}_{\mathbf{R}\mu\sigma} \delta_{\mathbf{R},\mathbf{R}_{\text{imp}}}, \quad (4.34)$$

where we have assumed that the Coulomb interaction between electrons and the impurity is screened at scales larger than the lattice spacing, so that the local potential is given by $V_{\mathbf{R}}^{\text{imp}} = V_{\text{imp}} \delta_{\mathbf{R},\mathbf{R}_{\text{imp}}}$, with $V_{\text{imp}} > 0$. This implements an impurity as a repulsive potential in a certain lattice site \mathbf{R}_{imp} , considering for simplicity that V_{imp} is the same for all orbitals.

4.3 Numerical implementation

In this section, we describe the numerical implementation of the self-consistent calculations. To achieve this purpose, we have programmed a code in Python. First of all, we deal with the implementation of the momentum space self-consistent code. In order to obtain a numerical solution, we introduce the discretization of the momentum space k_x and k_y , and we give a number of values N to these variables in the first Brillouin zone (between 0 to 2π). Therefore, we construct a $N \times N$ grid that introduces the partitions in momentum. In addition, we give an initial guess for the order parameter components, introduced as a random number between 0 and 1, with both real and imaginary parts.

Secondly, the sum over all \mathbf{k} values (corresponding to N^2) is performed. We introduce the definition of the kinetic terms, which will generally depend on \mathbf{k} , so that we build the normal state Hamiltonian. From the assigned initial guess, the BdG Hamiltonian at each \mathbf{k} value can be constructed and diagonalized, obtaining the eigensystem

$$\hat{\mathcal{H}}_{\mathbf{k}}^{\text{BdG}} \begin{pmatrix} \{u_{\mathbf{k}\bar{\mu}}^n\} \\ \{v_{-\mathbf{k}\bar{\mu}}^n\} \end{pmatrix} = E_{\mathbf{k}n} \begin{pmatrix} \{u_{\mathbf{k}\bar{\mu}}^n\} \\ \{v_{-\mathbf{k}\bar{\mu}}^n\} \end{pmatrix}, \quad (4.35)$$

where $\{u_{\bar{\mu}}\}, \{v_{\bar{\mu}}\}$ account for the vector components including all possible orbital/spin configurations. It is important to notice that in the wave-vector representation the dimension of the BdG matrix is given by $2 \times d_{s/o}$, where the 2 comes from Nambu space and $d_{s/o}$ refers to the dimension of the spin/orbital space. For instance, in the case of Sr_2RuO_4 , since we have 3 orbitals, $d_{s/o} = 6$. With the eigenvalues and eigenvectors, we can find the order parameter and the electron density by summing over all momentum partitions, according to equations (4.29), (4.30).

Thirdly, we impose the convergence condition, which in our case corresponds to an agreement of 0.001 meV. Therefore, the program checks if the previous mean field minus the newly calculated order parameter are within this precision, and the same between the calculated electron density and the fixed electron density. It is important to notice that by tuning the chemical potential μ_0 we can fix the number of electrons in the system. Thus, since in the case of Sr_2RuO_4 we know that it corresponds to 4, we can adjust the chemical potential in the self-consistent loop of the code in order to fix it. Therefore, if the numbers are not within the precision, the solution found is imposed as the new initial guess and the chemical potential is adjusted in the new iteration as

$$\mu = \mu_{\text{old}} + \frac{1}{2}(n_{\text{wanted}} - n_{\text{calculated}}), \quad (4.36)$$

in order to keep the electron density close the value that we want, with μ_{old} being the chemical potential used in the previous iteration. The second and the third steps are repeated until convergence is reached.

Finally, when the difference between the order parameters in the current and the previous iterations is smaller than the precision set, as well as for the electron density, a convergent solution is obtained.

In real space, the implementation is slightly different. In this case, to solve the problem numerically, we set up a square grid with dimensions $N \times N$ and choose to incorporate periodic boundary conditions. Within this description, a generalization of the previous eigensystem

presented in equation (4.35) is needed:

$$\hat{\mathcal{H}}^{\text{BdG}} \begin{pmatrix} \{u_{\mu}^n(1)\} \\ \cdot \\ \cdot \\ \{u_{\mu}^n(N^2)\} \\ \{v_{\mu}^n(1)\} \\ \cdot \\ \cdot \\ \{v_{\mu}^n(N^2)\} \end{pmatrix} = E_n \begin{pmatrix} \{u_{\mu}^n(1)\} \\ \cdot \\ \cdot \\ \{u_{\mu}^n(N^2)\} \\ \{v_{\mu}^n(1)\} \\ \cdot \\ \cdot \\ \{v_{\mu}^n(N^2)\} \end{pmatrix}, \quad (4.37)$$

where $(1), \dots, (N)$ refers to each lattice site. Apart from this, the self-consistent procedure is the same, and a convergence condition is also imposed. From the previous equation, we can immediately see that now the dimension of the BdG matrix corresponds to $2N^2 \times 2N^2 \times d_{s/o}$. Solving these equations is numerically costly, and therefore the description in the wave-vector basis is preferred when considering a homogeneous system. However, the real space description becomes crucial in the impurities studies.

Chapter 5

Systems with on-site interactions

In this chapter, we consider a system with an on-site attractive interaction, giving rise to superconductivity. In this case, the interaction potential in real space has the form

$$[V_{\mathbf{R}-\mathbf{R}'}]_{\tilde{\mu}_j, \tilde{\mu}_l}^{\tilde{\mu}_i, \tilde{\mu}_k} = [U]_{\tilde{\mu}_j, \tilde{\mu}_l}^{\tilde{\mu}_i, \tilde{\mu}_k} \delta_{\mathbf{R}, \mathbf{R}'}. \quad (5.1)$$

Therefore, the mean-field Hamiltonian in momentum space in equation (4.20) is now given by

$$H^{\text{MF}} = \sum_{\mathbf{k}, \sigma} \xi_{\mathbf{k}}^{\mu\nu} \hat{c}_{\mathbf{k}\mu\sigma}^\dagger \hat{c}_{\mathbf{k}\nu\sigma} + \frac{1}{2} \sum_{\mathbf{k}} \sum_{\tilde{\mu}_2, \tilde{\mu}_4} \left([\Delta]_{\tilde{\mu}_4}^{\tilde{\mu}_2} \hat{c}_{\mathbf{k}\tilde{\mu}_2}^\dagger \hat{c}_{-\mathbf{k}\tilde{\mu}_4}^\dagger + \text{h.c.} \right), \quad (5.2)$$

where the superconducting order parameter in equation (4.29) corresponds to

$$[\Delta]_{\tilde{\mu}_j}^{\tilde{\mu}_i} = -\frac{1}{\mathcal{N}} \sum_{\mathbf{k}'} \sum_{\tilde{\mu}_k, \tilde{\mu}_l} [U]_{\tilde{\mu}_j, \tilde{\mu}_l}^{\tilde{\mu}_i, \tilde{\mu}_k} \sum_n u_{\mathbf{k}'\tilde{\mu}_k}^n v_{-\mathbf{k}'\tilde{\mu}_l}^{n*} \tanh\left(\frac{\beta E_{\mathbf{k}'n}}{2}\right). \quad (5.3)$$

Consequently, recalling equation (4.25), since now the order parameter is \mathbf{k} -independent, due to fermionic statistics it fulfills

$$[\Delta]_{\tilde{\mu}_j}^{\tilde{\mu}_i} = -[\Delta]_{\tilde{\mu}_i}^{\tilde{\mu}_j}. \quad (5.4)$$

Similarly, in the real space representation, the Hamiltonian introduced in equation (4.9) can be written as

$$H^{\text{MF}} = - \sum_{\mathbf{R}, \mathbf{R}'} \sum_{\mu, \nu} \sum_{\sigma} (t_{\mathbf{R}, \mathbf{R}'}^{\mu, \nu} + \mu_0 \delta_{\mathbf{R}, \mathbf{R}'} \delta_{\mu\nu}) \hat{c}_{\mathbf{R}\mu\sigma}^\dagger \hat{c}_{\mathbf{R}'\nu\sigma} + \frac{1}{2} \sum_{\mathbf{R}} \sum_{\tilde{\mu}_2, \tilde{\mu}_4} ([\Delta_{\mathbf{R}}]_{\tilde{\mu}_4}^{\tilde{\mu}_2} \hat{c}_{\mathbf{R}\tilde{\mu}_2}^\dagger \hat{c}_{\mathbf{R}\tilde{\mu}_4}^\dagger + \text{h.c.}), \quad (5.5)$$

where in this case equation (4.32) simply becomes

$$[\Delta_{\mathbf{R}}]_{\tilde{\mu}_j}^{\tilde{\mu}_i} = - \sum_{\tilde{\mu}_k, \tilde{\mu}_l} [U]_{\tilde{\mu}_j, \tilde{\mu}_l}^{\tilde{\mu}_i, \tilde{\mu}_k} \sum_n u_{\mathbf{R}\tilde{\mu}_k}^n v_{\mathbf{R}\tilde{\mu}_l}^{n*} \tanh\left(\frac{\beta E_n}{2}\right). \quad (5.6)$$

Therefore, with these expressions we are able to solve self-consistently for the order parameter. We will consider first a simple one-band model, and then we will generalize the previous case to a multi-orbital toy model system of two bands. Finally, an effective model for Sr_2RuO_4 with on-site interactions is also studied. For all systems considered in this part of the thesis, the self-consistent numerical approach is solved for a homogeneous system in momentum space, and then impurities are incorporated in the real space problem.

5.1 One-band model

In the first model presented we consider a single orbital. Hence, we only have the spin dependence in the interaction potential, which corresponds to

$$[U]_{\bar{\sigma},\bar{\sigma}}^{\sigma,\sigma} = g, \quad [U]_{\bar{\sigma},\bar{\sigma}}^{\bar{\sigma},\bar{\sigma}} = -[U]_{\bar{\sigma},\bar{\sigma}}^{\sigma,\sigma} = -g, \quad (5.7)$$

where $\bar{\sigma}$ denotes the opposite spin as σ . Since we want it to be attractive, we will always consider $g < 0$. Importantly, the previous interaction fulfills the symmetries in equation (4.23) due to fermionic statistics.

In this simple case, the Hamiltonian provided in equation (5.2) in wave-vector space reads

$$\begin{aligned} H^{\text{MF}} &= \sum_{\substack{\mathbf{k},\sigma \\ \mu,\nu}} \xi_{\mathbf{k}}^{\mu\nu} \hat{c}_{\mathbf{k}\mu\sigma}^\dagger \hat{c}_{\mathbf{k}\nu\sigma} + \frac{1}{2} \sum_{\mathbf{k},\sigma} \left([\Delta]_{\bar{\sigma}}^\sigma \hat{c}_{\mathbf{k}\sigma}^\dagger \hat{c}_{-\mathbf{k}\bar{\sigma}} + \text{h.c.} \right) \\ &= \sum_{\substack{\mathbf{k},\sigma \\ \mu,\nu}} \xi_{\mathbf{k}}^{\mu\nu} \hat{c}_{\mathbf{k}\mu\sigma}^\dagger \hat{c}_{\mathbf{k}\nu\sigma} + \sum_{\mathbf{k}} \left([\Delta]_{\downarrow}^\uparrow \hat{c}_{\mathbf{k}\uparrow}^\dagger \hat{c}_{-\mathbf{k}\downarrow} + \text{h.c.} \right), \end{aligned} \quad (5.8)$$

where we have used the symmetry in equation (5.4) for the order parameter. Using the form for the spinor $\hat{\Psi}_{\mathbf{k}} = \left(\hat{c}_{\mathbf{k}\uparrow}, \hat{c}_{\mathbf{k}\downarrow}, \hat{c}_{-\mathbf{k}\uparrow}^\dagger, \hat{c}_{-\mathbf{k}\downarrow}^\dagger \right)^T$, we can write the Hamiltonian as

$$H = \frac{1}{2} \hat{\Psi}^\dagger \hat{\mathcal{H}}_{\mathbf{k}}^{\text{BdG}} \hat{\Psi}, \quad \text{where} \quad \hat{\mathcal{H}}_{\mathbf{k}}^{\text{BdG}} = \begin{pmatrix} \xi_{\mathbf{k}} & 0 & 0 & [\Delta]_{\downarrow}^\uparrow \\ 0 & \xi_{\mathbf{k}} & -[\Delta]_{\downarrow}^\uparrow & 0 \\ 0 & -([\Delta]_{\downarrow}^\uparrow)^* & -\xi_{-\mathbf{k}} & 0 \\ ([\Delta]_{\downarrow}^\uparrow)^* & 0 & 0 & -\xi_{-\mathbf{k}} \end{pmatrix}. \quad (5.9)$$

For the redundant BdG Hamiltonian, due to particle-hole symmetry the eigenenergies would correspond to $(E_{n=1}, E_{n=2}, -E_{n=2}, -E_{n=1})$. For the eigenvectors, we obtain $(\{u_{\mathbf{k}\uparrow}^n, u_{\mathbf{k}\downarrow}^n, v_{-\mathbf{k}\uparrow}^n, v_{-\mathbf{k}\downarrow}^n\})$ for each eigenvalue E_n . Therefore, from equation (4.35) we can see that we want to solve the eigensystem

$$\hat{\mathcal{H}}_{\mathbf{k}}^{\text{BdG}} \begin{pmatrix} u_{\mathbf{k}\uparrow}^n \\ u_{\mathbf{k}\downarrow}^n \\ v_{-\mathbf{k}\uparrow}^n \\ v_{-\mathbf{k}\downarrow}^n \end{pmatrix} = E_{kn} \begin{pmatrix} u_{\mathbf{k}\uparrow}^n \\ u_{\mathbf{k}\downarrow}^n \\ v_{-\mathbf{k}\uparrow}^n \\ v_{-\mathbf{k}\downarrow}^n \end{pmatrix}. \quad (5.10)$$

Since in this simple model we have no spin-orbit coupling, we can rewrite equation (5.9) as two decoupled equations,

$$\begin{pmatrix} \xi_{\mathbf{k}} & [\Delta]_{\downarrow}^{\uparrow} \\ ([\Delta]_{\downarrow}^{\uparrow})^* & -\xi_{\mathbf{k}} \end{pmatrix} \begin{pmatrix} u_{\mathbf{k}\uparrow}^n \\ v_{-\mathbf{k}\downarrow}^n \end{pmatrix} = E_{\mathbf{k}n} \begin{pmatrix} u_{\mathbf{k}\uparrow}^n \\ v_{-\mathbf{k}\downarrow}^n \end{pmatrix}, \quad (5.11)$$

$$\begin{pmatrix} \xi_{\mathbf{k}} & -[\Delta]_{\downarrow}^{\uparrow} \\ -([\Delta]_{\downarrow}^{\uparrow})^* & -\xi_{\mathbf{k}} \end{pmatrix} \begin{pmatrix} u_{\mathbf{k}\downarrow}^n \\ v_{-\mathbf{k}\uparrow}^n \end{pmatrix} = E_{\mathbf{k}n} \begin{pmatrix} u_{\mathbf{k}\downarrow}^n \\ v_{-\mathbf{k}\uparrow}^n \end{pmatrix}. \quad (5.12)$$

Therefore, since both equations are related by the symmetry

$$\begin{Bmatrix} E_{\mathbf{k}n} \\ u_{\mathbf{k}\uparrow}^n \\ v_{-\mathbf{k}\downarrow}^n \end{Bmatrix} \longrightarrow \begin{Bmatrix} -E_{\mathbf{k}n} \\ v_{-\mathbf{k}\uparrow}^{n*} \\ u_{\mathbf{k}\downarrow}^{n*} \end{Bmatrix}, \quad (5.13)$$

we only need to solve the Hamiltonian in a 2×2 subspace. We choose to take the reduced spinor $\hat{\Psi}_{\mathbf{k},\text{red.}} = (\hat{c}_{\mathbf{k}\uparrow}, \hat{c}_{-\mathbf{k}\downarrow}^{\dagger})^T$, with the corresponding Hamiltonian

$$\hat{\mathcal{H}}_{\mathbf{k},\text{red.}}^{\text{BdG}} = \begin{pmatrix} \xi_{\mathbf{k}} & [\Delta]_{\downarrow}^{\uparrow} \\ ([\Delta]_{\downarrow}^{\uparrow})^* & -\xi_{-\mathbf{k}} \end{pmatrix}. \quad (5.14)$$

Using the previous symmetry, in momentum space the order parameter of equation (5.3) is given by

$$\begin{aligned} [\Delta]_{\downarrow}^{\uparrow} &= -\sum_{\mathbf{k}'} \sum_{\sigma} [U]_{\downarrow,\bar{\sigma}}^{\uparrow,\sigma} \sum_n u_{\mathbf{k}'\sigma}^n v_{-\mathbf{k}'\bar{\sigma}}^{n*} \tanh\left(\frac{\beta E_{\mathbf{k}'n}}{2}\right) \\ &= -2g \sum_{\mathbf{k}'} \sum_n u_{\mathbf{k}'\uparrow}^n v_{-\mathbf{k}'\downarrow}^{n*} \tanh\left(\frac{\beta E_{\mathbf{k}'n}}{2}\right), \end{aligned} \quad (5.15)$$

whereas in real space equation (5.6) corresponds to

$$\begin{aligned} [\Delta_{\mathbf{R}}]_{\downarrow}^{\uparrow} &= -\sum_{\mathbf{k}'} \sum_{\sigma} [U]_{\downarrow,\bar{\sigma}}^{\uparrow,\sigma} \sum_n u_{\mathbf{R}\sigma}^n v_{\mathbf{R}\bar{\sigma}}^{n*} \tanh\left(\frac{\beta E_n}{2}\right) \\ &= -2g \sum_n u_{\mathbf{R}\uparrow}^n v_{\mathbf{R}\downarrow}^{n*} \tanh\left(\frac{\beta E_n}{2}\right). \end{aligned} \quad (5.16)$$

Therefore, with these expressions we can solve self-consistently for the order parameter in both spaces. With this purpose, we consider a simple dispersion of the form $\xi_{\mathbf{k}} = -2t(\cos k_x + \cos k_y)$. In Figure 5.1 we show the relative order parameter $[\Delta_{\mathbf{R}}]_{\downarrow}^{\uparrow}/[\Delta]_{\downarrow}^{\uparrow}$ in the presence of an impurity in the center site, $V_{\mathbf{R}}^{\text{imp}} = V_{\text{imp}}\delta_{\mathbf{R},\mathbf{0}}$. By plotting the relative order parameter we can compare the effects of the impurity with respect to the homogeneous case. Indeed, we can verify that the order parameter is the same in both cases except in the vicinity of the impurity, and we can see that at the center sites the gap is suppressed due to the effect of the defect.

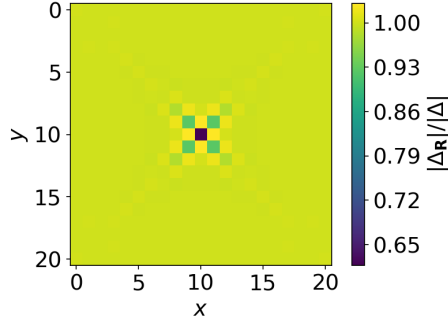


Figure 5.1: Real space superconducting order parameter $|\Delta_{\mathbf{R}}|$ in a one-band model with a non-magnetic impurity at the center site, normalized with respect to the homogeneous value $|\Delta|$. We consider a 21×21 square lattice, with $g = -2t$, $V_{\text{imp}} = t$ and fix the electron density to $\langle n \rangle = 0.75$, with $t = 1$ meV.

Moreover, the impurity has an effect only in the closer lattice sites. This is a consequence of the coherence length ξ_0 , which represents the physical size of the Cooper pair bound state in the BCS theory. This length is closely related to the gap [49] by

$$\xi_0 = \frac{\hbar v_F}{\pi \Delta}. \quad (5.17)$$

Therefore, since in our case the values of the gap are around 1 meV, the coherence length is very short, so that only an effect in the sites closer to the impurity is seen.

The same result for the momentum space order parameter can be derived using the reduced spinor notation $\hat{\psi}_{\mathbf{k}, \text{red}} = (\hat{c}_{\mathbf{k}\uparrow}, \hat{c}_{-\mathbf{k}\downarrow}^\dagger)$, as shown in Appendix A, noticing that in the system considered the condition $\hat{\mathcal{H}}_{-\mathbf{k}}^{\text{BdG}} = \hat{\mathcal{H}}_{\mathbf{k}}^{\text{BdG}}$ is fulfilled, and for the energies $E_{-\mathbf{k}n} = E_{\mathbf{k}n}$. Thus, recalling equation (4.35), we can see that in these cases $u_{-\mathbf{k}\tilde{\mu}}^n = u_{\mathbf{k}\tilde{\mu}}^n$ and $v_{-\mathbf{k}\tilde{\mu}}^n = v_{\mathbf{k}\tilde{\mu}}^n$.

5.2 Two-band model

As the following step towards building a system with three orbitals, we choose a simple two-orbital model including the interaction potentials in equation (3.7). Assuming rotational symmetry, we can take $U' = U - 2J$ and $J' = J$. Numerically, the easiest way to incorporate this in the program is by introducing 4×4 matrices including the interactions for a certain order parameter component. For instance, to calculate $[\Delta]_{\alpha\downarrow}^{\alpha\uparrow}$ we introduce the 4×4 matrix $[U]_{\alpha\downarrow, \nu\sigma'}^{\alpha\uparrow, \mu\sigma}$ encoding all the interactions in orbital and spin space for this particular component.

In our simple model, we consider no spin-orbit coupling and an intraorbital dispersion of the form $\xi_{\mathbf{k}}^{\nu\nu} = -2t_\nu(\cos k_x + \cos k_y) - \mu$, whereas the interorbital dispersion is fixed to $\xi_{\mathbf{k}}^{\mu\nu} = 0.01t$. We denote the two orbitals as α, β , so that the possible values for orbital and spin are $\{\tilde{\mu}_i\} = \{\alpha \uparrow, \alpha \downarrow, \beta \uparrow, \beta \downarrow\}$. Hence, the matrices for the kinetic term and the superconducting order parameter entering in the BdG equation (4.26) would be 4×4 . Considering the Pauli matrices, given in Appendix B, as the basis for a 2×2 subspace, we can adopt the following notation: $\tau \rightarrow$ Nambu, $\kappa \rightarrow$ orbital, and $\sigma \rightarrow$ spin. Thus, considering the kinetic term

$$\hat{\xi} = \begin{pmatrix} \xi^{\alpha\alpha} & \xi^{\alpha\beta} \\ (\xi^{\alpha\beta})^* & \xi^{\beta\beta} \end{pmatrix} \otimes \mathbb{1}_\sigma, \quad (5.18)$$

the BdG Hamiltonian in equation (4.26) can be written as

$$\hat{\mathcal{H}}_{\mathbf{k}}^{\text{BdG}} = \tau_z \left[\frac{\xi_{\mathbf{k}}^{\alpha\alpha} + \xi_{\mathbf{k}}^{\beta\beta}}{2} \mathbb{1}_\kappa + \frac{\xi_{\mathbf{k}}^{\alpha\alpha} - \xi_{\mathbf{k}}^{\beta\beta}}{2} \kappa_z + \text{Re}(\xi_{\mathbf{k}}^{\alpha\beta}) \kappa_x \right] \mathbb{1}_\sigma - \text{Im}(\xi_{\mathbf{k}}^{\alpha\beta}) \kappa_y \mathbb{1}_\sigma + \tau_x \frac{\hat{\Delta} + \hat{\Delta}^\dagger}{2} + i\tau_y \frac{\hat{\Delta} - \hat{\Delta}^\dagger}{2}, \quad (5.19)$$

where two matrices together implicitly imply a tensor product (\otimes) between them. Therefore, the total Hamiltonian would be 8×8 in \mathbf{k} -space, so that for each positive eigenenergy E_n the corresponding eigenvector will have the following form:

$$(u_{\alpha\uparrow}^n, u_{\alpha\downarrow}^n, u_{\beta\uparrow}^n, u_{\beta\downarrow}^n, v_{\alpha\uparrow}^n, v_{\alpha\downarrow}^n, v_{\beta\uparrow}^n, v_{\beta\downarrow}^n). \quad (5.20)$$

Similarly, since in real space the Hamiltonian is $8N^2 \times 8N^2$, the eigenvectors will have $8N^2$ entries. Comparing with the previous components, the form will be the same except that now we have the subspace corresponding to each lattice site, so that it will be

$$(u_{\alpha\uparrow}^n(1), \dots, u_{\alpha\uparrow}^n(N^2), u_{\alpha\downarrow}^n(1), \dots, u_{\alpha\downarrow}^n(N^2), u_{\beta\uparrow}^n(1), \dots, u_{\beta\uparrow}^n(N^2), u_{\beta\downarrow}^n(1), \dots, u_{\beta\downarrow}^n(N^2), \\ v_{\alpha\uparrow}^n(1), \dots, v_{\alpha\uparrow}^n(N^2), v_{\alpha\downarrow}^n(1), \dots, v_{\alpha\downarrow}^n(N^2), v_{\beta\uparrow}^n(1), \dots, v_{\beta\uparrow}^n(N^2), v_{\beta\downarrow}^n(1), \dots, v_{\beta\downarrow}^n(N^2)). \quad (5.21)$$

For the order parameter matrix, taking into consideration equation (5.4), it is highly advantageous to use the symmetry $\hat{\Delta} = -\hat{\Delta}^T$, so that it is given by the general form

$$\hat{\Delta} = \begin{pmatrix} 0 & [\Delta]_{\alpha\downarrow}^{\alpha\uparrow} & [\Delta]_{\beta\uparrow}^{\alpha\uparrow} & [\Delta]_{\beta\downarrow}^{\alpha\uparrow} \\ -[\Delta]_{\alpha\downarrow}^{\alpha\uparrow} & 0 & [\Delta]_{\beta\uparrow}^{\alpha\downarrow} & [\Delta]_{\beta\downarrow}^{\alpha\downarrow} \\ -[\Delta]_{\beta\uparrow}^{\alpha\uparrow} & -[\Delta]_{\beta\uparrow}^{\alpha\downarrow} & 0 & [\Delta]_{\beta\downarrow}^{\beta\uparrow} \\ -[\Delta]_{\beta\downarrow}^{\alpha\uparrow} & -[\Delta]_{\beta\downarrow}^{\alpha\downarrow} & -[\Delta]_{\beta\downarrow}^{\beta\uparrow} & 0 \end{pmatrix}. \quad (5.22)$$

In terms of the Pauli matrices, the expression above can be rewritten as

$$\hat{\Delta} = i\mathbb{1}_\kappa \frac{[\Delta]_{\alpha\downarrow}^{\alpha\uparrow} + [\Delta]_{\beta\downarrow}^{\beta\uparrow}}{2} \sigma_y + i\kappa_z \frac{[\Delta]_{\alpha\downarrow}^{\alpha\uparrow} - [\Delta]_{\beta\downarrow}^{\beta\uparrow}}{2} \sigma_y + i\kappa_y \frac{[\Delta]_{\beta\uparrow}^{\alpha\uparrow} + [\Delta]_{\beta\downarrow}^{\alpha\downarrow}}{2} \mathbb{1}_\sigma \\ + i\kappa_y \frac{[\Delta]_{\beta\uparrow}^{\alpha\uparrow} - [\Delta]_{\beta\downarrow}^{\alpha\downarrow}}{2} \sigma_z + i\kappa_y \frac{[\Delta]_{\beta\downarrow}^{\alpha\uparrow} + [\Delta]_{\beta\uparrow}^{\alpha\downarrow}}{2} \sigma_x + i\kappa_x \frac{[\Delta]_{\beta\downarrow}^{\alpha\uparrow} - [\Delta]_{\beta\uparrow}^{\alpha\downarrow}}{2} \sigma_y. \quad (5.23)$$

Using the common notation $\hat{\Delta} = i(\hat{\psi} + \hat{\mathbf{d}} \cdot \boldsymbol{\sigma})\sigma_y$ for the superconducting order parameter, we can distinguish the spin-singlet ($\hat{\psi}$) and spin-triplet ($\hat{\mathbf{d}} \cdot \boldsymbol{\sigma}$) contributions, which correspond to

$$\hat{\psi} = \mathbb{1}_\kappa \frac{[\Delta]_{\alpha\downarrow}^{\alpha\uparrow} + [\Delta]_{\beta\downarrow}^{\beta\uparrow}}{2} \mathbb{1}_\sigma + \kappa_z \frac{[\Delta]_{\alpha\downarrow}^{\alpha\uparrow} - [\Delta]_{\beta\downarrow}^{\beta\uparrow}}{2} \mathbb{1}_\sigma + \kappa_x \frac{[\Delta]_{\beta\downarrow}^{\alpha\uparrow} - [\Delta]_{\beta\downarrow}^{\alpha\downarrow}}{2} \mathbb{1}_\sigma, \quad (5.24)$$

$$\hat{\mathbf{d}} \cdot \boldsymbol{\sigma} = \kappa_y \frac{[\Delta]_{\beta\uparrow}^{\alpha\uparrow} + [\Delta]_{\beta\downarrow}^{\alpha\downarrow}}{2} \sigma_y - i\kappa_y \frac{[\Delta]_{\beta\uparrow}^{\alpha\uparrow} - [\Delta]_{\beta\downarrow}^{\alpha\downarrow}}{2} \sigma_x + i\kappa_y \frac{[\Delta]_{\beta\downarrow}^{\alpha\uparrow} + [\Delta]_{\beta\uparrow}^{\alpha\downarrow}}{2} \sigma_z. \quad (5.25)$$

Considering that in the case of on-site interactions the order parameter matrix does not depend on \mathbf{k} , $\hat{\psi}$ and $\hat{\mathbf{d}} \cdot \boldsymbol{\sigma}$ are thus even under $\mathbf{k} \rightarrow -\mathbf{k}$. Nevertheless, they transform differently under the exchange of orbital indices, so that $\hat{\psi}^T = \hat{\psi}$ and $\hat{d}_i^T = -\hat{d}_i$, for $i = x, y, z$.

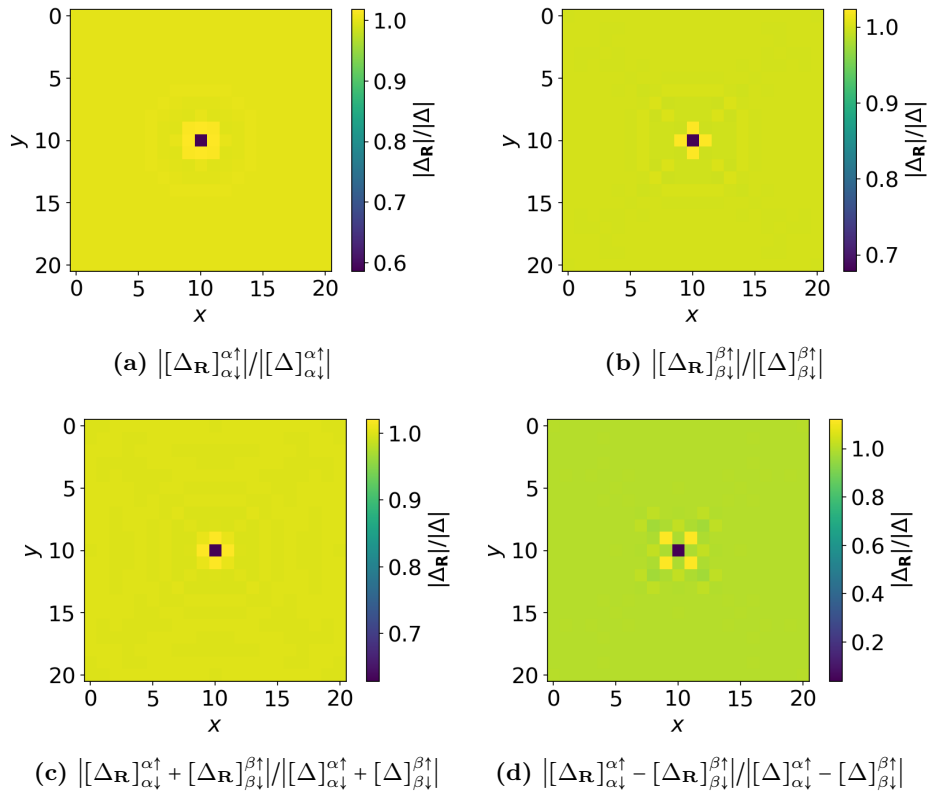


Figure 5.2: Real space superconducting order parameter $|\Delta_{\mathbf{R}}|$ in a two-band model with a non-magnetic impurity at the center of the two orbitals, normalized with respect to the homogeneous value $|\Delta|$. We consider a 21×21 square lattice, with $t_\alpha = t$, $t_\beta = 2t$, $U = -1.5t$, $J = U/3$, $V_{\text{imp}} = t$ and fix the electron density to $\langle n \rangle = 0.75$, with $t = 1$ meV. The particular orbital and spin components plotted are detailed in each caption.

In Figure 5.2, we show the results for the order parameters in real space normalized with the \mathbf{k} -space homogeneous value in the presence of an impurity in the center site. Figures 5.2a and 5.2b are different since we take a distinct dispersion for each orbital, as detailed in the caption. Similar to the one-band model, in this case also the coherence length is also very short, as impurities only have an effect in the closer the lattice sites.

Figures 5.2c and 5.2d correspond to two of the combinations for the order parameter components obtained in equation (5.24). Importantly, these combinations show a different pattern due to the impurity effect, although both of them correspond to orbital-triplet and spin-singlet character. The distinction of the singlet and triplet contributions in the order parameter will be very convenient in the following section, since we will be able identify how each contribution behaves under the particular point group relevant to Sr_2RuO_4 .

5.3 Three-band model: effective model for Sr_2RuO_4

In the case of a three-orbital model, we can write the multi-orbital Hamiltonian in equation (5.2) as

$$H = \sum_{\mathbf{k}} \sum_{\mu\nu} \sum_{\sigma} \hat{c}_{\mathbf{k}\mu\sigma}^{\dagger} h_{\mathbf{k}}^{\mu\nu} \hat{c}_{\mathbf{k}\nu\sigma} + \sum_{\mathbf{k}} \sum_{\tilde{\mu}_2\tilde{\mu}_4} (\hat{c}_{\mathbf{k}\tilde{\mu}_2}^{\dagger} [\Delta]_{\tilde{\mu}_4}^{\tilde{\mu}_2} \hat{c}_{-\mathbf{k}\tilde{\mu}_4}^{\dagger} + \text{h.c.}), \quad (5.26)$$

where $h_{\mathbf{k}}^{\mu\nu}$ denotes the normal state Hamiltonian including the electronic dispersions and spin-orbit coupling.

To implement a simple three-band model, we consider only the bare electron-electron interactions explained in Chapter 3, corresponding to equation (3.7). As in the two-band model case, the easiest way to incorporate these interactions numerically is to introduce the 6×6 matrices including the interactions for each order parameter component.

Remembering that for Sr_2RuO_4 we need to consider the three t_{2g} orbitals, we adopt the following notation: $\mu = \{xz, yz, xy\} \equiv \{1, 2, 3\}$. Moreover, when two matrices are together it is again implicitly understood as a tensor product between them, $\tau_k \otimes \lambda_i \otimes \sigma_j \equiv \tau_k \lambda_i \sigma_j$. In this case, since we have three orbitals, a good basis in orbital space is given by the 8 Gell-Mann matrices together with the identity matrix, which are written in Appendix C. Since they form a basis, we can write each element of a 3×3 matrix as a combination of these 9 matrices, as also shown in equation (B.4).

In the three-band model, the spinor corresponds to

$$\hat{\Psi}_{\mathbf{k}} = \left(\hat{c}_{1\uparrow}(\mathbf{k}), \hat{c}_{1\downarrow}(\mathbf{k}), \hat{c}_{2\uparrow}(\mathbf{k}), \hat{c}_{2\downarrow}(\mathbf{k}), \hat{c}_{3\uparrow}(\mathbf{k}), \hat{c}_{3\downarrow}(\mathbf{k}), \right. \\ \left. \hat{c}_{1\uparrow}^{\dagger}(-\mathbf{k}), \hat{c}_{1\downarrow}^{\dagger}(-\mathbf{k}), \hat{c}_{2\uparrow}^{\dagger}(-\mathbf{k}), \hat{c}_{2\downarrow}^{\dagger}(-\mathbf{k}), \hat{c}_{3\uparrow}^{\dagger}(-\mathbf{k}), \hat{c}_{3\downarrow}^{\dagger}(-\mathbf{k}) \right)^T. \quad (5.27)$$

Hence, the dimension of the BdG Hamiltonian is 12×12 . In Nambu representation, it can be

written as

$$\begin{aligned}\hat{\mathcal{H}}_{\mathbf{k}}^{\text{BdG}} &= \begin{pmatrix} \hat{h}_{\mathbf{k}} & \hat{\Delta} \\ \hat{\Delta}^\dagger & -\hat{h}_{-\mathbf{k}}^T \end{pmatrix} = \hat{h}_{\mathbf{k}} \frac{\mathbb{1}_\tau + \tau_z}{2} - \hat{h}_{-\mathbf{k}}^T \frac{\mathbb{1}_\tau - \tau_z}{2} + \tau_x \frac{\hat{\Delta} + \hat{\Delta}^\dagger}{2} + i\tau_y \frac{\hat{\Delta} - \hat{\Delta}^\dagger}{2} \\ &= \frac{\hat{h}_{\mathbf{k}} - \hat{h}_{-\mathbf{k}}^T}{2} \mathbb{1}_\tau + \frac{\hat{h}_{\mathbf{k}} + \hat{h}_{-\mathbf{k}}^T}{2} \tau_z + i(\tau_y \hat{\Delta}^{\text{Re}} + \tau_x \hat{\Delta}^{\text{Im}}),\end{aligned}\quad (5.28)$$

with $\hat{\Delta}$ and $\hat{h}_{\mathbf{k}}$ being 6×6 matrices corresponding to the order parameter and the non-interacting Hamiltonian in orbital and spin space. In the last line, we have used that the order parameter matrix fulfills $\hat{\Delta}^T = -\hat{\Delta}$.

The next step is to obtain the form of both matrices. First, we focus on the normal state Hamiltonian. Considering the two distinct contributions coming from the electronic dispersions and spin-orbit coupling, we can write it as

$$\hat{h}_{\mathbf{k}} = H_0(\mathbf{k}) + H_{\text{SOC}}. \quad (5.29)$$

On the one hand, we include the term for the dispersions and a small hybridization between the xz and yz orbitals, which as previously stated is the only one allowed by symmetry. Thus, the former term reads

$$H_0(\mathbf{k}) = \begin{pmatrix} \xi^{11}(\mathbf{k}) & g(\mathbf{k}) & 0 \\ g(\mathbf{k}) & \xi^{22}(\mathbf{k}) & 0 \\ 0 & 0 & \xi^{33}(\mathbf{k}) \end{pmatrix} \otimes \mathbb{1}_\sigma, \quad (5.30)$$

remembering that for the electronic dispersions it holds that

$$\begin{aligned}\xi^{11}(\mathbf{k}) &= -2t_1 \cos k_x - 2t_2 \cos k_y - \mu, \\ \xi^{22}(\mathbf{k}) &= -2t_2 \cos k_x - 2t_1 \cos k_y - \mu, \\ \xi^{33}(\mathbf{k}) &= -2t_3(\cos k_x + \cos k_y) - 4t_4 \cos k_x \cos k_y - 2t_5(\cos 2k_x + \cos 2k_y) - \mu,\end{aligned}\quad (5.31)$$

with $\{t_1, t_2, t_3, t_4, t_5\} = \{88, 9, 80, 40, 5\}$ meV, and $\mu = 109$ meV [44]. We consider a nearest-neighbor interorbital hybridization given by

$$g(\mathbf{k}) = -4t' \sin k_x \sin k_y, \quad (5.32)$$

with $t' = 4.4$ meV ($= 0.05t_1$) [45]. We notice that since the dispersions and the hybridization term are even under $\mathbf{k} \rightarrow -\mathbf{k}$, the normal state Hamiltonian fulfills $\hat{h}_{-\mathbf{k}} = \hat{h}_{\mathbf{k}}$. With the basis given by the Gell-Mann matrices, we can rewrite it as

$$\begin{aligned}H_0 &= \left[\frac{\xi^{11}(\mathbf{k}) + \xi^{22}(\mathbf{k}) + \xi^{33}(\mathbf{k})}{3} \mathbb{1}_\lambda + \frac{\xi^{11}(\mathbf{k}) - \xi^{22}(\mathbf{k})}{2} \lambda_3 \right. \\ &\quad \left. + \frac{\xi^{11}(\mathbf{k}) + \xi^{22}(\mathbf{k}) - 2\xi^{33}(\mathbf{k})}{2\sqrt{3}} \lambda_8 + g(\mathbf{k}) \lambda_1 \right] \otimes \mathbb{1}_\sigma.\end{aligned}\quad (5.33)$$

On the other hand, for the spin-orbit coupling Hamiltonian, $H_{\text{SOC}} = \lambda_{\text{SOC}} \sum_i \mathbf{L}_i \cdot \mathbf{S}_i$, restricting to the three t_{2g} -orbitals and taking the same form as in [9], we obtain the form in equation (3.4), which we rewrite here for convenience:

$$H_{\text{SOC}} = \frac{\lambda_{\text{SOC}}}{2} \begin{pmatrix} 0 & 0 & -i & 0 & 0 & i \\ 0 & 0 & 0 & i & i & 0 \\ i & 0 & 0 & 0 & 0 & -1 \\ 0 & -i & 0 & 0 & 1 & 0 \\ 0 & -i & 0 & 1 & 0 & 0 \\ -i & 0 & -1 & 0 & 0 & 0 \end{pmatrix}, \quad (5.34)$$

remembering that we are using the basis $\{d_{xz} \uparrow, d_{xz} \downarrow, d_{yz} \uparrow, d_{yz} \downarrow, d_{xy} \uparrow, d_{xy} \downarrow\}$. With the Gell-Mann and Pauli matrices, the previous Hamiltonian finally reads

$$H_{\text{SOC}} = \frac{\lambda_{\text{SOC}}}{2} (\lambda_2 \sigma_z - \lambda_5 \sigma_x + \lambda_7 \sigma_y), \quad (5.35)$$

which is also in agreement with Ref. [31, 50].

Secondly, recalling that we have the symmetry $[\Delta]_{\nu\sigma'}^{\mu\sigma} = -[\Delta]_{\mu\sigma}^{\nu\sigma'}$ for the order parameter components in terms of orbital and spin, the 6×6 matrix can be generally written as

$$\hat{\Delta} = \begin{pmatrix} 0 & [\Delta]_{1\downarrow}^{1\uparrow} & [\Delta]_{2\uparrow}^{1\uparrow} & [\Delta]_{2\downarrow}^{1\uparrow} & [\Delta]_{3\uparrow}^{1\uparrow} & [\Delta]_{3\downarrow}^{1\uparrow} \\ -[\Delta]_{1\downarrow}^{1\uparrow} & 0 & [\Delta]_{2\uparrow}^{1\downarrow} & [\Delta]_{2\downarrow}^{1\downarrow} & [\Delta]_{3\uparrow}^{1\downarrow} & [\Delta]_{3\downarrow}^{1\downarrow} \\ -[\Delta]_{2\uparrow}^{1\uparrow} & -[\Delta]_{2\uparrow}^{1\downarrow} & 0 & [\Delta]_{2\downarrow}^{2\uparrow} & [\Delta]_{3\uparrow}^{2\uparrow} & [\Delta]_{3\downarrow}^{2\uparrow} \\ -[\Delta]_{2\downarrow}^{1\uparrow} & -[\Delta]_{2\downarrow}^{1\downarrow} & -[\Delta]_{2\downarrow}^{2\uparrow} & 0 & [\Delta]_{3\uparrow}^{2\downarrow} & [\Delta]_{3\downarrow}^{2\downarrow} \\ -[\Delta]_{3\uparrow}^{1\uparrow} & -[\Delta]_{3\uparrow}^{1\downarrow} & -[\Delta]_{3\uparrow}^{2\uparrow} & -[\Delta]_{3\uparrow}^{2\downarrow} & 0 & [\Delta]_{3\downarrow}^{3\uparrow} \\ -[\Delta]_{3\downarrow}^{1\uparrow} & -[\Delta]_{3\downarrow}^{1\downarrow} & -[\Delta]_{3\downarrow}^{2\uparrow} & -[\Delta]_{3\downarrow}^{2\downarrow} & -[\Delta]_{3\downarrow}^{3\uparrow} & 0 \end{pmatrix}, \quad (5.36)$$

so that there are 15 independent components. Since the tensorial product of matrices does not commute, we have to be very careful. Thus, recalling our basis, we can consider first the 3×3 matrix corresponding to orbital space, and at each component we will have a 2×2 matrix corresponding to spin space.

Using that, as in the two-band model, $\{\mathbb{1}_\sigma, \sigma_x, \sigma_y, \sigma_z\}$ form a basis for the 2×2 matrices, we can write all components in terms of these basis elements, as detailed in Appendix B. Therefore, together with the representation of each element of a 3×3 matrix in terms of the Gell-Mann matrices, we can rewrite the superconducting order parameter matrix, with the purpose of using the notation

$$\hat{\Delta} = i(\hat{\psi} + \hat{\mathbf{d}} \cdot \boldsymbol{\sigma})\sigma_y, \quad (5.37)$$

allowing us to distinguish the spin-singlet and spin-triplet contributions. After rewriting the

matrix in the previous form, we obtain the 2 contributions

$$\begin{aligned}\hat{\psi} = & \mathbf{1}_\lambda \frac{1}{3}([\Delta]_{1\downarrow}^{1\uparrow} + [\Delta]_{2\downarrow}^{2\uparrow} + [\Delta]_{3\downarrow}^{3\uparrow})\mathbf{1}_\sigma + \lambda_3 \frac{1}{2}([\Delta]_{1\downarrow}^{1\uparrow} - [\Delta]_{2\downarrow}^{2\uparrow})\mathbf{1}_\sigma + \lambda_6 \frac{1}{2}([\Delta]_{3\downarrow}^{2\uparrow} + [\Delta]_{3\downarrow}^{2\uparrow})\mathbf{1}_\sigma \\ & + \lambda_1 \frac{1}{2}([\Delta]_{2\downarrow}^{1\uparrow} + [\Delta]_{2\downarrow}^{1\downarrow})\mathbf{1}_\sigma + \lambda_4 \frac{1}{2}([\Delta]_{3\downarrow}^{1\uparrow} + [\Delta]_{3\downarrow}^{1\downarrow})\mathbf{1}_\sigma + \lambda_8 \frac{1}{2\sqrt{3}}([\Delta]_{1\downarrow}^{1\uparrow} + [\Delta]_{2\downarrow}^{2\uparrow} - 2[\Delta]_{3\downarrow}^{3\uparrow})\mathbf{1}_\sigma,\end{aligned}\tag{5.38}$$

$$\begin{aligned}\hat{\mathbf{d}} \cdot \boldsymbol{\sigma} = & \lambda_2 \frac{1}{2}([\Delta]_{2\downarrow}^{1\uparrow} + [\Delta]_{2\downarrow}^{1\downarrow})\sigma_y + \lambda_2 \frac{-i}{2}([\Delta]_{2\downarrow}^{1\uparrow} - [\Delta]_{2\downarrow}^{1\downarrow})\sigma_x + \lambda_2 \frac{i}{2}([\Delta]_{2\downarrow}^{1\uparrow} + [\Delta]_{2\downarrow}^{1\downarrow}) \\ & + \lambda_5 \frac{1}{2}([\Delta]_{3\downarrow}^{1\uparrow} + [\Delta]_{3\downarrow}^{1\downarrow})\sigma_y + \lambda_5 \frac{-i}{2}([\Delta]_{3\downarrow}^{1\uparrow} - [\Delta]_{3\downarrow}^{1\downarrow})\sigma_x + \lambda_5 \frac{i}{2}([\Delta]_{3\downarrow}^{1\uparrow} + [\Delta]_{3\downarrow}^{1\downarrow})\sigma_z \\ & + \lambda_7 \frac{1}{2}([\Delta]_{3\downarrow}^{2\uparrow} + [\Delta]_{3\downarrow}^{2\downarrow})\sigma_y + \lambda_7 \frac{-i}{2}([\Delta]_{3\downarrow}^{2\uparrow} - [\Delta]_{3\downarrow}^{2\downarrow})\sigma_x + \lambda_7 \frac{i}{2}([\Delta]_{3\downarrow}^{2\uparrow} + [\Delta]_{3\downarrow}^{2\downarrow})\sigma_z.\end{aligned}\tag{5.39}$$

These results are summarized in Table 5.1, where we see how each term couples to band and spin space and whether it corresponds to spin triplet or singlet.

Table 5.1: Order parameter components entering in the spin-triplet ($\hat{\psi}$) and spin-singlet ($\hat{\mathbf{d}} \cdot \boldsymbol{\sigma}$) contributions, according to equations (5.38),(5.39). It is also included how they couple to band and spin space and the corresponding irreducible representation (IR).

$\hat{\Delta}$	Enters in	Orbital Space	λ	Spin space	$\boldsymbol{\sigma}$	IR
$\frac{1}{3}([\Delta]_{1\downarrow}^{1\uparrow} + [\Delta]_{2\downarrow}^{2\uparrow} + [\Delta]_{3\downarrow}^{3\uparrow})$	$\hat{\psi}$	Triplet	$\mathbf{1}_\lambda$	Singlet	$\mathbf{1}_\sigma$	A_{1g} (1)
$\frac{1}{2}([\Delta]_{2\downarrow}^{1\uparrow} - [\Delta]_{2\downarrow}^{1\downarrow})$	$\hat{\psi}$	Triplet	λ_1	Singlet	$\mathbf{1}_\sigma$	B_{2g} (1)
$\frac{1}{2}([\Delta]_{1\downarrow}^{1\uparrow} - [\Delta]_{2\downarrow}^{2\uparrow})$	$\hat{\psi}$	Triplet	λ_3	Singlet	$\mathbf{1}_\sigma$	B_{1g} (1)
$\frac{1}{2}([\Delta]_{3\downarrow}^{1\uparrow} - [\Delta]_{3\downarrow}^{1\downarrow})$	$\hat{\psi}$	Triplet	λ_4	Singlet	$\mathbf{1}_\sigma$	E_{yg} (1)
$\frac{1}{2}([\Delta]_{3\downarrow}^{2\uparrow} - [\Delta]_{3\downarrow}^{2\downarrow})$	$\hat{\psi}$	Triplet	λ_6	Singlet	$\mathbf{1}_\sigma$	E_{xg} (1)
$\frac{1}{2\sqrt{3}}([\Delta]_{1\downarrow}^{1\uparrow} + [\Delta]_{2\downarrow}^{2\uparrow} - 2[\Delta]_{3\downarrow}^{3\uparrow})$	$\hat{\psi}$	Triplet	λ_8	Singlet	$\mathbf{1}_\sigma$	A_{1g} (2)
$\frac{1}{2}([\Delta]_{2\downarrow}^{1\uparrow} + [\Delta]_{2\downarrow}^{1\downarrow})$	\hat{d}_y	Singlet	λ_2	Triplet	σ_y	E_{yg} (2)
$\frac{i}{2}([\Delta]_{2\downarrow}^{1\uparrow} + [\Delta]_{2\downarrow}^{1\downarrow})$	\hat{d}_z	Singlet	λ_2	Triplet	σ_z	A_{1g} (3)
$\frac{-i}{2}([\Delta]_{2\downarrow}^{1\uparrow} - [\Delta]_{2\downarrow}^{1\downarrow})$	\hat{d}_x	Singlet	λ_2	Triplet	σ_x	E_{xg} (2)
$\frac{1}{2}([\Delta]_{3\downarrow}^{1\uparrow} + [\Delta]_{3\downarrow}^{1\downarrow})$	\hat{d}_y	Singlet	λ_5	Triplet	σ_y	Reducible
$\frac{i}{2}([\Delta]_{3\downarrow}^{1\uparrow} + [\Delta]_{3\downarrow}^{1\downarrow})$	\hat{d}_z	Singlet	λ_5	Triplet	σ_z	E_{yg} (3)
$\frac{-i}{2}([\Delta]_{3\downarrow}^{1\uparrow} - [\Delta]_{3\downarrow}^{1\downarrow})$	\hat{d}_x	Singlet	λ_5	Triplet	σ_x	Reducible
$\frac{1}{2}([\Delta]_{3\downarrow}^{2\uparrow} + [\Delta]_{3\downarrow}^{2\downarrow})$	\hat{d}_y	Singlet	λ_7	Triplet	σ_y	Reducible
$\frac{i}{2}([\Delta]_{3\downarrow}^{2\uparrow} + [\Delta]_{3\downarrow}^{2\downarrow})$	\hat{d}_z	Singlet	λ_7	Triplet	σ_z	E_{xg} (3)
$\frac{-i}{2}([\Delta]_{3\downarrow}^{2\uparrow} - [\Delta]_{3\downarrow}^{2\downarrow})$	\hat{d}_x	Singlet	λ_7	Triplet	σ_x	Reducible

Therefore, in momentum space the Hamiltonian is 12×12 , so that for each eigenenergy E_n the returned eigenvector is of the form

$$(u_{1\uparrow}^n, u_{1\downarrow}^n, u_{2\uparrow}^n, u_{2\downarrow}^n, u_{3\uparrow}^n, u_{3\downarrow}^n, v_{1\uparrow}^n, v_{1\downarrow}^n, v_{2\uparrow}^n, v_{2\downarrow}^n, v_{3\uparrow}^n, v_{3\downarrow}^n)^T. \quad (5.40)$$

Similarly, in the real space code the Hamiltonian is $12N^2 \times 12N^2$, and therefore in each of the previous elements we need to include the subspace corresponding to all lattice sites.

Moreover, to be able to solve the Hamiltonian in real space we need to Fourier transform the electronic dispersions and the hybridization term in the real space lattice. As illustrated in Figure 5.3, in real space $\xi^{11}(\mathbf{k})$ and $\xi^{22}(\mathbf{k})$ correspond to a nearest neighbor hopping, whereas $g(\mathbf{k})$ includes a next-nearest neighbor interaction, and $\xi^{33}(\mathbf{k})$ will involve up to third nearest neighbors.

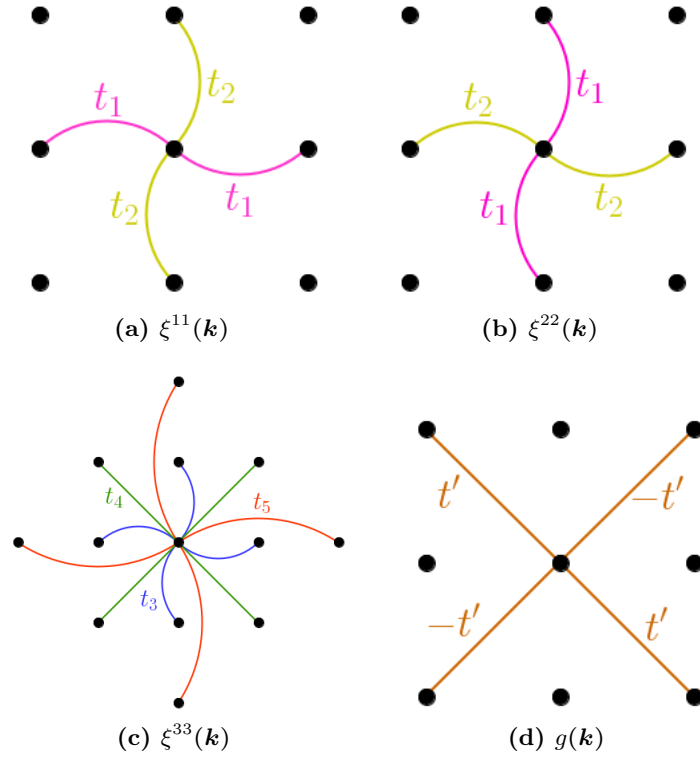


Figure 5.3: Fourier transformation of the momentum space electronic dispersions and hybridization term into the real space lattice neighbor hopping.

5.3.1 Point group symmetry for Sr_2RuO_4

In this section, we will give an overview of the basic ideas within group theory, focusing on the particular point group of Sr_2RuO_4 . For a detailed discussion, see Ref. [51]. This will become particularly important to study the order parameter, and will be essential in the second part of the thesis to incorporate longer range interactions.

First of all, it is important to understand the definition of a group, which consists on a set of elements $A, B, C, ..$ together with a product among these elements that fulfill the following four conditions:

1. The product of any two elements in the group is itself an element of the group;
2. The associative law holds, which means that it must satisfied $(AB)C = A(BC)$ for all group elements;
3. There exists an identity element E such that $AE = EA = A$, and therefore the product of E with any group element leaves that element invariant;
4. For every element A in the group, there exists an inverse element A^{-1} such that $AA^{-1} = A^{-1}A = E$.

Therefore, the elements of the group will in general not commute, $[A, B] \neq 0$. However, in the particular case where all elements commute, the group is called Abelian.

In particular, a point group exhibits a point that is left invariant under the application of all symmetry operations. Therefore, point groups have no translational symmetry, in contrast to space groups, which include both point group symmetry operations and translations. In particular, Sr_2RuO_4 has the tetragonal space group $I4/mmm$, where I refers to a body centered lattice [21]. This group consists of operations in the point group D_{4h} and intra-unit cell shifts by half a lattice parameter in all directions.

As will become important in the next section, we need to introduce the notation used for the point group symmetry operations. First of all, we denote E as the identity operation. Secondly, C_n represents a rotation around the z axis by $\frac{2\pi}{n}$. Differently, C'_n denotes a rotation around x/y axis, whereas C''_n around the $(-)x = y$ axis. Thirdly, $\sigma_h, \sigma_v, \sigma_d$ correspond to a reflection in a horizontal, vertical, and diagonal plane, respectively. In addition, the inversion is referred as \mathcal{I} and takes $\mathbf{r} \rightarrow -\mathbf{r}$ for all spatial coordinates. Finally, S_n corresponds to an improper rotation, which is composed of a rotation of $\frac{4\pi}{n}$ followed by an inversion.

It is also convenient to introduce the concept of a representation. If we consider an abstract group, a representation is the substitution group isomorphic to the first group, considering that two groups are isomorphic if there exists a one-to-one correspondence between their elements

such that

$$A \rightarrow a \tag{5.41}$$

$$B \rightarrow b \tag{5.42}$$

$$AB \rightarrow ab, \tag{5.43}$$

where the capital letters indicate the elements in one group and the lower letters the elements in the other group. Therefore, we can represent the symmetry operations of a group through a matrix representation such that $D(AB) = D(A)D(B)$.

Nevertheless, it must be noted that the representations $D(A)$ are not unique, since it could have been equally represented by performing a similarity transformation $UD(A)U^{-1}$. Additionally, we can generate another representation by combining them as

$$\begin{pmatrix} D(A) & \mathcal{O} \\ \mathcal{O} & D'(A) \end{pmatrix}, \tag{5.44}$$

where \mathcal{O} is a matrix of zeros and $D(A)$ and $D'(A)$ are different (or even the same) representations.

To overcome this issue, it is convenient to consider the irreducible representations (IRs), which cannot be expressed in terms of representations of lower dimensionality. Thus, they cannot be further block-diagonalized and reduced. We denote the matrix representation of the element A corresponding to the IR Γ_j as $D^{\Gamma_j}(A)$. Due to the arbitrariness of a representation, we also introduce the trace (or character) of a matrix representation for a symmetry operation R , $\chi^{\Gamma_j}(R) = \text{Tr}D^{\Gamma_j}(R)$, since it is invariant under a change of basis. This allows for the construction of the character tables for the different point groups.

We also introduce the ‘‘Wonderful Orthogonality Theorem’’ for characters, which states that the characters of an irreducible representation obey the orthogonality relation

$$\sum_R \chi^{\Gamma_j}(R)\chi^{\Gamma_i}(R^{-1}) = h\delta_{\Gamma_j, \Gamma_i}, \tag{5.45}$$

where h is the order of the group, referring to the number of elements in the group. This theorem has profound consequences, implying that non-equivalent irreducible representations are orthogonal [51].

In addition, we also need to introduce the concept of a class. In order to understand what the class is, first another definition must be presented. We consider an element B as the conjugate to A if they fulfill by definition $B \equiv XAX^{-1}$, where X is an arbitrary element of the group. With this in mind, we can get to the class, which is defined by all the elements that can be obtained from a given group element by conjugation. The information about the characters of the representations of a group is summarized in the character tables, where the IRs for a particular point group are listed in column form (usually in the left column), and the class is listed as rows (top row).

Considering all the previous definitions, we can focus now on the character table for the point group D_{4h} , detailed in Appendix C. This particular group has the 10 classes of operations

$$D_{4h} = \{E, 2C_4, C_2, 2C_2', 2C_2'', \mathcal{I}, 2S_4, \sigma_h, 2\sigma_v, 2\sigma_d\}, \quad (5.46)$$

resulting in 16 group symmetry elements. Due to the theorem stating that the number of IRs is equal to the number of classes, in this group we have 10 IRs, from which 8 are one-dimensional IRs ($A_{1g}, B_{1g}, A_{2g}, B_{2g}, A_{1u}, B_{1u}, A_{2u}, B_{2u}$), and only 2 are two-dimensional (E_g, E_u). The g and u indices denote if the IR is invariant under parity or not, respectively. The IR A_{1g} transforms trivially under all point group operations, whereas in the other cases some symmetries are broken, therefore belonging to a subgroup of D_{4h} (for more details on these classifications see Ref. [52]).

In addition, to see how the combination of the different elements in the group are related, we can construct a multiplication table recalling that, according to the first defining condition of a group, the product of two elements in a group will itself be an element of the group. As it will be necessary to know the product on the different elements in the particular point group D_{4h} , the multiplication table is also included in Appendix C.

Finally, since it will be important in the second part of the thesis, we also introduce the concept of basis functions, which can be used to generate the matrices that represent the symmetry elements of a particular IR or to project the different IRs of some arbitrary function. The most important ones are stated in the character tables (see Appendix C). If we denote the IRs by Γ_n , where n labels the representation, we can define a set of basis vectors given by $|\Gamma_n j\rangle$, where j labels the component of the representation (for a one-dimensional representation, $j = 1$, whereas for a two-dimensional one $j = 1, 2$). The basis vectors relate the symmetry operators \hat{P}_R with its matrix representation $D^{\Gamma_n}(R)$ as

$$\hat{P}_R |\Gamma_n i\rangle = \sum_j D^{\Gamma_n}(R)_{ji} |\Gamma_n j\rangle. \quad (5.47)$$

In the particular case where these basis vectors can be expressed explicitly in coordinate space, we define them as basis functions.

5.3.2 Irreducible representations of the superconducting order parameter

After having introduced the basic group theory definitions, in this section we proceed to study the irreducible representations of the superconducting order parameter, with the ultimate goal of classifying the combinations obtained in Table 5.1 into the different IR of the point group D_{4h} .

First of all, we notice that there are different ways of expressing the group elements, so that we are allowed to write our point group as the combination $D_{4h} = C_{4v} \otimes \{E, \mathcal{I}\}$. We can check that this is equivalent to considering $D_{4h} = D_4 \otimes \{E, \mathcal{I}\}$, so that both representations lead to the same group elements:

1. $D_4 \otimes \{E, \mathcal{I}\}$
 $D_4 \otimes E = \{E, 2C_4, C_2, 2C_2', 2C_2''\}$
 $D_4 \otimes \mathcal{I} = \{\mathcal{I}, 2S_4, \sigma_h, 2\sigma_v, 2\sigma_d\};$
2. $C_{4v} \otimes \{E, \mathcal{I}\}$
 $C_{4v} \otimes E = \{E, C_2, 2C_4, 2\sigma_v, 2\sigma_d\}$
 $C_{4v} \otimes \mathcal{I} = \{\mathcal{I}, 2S_4, \sigma_h, 2C_2', 2C_2''\}.$

To define the matrix representations, we need to consider the degrees of freedom corresponding to spin, orbital and Nambu space. For the latter, as detailed in Appendix D, the notation $\hat{\Delta} = i(\hat{\psi} + \hat{\mathbf{d}} \cdot \boldsymbol{\sigma})\sigma_y$ becomes very convenient when considering the point group analysis, since the Nambu matrices $\boldsymbol{\tau}$ are left in the trivial A_{1g} representation. Consequently, to identify the different irreducible representations we only need to focus on orbital and spin space. Due to spin-orbit coupling, we need to represent each element in band and spin space. For the first one, to describe the 3 bands we can use as generators the Gell-Mann matrices together with the identity in 3×3 space. For the second one, remembering that spin forms a 2×2 space, we can choose as generators the Pauli matrices with the 2×2 identity, $\{\mathbb{1}_\sigma, \boldsymbol{\sigma}\}$.

Since we choose to decompose the point group as $D_{4h} = C_{4v} \otimes \{E, \mathcal{I}\}$, and the matrix representation of the inversion will turn out to be trivial, corresponding to the identity matrix, we only need to focus on the matrix representation of the elements of C_{4v} . With this purpose, we need to remember that the symmetry operations transform the space coordinates as

$$\begin{aligned}
E(x, y, z) &= E(x, y, z), & C_4(x, y, z) &= (y, -x, z), \\
\mathcal{I}(x, y, z) &= (-x, -y, -z), & \sigma_{xz}(x, y, z) &= (x, -y, z), \\
C_2(x, y, z) &= (-x, -y, z), & \sigma_{x=y}(x, y, z) &= (y, x, z),
\end{aligned} \tag{5.48}$$

where σ_{xz} is the reflection in plane in the xz axis, and $\sigma_{x=y}$ is the reflection in the diagonal plane $x = y$.

First, we can start with orbital space, by choosing the basis $\{xz, yz, xy\}$. Therefore, by using the previous transformations we can calculate how the different point group operations act in this basis, obtaining the following matrix representations:

$$\begin{aligned}
d_\lambda(E) &= \mathbb{1}_\lambda, & d_\lambda(\mathcal{I}) &= \mathbb{1}_\lambda, & d_\lambda(C_2) &= \begin{pmatrix} -1 & 0 & 0 \\ 0 & -1 & 0 \\ 0 & 0 & 1 \end{pmatrix}, \\
d_\lambda(C_4) &= \begin{pmatrix} 0 & -1 & 0 \\ 1 & 0 & 0 \\ 0 & 0 & -1 \end{pmatrix}, & d_\lambda(\sigma_{xz}) &= \begin{pmatrix} 1 & 0 & 0 \\ 0 & -1 & 0 \\ 0 & 0 & -1 \end{pmatrix}, & d_\lambda(\sigma_{x=y}) &= \begin{pmatrix} 0 & 1 & 0 \\ 1 & 0 & 0 \\ 0 & 0 & 1 \end{pmatrix}.
\end{aligned} \tag{5.49}$$

Focusing next on spin space, we recall that the generator of rotations in this case corresponds to

$$d_\sigma(C_n) = e^{-i\mathbf{S} \cdot \boldsymbol{\varphi}} = e^{-i\boldsymbol{\sigma} \cdot \frac{\boldsymbol{\varphi}}{2}}, \tag{5.50}$$

where we have taken $\mathbf{S} = \frac{\sigma}{2}$, with $\hbar \equiv 1$, and φ denotes the angle of the rotation.

To see how inversion acts on the spin operator we need to remember how space and momentum coordinates transform under this operation,

$$\mathcal{I}\mathbf{x}\mathcal{I}^\dagger = -\mathbf{x}, \quad \mathcal{I}\mathbf{p}\mathcal{I}^\dagger = -\mathbf{p}. \quad (5.51)$$

Thus, the angular momentum operator $\mathbf{L} = \mathbf{x} \times \mathbf{p}$ will not change sign under parity. Since the total angular momentum also does not change sign, we can see that the same must occur for the spin operator [53]. Hence, in matrix representation this would correspond to an identity in spin space.

The following step is to determine the representation of the reflections in spin space. In this case, we can use that \mathbf{S} transforms as the orbital angular momentum $\mathbf{L} = \mathbf{x} \times \mathbf{p}$. Recalling how the coordinates transform under the reflections, since the momentum is given by $p_i = \frac{\partial}{\partial x_i}$, it will transform in the same way. Using these results, we can see how \mathbf{L} transforms under the operations, leading to

$$\sigma_{xz}(L_x, L_y, L_z) = (-L_x, L_y, -L_z), \quad (5.52)$$

$$\sigma_{x=y}(L_x, L_y, L_z) = -(L_y, L_x, L_z). \quad (5.53)$$

Hence, the spin will transform in the same way under these reflections. By inspection, using that $\mathbf{S} = \frac{\sigma}{2}$, we can find the matrix representation that corresponds to the previous operations, corresponding to σ_y for the vertical plane reflection and $\frac{\sigma_y - \sigma_x}{\sqrt{2}}$ for the diagonal one.

Nevertheless, another important condition enters in the previous matrix representation, since we must remember that fermions belong to the double group. To understand this, we can recall that when we consider a spin- $\frac{1}{2}$ system, to recover the initial state we need to apply a 4π rotation instead of a 2π , which would return a minus sign. Thus, as reflections should act in the same way we must add a phase $\pm i$ in front of the matrix representation.

Finally, from the previous results we can write the matrices representing each transformation in spin space, corresponding to

$$\begin{aligned} d_\sigma(E) &= \mathbb{1}_\sigma, & d_\sigma(\mathcal{I}) &= \mathbb{1}_\sigma, & d_\sigma(C_2) &= -i\sigma_z, \\ d_\sigma(C_4) &= \frac{\mathbb{1}_\sigma - i\sigma_z}{\sqrt{2}}, & d_\sigma(\sigma_v) &= -i\sigma_y, & d_\sigma(\sigma_d) &= -i\frac{\sigma_y - \sigma_x}{\sqrt{2}}. \end{aligned} \quad (5.54)$$

Once we have the matrices, we can see how the band and the spin generators transform under each point group element $g \in D_{4h}$. With this purpose, we need to calculate

$$\begin{aligned} d_\lambda^\dagger(g)\lambda_i d_\lambda(g), \\ d_\sigma^\dagger(g)\sigma_i d_\sigma(g), \end{aligned} \quad (5.55)$$

for each $\lambda_i = \{\mathbb{1}_\lambda, \boldsymbol{\lambda}\}$ and $\sigma_i = \{\mathbb{1}_\sigma, \boldsymbol{\sigma}\}$ in orbital and spin space, respectively. Once we know how each element transforms under all point group operations, we can look at the character table

for the group D_{4h} shown in Appendix C, and we can identify the corresponding IR for each generator. Since in our case we have seen that the inversion corresponds to the identity matrix, we only need to focus on the even IR. These results are summarized in Tables 5.2, 5.3, for the band and the spin generators, respectively.

Looking back at Table 5.1, we can see how each combination of the order parameter components couples to band and spin space. Therefore, we can identify the IR in each channel by looking at the product table for the different IR of the point group, shown in Appendix C. For instance, we can take the combination $\frac{1}{3}([\Delta]_{1\downarrow}^{1\uparrow} + [\Delta]_{2\downarrow}^{2\uparrow} + [\Delta]_{3\downarrow}^{3\uparrow})$, which couples in band space to $\mathbb{1}_\lambda$ and in spin space to $\mathbb{1}_\sigma$. From Tables 5.2, 5.3, we can see that the IR will correspond to $A_{1g} \otimes A_{1g} = A_{1g}$. We can take another example, the combination $\frac{1}{2}([\Delta]_{1\downarrow}^{1\uparrow} - [\Delta]_{2\downarrow}^{2\uparrow})$, which couples in band space to λ_1 and in spin space to $\mathbb{1}_\sigma$. Hence, the IR is now $B_{2g} \otimes A_{1g} = B_{2g}$. All the corresponding IRs are detailed in the last column in the Table 5.1.

Table 5.2: Irreducible representations for the band generators $\{\mathbb{1}_\lambda, \lambda\}$.

Band generators	E	C ₂	2C ₄	2σ _v	2σ _d	\mathcal{I}	IR
$\mathbb{1}_\lambda, \lambda_8$	1	1	1	1	1	1	A_{1g}
λ_2	1	1	1	-1	-1	1	A_{2g}
λ_3	1	1	-1	1	-1	1	B_{1g}
λ_1	1	1	-1	-1	1	1	B_{2g}
$(\lambda_6, \lambda_4), (\lambda_7, \lambda_5)$	2	-2	0	0	0	2	E_g

Table 5.3: Irreducible representations for the spin generators $\{\mathbb{1}_\sigma, \sigma\}$.

Spin generators	E	C ₂	2C ₄	2σ _v	2σ _d	\mathcal{I}	IR
$\mathbb{1}_\sigma$	1	1	1	1	1	1	A_{1g}
σ_z	1	1	1	-1	-1	1	A_{2g}
(σ_x, σ_y)	2	-2	0	0	0	2	E_g

Nevertheless, in some cases we find that the total IR corresponds to $E_g \otimes E_g$. Thus, since the resulting representation has a dimensionality larger than two, it would be reducible. Considering that we aim to classify all possible solutions in terms of IRs, we notice that by taking particular combinations of the previous reducible representations they behave then as a particular IR of the point group D_{4h} . In order to understand this, we consider a particular example. If we consider the first and the last reducible representations in Table 5.1, we can take the Gell-Mann and Pauli matrices combination $\lambda_5\sigma_y + \lambda_7\sigma_x$. Using the matrix representation in orbital and spin basis for the different operations of our point group, we can calculate how each of these matrices transforms under all operations by using equation (5.55). Therefore, we see that the previous combination will transform as the A_{2g} IR. In the same way, we can study the other three possible combinations. All results obtained are presented in Table 5.4.

In Figure 5.4, the different superconducting order parameter irreducible representations as a function of the temperature are shown, obtained from the homogeneous momentum space self-consistency solution. In the on-site interactions case, we can see that the leading and subleading IRs are A_{1g} . Moreover, from Table 5.1 we see that although we are including spin-orbit coupling in this effective model, the leading superconducting symmetries are of spin-singlet character, and therefore correspond to orbital triplet. For the particular strength chosen there also appears a B_{2g} channel, with a corresponding spin triplet (see Table 5.4).

Table 5.4: Irreducible representations coupling to an even form factor obtained by combining the four reducible representations in Table 5.1.

$\hat{\Delta}$	Combined spin and orbital	Orbital	Spin	IR
$\frac{1}{4}([\Delta]_{3\uparrow}^{1\uparrow} + [\Delta]_{3\downarrow}^{1\downarrow} - i([\Delta]_{3\uparrow}^{2\uparrow} - [\Delta]_{3\downarrow}^{2\downarrow}))$	$\lambda_5\sigma_y + \lambda_7\sigma_x$	Singlet	Triplet	A_{2g} (1)
$\frac{1}{4}([\Delta]_{3\uparrow}^{1\uparrow} + [\Delta]_{3\downarrow}^{1\downarrow} + i([\Delta]_{3\uparrow}^{2\uparrow} - [\Delta]_{3\downarrow}^{2\downarrow}))$	$\lambda_5\sigma_y - \lambda_7\sigma_x$	Singlet	Triplet	B_{2g} (2)
$\frac{1}{4}(-i([\Delta]_{3\uparrow}^{1\uparrow} - [\Delta]_{3\downarrow}^{1\downarrow}) + [\Delta]_{3\uparrow}^{2\uparrow} + [\Delta]_{3\downarrow}^{2\downarrow})$	$\lambda_5\sigma_x + \lambda_7\sigma_y$	Singlet	Triplet	B_{1g} (2)
$\frac{1}{4}(-i([\Delta]_{3\uparrow}^{1\uparrow} - [\Delta]_{3\downarrow}^{1\downarrow}) - [\Delta]_{3\uparrow}^{2\uparrow} - [\Delta]_{3\downarrow}^{2\downarrow})$	$\lambda_5\sigma_x - \lambda_7\sigma_y$	Singlet	Triplet	A_{1g} (4)

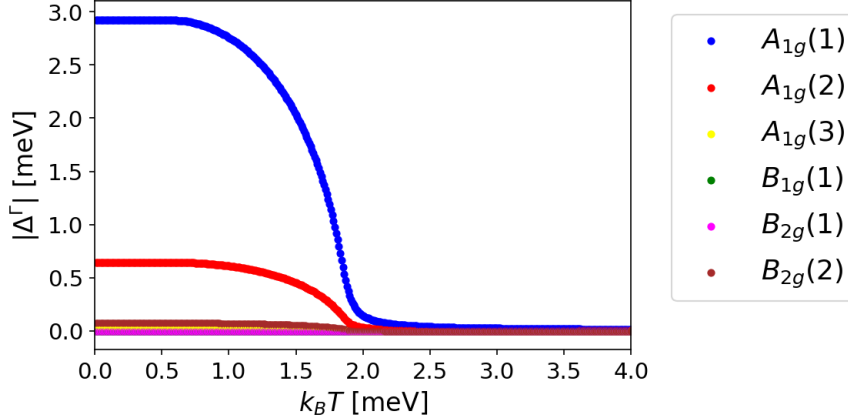


Figure 5.4: Leading superconducting order parameter channels corresponding to the irreducible representations indicated in Table 5.1. The parameters chosen are $N = 21$, $\{t_1, t_2, t_3, t_4, t_5, t'\} = \{88, 9, 80, 40, 5, 0\}$ meV, $\lambda_{\text{SOC}} = 35$ meV, a fixed $\mu = 109$ meV, and for the interaction strengths $U = -25$ meV, $J = U/4$, $J' = J$, $U' = U - 2J$.

Similar to the one-band and the two-band models, we can plot the real space order parameter components with an impurity in the center lattice site for a fixed temperature, as can be seen in Figure 5.5. Only the order parameter components with the same orbital but opposite spin are plotted, since they have the largest contributions. We notice that for the xz and yz orbitals (Figures 5.5a and 5.5b, respectively), the effect of the impurity in the real space lattice is the same but rotated by $\pi/2$. Differently, the xy orbital (Figure 5.5c) displays a symmetric effect due to the impurity in the x and y direction, corresponding to the different lattice sites. In addition, we see that for the xy orbital the order parameter is larger, since this orbital is closer to a region with a higher density of states.

We can also plot the normalized order parameter IRs, $|\Delta_{\mathbf{R}}^{\Gamma}|/|\Delta^{\Gamma}|$, where $|\Delta^{\Gamma}|$ is obtained from the homogeneous momentum space code. These results can be observed in Figure 5.6, with an impurity in the center site. In comparison with the previous one-band and two-band models, we see that now the impurity has an effect even in lattice sites further away from the defect for all IRs plotted. Finally, we see that the effect of the impurity in the real space lattice is different in all cases, even if we consider the same IRs.

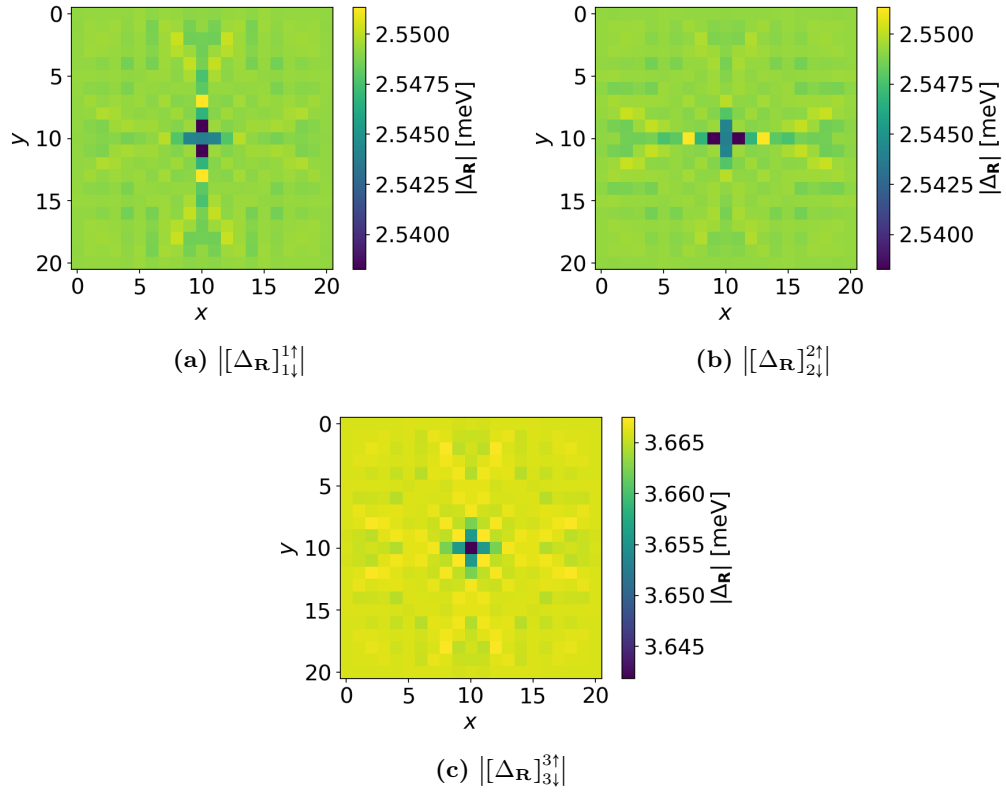


Figure 5.5: Real space superconducting order parameter $|\Delta_{\mathbf{R}}|$ in a three-band model with a non-magnetic impurity at the center of the three orbitals. We consider a 21×21 square lattice, with $\{t_1, t_2, t_3, t_4, t_5, t'\} = \{88, 9, 80, 40, 5, 0\}$ meV, $\lambda_{\text{SOC}} = 35$ meV, a fixed $\mu = 109$ meV, $V_{\text{imp}} = 1$ meV, and for the interaction strengths $U = -25$ meV, $J = U/4$, $J_1 = J$, $U_1 = U - 2J$. The particular orbital and spin components plotted are detailed in each caption.

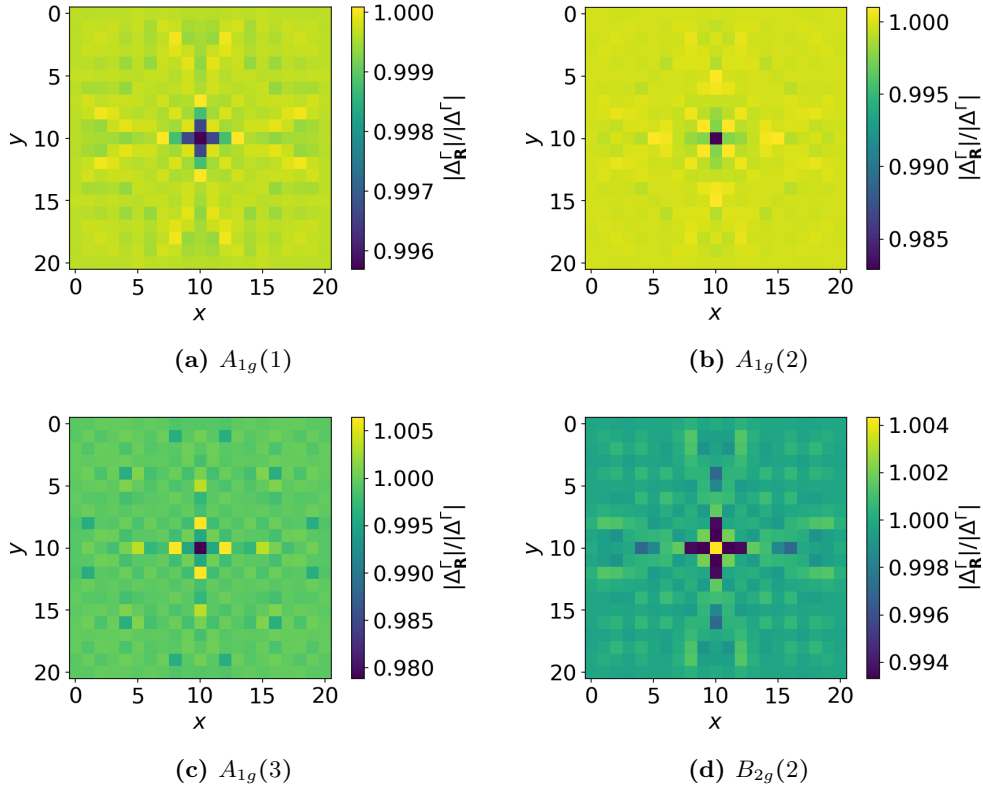


Figure 5.6: Real space superconducting order parameter irreducible representations $|\Delta_{\mathbf{R}}^{\Gamma}|$, according to Tables 5.1, 5.4, in a three-band model with a non-magnetic impurity at the center of the three orbitals, normalized with respect to the homogeneous value $|\Delta^{\Gamma}|$. We consider a 21×21 square lattice, with $\{t_1, t_2, t_3, t_4, t_5, t'\} = \{88, 9, 80, 40, 5, 0\}$ meV, $\lambda_{\text{SOC}} = 35$ meV, a fixed $\mu = 109$ meV, $V_{\text{imp}} = 1$ meV, and for the interaction strengths $U = -25$ meV, $J = U/4$, $J_1 = J$, $U_1 = U - 2J$. The particular IR plotted is detailed in each caption.

Chapter 6

Systems with off-site interactions

In this chapter, we consider a more general interaction potential including different neighbors. Only the results for the simple one-band model in momentum space are shown, since in the case of a more complicated system it is challenging to find a toy model that fulfills all the symmetries for the pairing interaction due to fermionic statistics, presented in equation (4.23). As we will see, the pairing strengths originated from a spin-fluctuation mechanism will fulfill those symmetries by construction.

In addition, a new way of solving self-consistently for the order parameter is introduced, based on the decomposition into the basis functions of the point group. This new formulation of the problem will be highly advantageous in the next Chapter. Not only does it reduce the computation time, but it also allows to characterize the symmetry of the solution according to a point group theory analysis.

To begin with, we include only nearest neighbor interactions, which lead to the following form for the interaction strength:

$$[V_{\mathbf{R}-\mathbf{R}'}]_{\tilde{\mu}_j, \tilde{\mu}_l}^{\tilde{\mu}_i, \tilde{\mu}_k} = \sum_{\boldsymbol{\delta}} [U]_{\tilde{\mu}_j, \tilde{\mu}_l}^{\tilde{\mu}_i, \tilde{\mu}_k} \delta_{\mathbf{R}-\mathbf{R}', \boldsymbol{\delta}}, \quad \text{with} \quad \boldsymbol{\delta} = \pm\{\hat{x}, \hat{y}\}, \quad (6.1)$$

denoting the nearest neighbors for each lattice point. In this case, the wave-vector representation corresponds to

$$\begin{aligned} [V_{\mathbf{k}-\mathbf{k}'}]_{\tilde{\mu}_j, \tilde{\mu}_l}^{\tilde{\mu}_i, \tilde{\mu}_k} &= \sum_{\mathbf{R}, \mathbf{R}'} [V_{\mathbf{R}-\mathbf{R}'}]_{\tilde{\mu}_j, \tilde{\mu}_l}^{\tilde{\mu}_i, \tilde{\mu}_k} e^{-i(\mathbf{R}-\mathbf{R}') \cdot (\mathbf{k}-\mathbf{k}')} \\ &= \sum_{\boldsymbol{\delta}} [U]_{\tilde{\mu}_j, \tilde{\mu}_l}^{\tilde{\mu}_i, \tilde{\mu}_k} e^{-i\boldsymbol{\delta} \cdot (\mathbf{k}-\mathbf{k}')} \\ &= 2[U]_{\tilde{\mu}_j, \tilde{\mu}_l}^{\tilde{\mu}_i, \tilde{\mu}_k} [\cos(k_x - k'_x) + \cos(k_y - k'_y)], \end{aligned} \quad (6.2)$$

remembering that we are assuming the interaction potential to be translational invariant.

Recalling equation (4.21), since the superconducting order parameter depends on $[V_{\mathbf{k}-\mathbf{k}'}]_{\tilde{\mu}_j, \tilde{\mu}_l}^{\tilde{\mu}_i, \tilde{\mu}_k}$, we should perform the sum over \mathbf{k}' for each value of \mathbf{k} , which would result in a large computation time when solving self-consistently. To avoid this, we can use the fact that

the interaction potential can be decomposed into the dependence on \mathbf{k} and \mathbf{k}' . The functions obtained correspond to the basis functions of the system point group, since they transform as one of the IR stated in Appendix C under all group operations. Therefore, we can rewrite the expression above as

$$[V_{\mathbf{k}-\mathbf{k}'}]_{\tilde{\mu}_j, \tilde{\mu}_l}^{\tilde{\mu}_i, \tilde{\mu}_k} = [U]_{\tilde{\mu}_j, \tilde{\mu}_l}^{\tilde{\mu}_i, \tilde{\mu}_k} \left(2 \sin k_x \sin k'_x + 2 \sin k_y \sin k'_y \right. \\ \left. + [\cos k_x + \cos k_y][\cos k'_x + \cos k'_y] + [\cos k_x - \cos k_y][\cos k'_x - \cos k'_y] \right). \quad (6.3)$$

For completeness, we also consider next-to nearest neighbor interactions, although the possibility of a decomposition in terms of the basis functions holds for all neighbors. In this case, the interaction potential is given by

$$[V_{\mathbf{R}-\mathbf{R}'}]_{\tilde{\mu}_j, \tilde{\mu}_l}^{\tilde{\mu}_i, \tilde{\mu}_k} = \sum_{\boldsymbol{\delta}} [U]_{\tilde{\mu}_j, \tilde{\mu}_l}^{\tilde{\mu}_i, \tilde{\mu}_k} \delta_{\mathbf{R}-\mathbf{R}', \boldsymbol{\delta}}, \quad \text{with} \quad \boldsymbol{\delta} = \pm\{\hat{x} + \hat{y}, \hat{x} - \hat{y}\}. \quad (6.4)$$

In the wave-vector representation, it corresponds to

$$[V_{\mathbf{k}-\mathbf{k}'}]_{\tilde{\mu}_j, \tilde{\mu}_l}^{\tilde{\mu}_i, \tilde{\mu}_k} = 2[U]_{\tilde{\mu}_j, \tilde{\mu}_l}^{\tilde{\mu}_i, \tilde{\mu}_k} \cos(k_x - k'_x) \cos(k_y - k'_y). \quad (6.5)$$

Using the same idea as in the previous case, with trigonometric identities we can rewrite it as

$$[V_{\mathbf{k}-\mathbf{k}'}]_{\tilde{\mu}_j, \tilde{\mu}_l}^{\tilde{\mu}_i, \tilde{\mu}_k} = [U]_{\tilde{\mu}_j, \tilde{\mu}_l}^{\tilde{\mu}_i, \tilde{\mu}_k} \left([2 \cos k_x \cos k_y][2 \cos k'_x \cos k'_y] + [2 \sin k_x \sin k_y][2 \sin k'_x \sin k'_y] \right. \\ \left. + [2 \cos k_x \sin k_y][2 \cos k'_x \sin k'_y] + [2 \sin k_x \cos k_y][2 \sin k'_x \cos k'_y] \right). \quad (6.6)$$

Hence, each term has two separate contributions, one depending on \mathbf{k} and the other on \mathbf{k}' .

Therefore, we can write a general expression for the interaction potential by projecting as

$$[V_{\mathbf{k}-\mathbf{k}'}]_{\tilde{\mu}_j, \tilde{\mu}_l}^{\tilde{\mu}_i, \tilde{\mu}_k} = \sum_{\Gamma \in \text{IR}} [V_{\mathbf{k}, \Gamma}]_{\tilde{\mu}_j, \tilde{\mu}_l}^{\tilde{\mu}_i, \tilde{\mu}_k} g_{\mathbf{k}}^{\Gamma}, \quad \text{with} \quad [V_{\mathbf{k}', \Gamma}]_{\tilde{\mu}_j, \tilde{\mu}_l}^{\tilde{\mu}_i, \tilde{\mu}_k} = \frac{1}{\mathcal{N}} \sum_{\mathbf{k}} (g_{\mathbf{k}}^{\Gamma})^* [V_{\mathbf{k}-\mathbf{k}'}]_{\tilde{\mu}_j, \tilde{\mu}_l}^{\tilde{\mu}_i, \tilde{\mu}_k}, \quad (6.7)$$

where $g_{\mathbf{k}}^{\Gamma}$ is a normalized basis function, or alternatively called form factor, of the Γ irreducible representation of the point group, fulfilling the orthogonality relation $\frac{1}{\mathcal{N}} \sum_{\mathbf{k}} (g_{\mathbf{k}}^{\Gamma})^* g_{\mathbf{k}}^{\Gamma'} = \delta_{\Gamma, \Gamma'}$ [51]. To identify the IR that each basis function corresponds to, we can see how they transform under all D_{4h} point group operations.

Replacing in equation (4.21) for the superconducting order parameter, we obtain

$$[\Delta_{\mathbf{k}}]_{\tilde{\mu}_j}^{\tilde{\mu}_i} = \sum_{\Gamma \in \text{IR}} g_{\mathbf{k}}^{\Gamma} \frac{1}{\mathcal{N}} \sum_{\mathbf{k}'} \sum_{\tilde{\mu}_k, \tilde{\mu}_l} [V_{\mathbf{k}', \Gamma}]_{\tilde{\mu}_j, \tilde{\mu}_l}^{\tilde{\mu}_i, \tilde{\mu}_k} \langle \hat{c}_{-\mathbf{k}' \tilde{\mu}_l} \hat{c}_{\mathbf{k}' \tilde{\mu}_k} \rangle \\ = \sum_{\Gamma \in \text{IR}} g_{\mathbf{k}}^{\Gamma} \left[-\frac{1}{\mathcal{N}} \sum_{\mathbf{k}'} \sum_{\tilde{\mu}_k, \tilde{\mu}_l} [V_{\mathbf{k}', \Gamma}]_{\tilde{\mu}_j, \tilde{\mu}_l}^{\tilde{\mu}_i, \tilde{\mu}_k} \sum_n u_{\mathbf{k}' \tilde{\mu}_k}^n v_{-\mathbf{k}' \tilde{\mu}_l}^{n*} \tanh\left(\frac{\beta E_{\mathbf{k}' n}}{2}\right) \right] \equiv \sum_{\Gamma \in \text{IR}} g_{\mathbf{k}}^{\Gamma} [\Delta_{\Gamma}]_{\tilde{\mu}_j}^{\tilde{\mu}_i}, \quad (6.8)$$

where in the last line we have introduced the Bogoliubov transformations, obtaining the same expression derived in equation (4.29). Moreover, from the expression above we can see that we have decoupled the wave-vector and spin/orbital degrees of freedom. This will be advantageous in the case of Sr_2RuO_4 in order to identify the preferred symmetry for the order parameter, as we will explain in the next Chapter.

6.1 One-band model

Similar to the case of on-site interactions, in the one-band model the interaction potential takes the simple form

$$[U]_{\bar{\sigma},\bar{\sigma}}^{\sigma,\sigma} = g, \quad [U]_{\bar{\sigma},\sigma}^{\sigma,\bar{\sigma}} = -g. \quad (6.9)$$

Differently, the order parameter would depend now on the position in \mathbf{k} -space and, thus, it is no longer constant. Therefore, the mean-field Hamiltonian in momentum space in equation (4.20) corresponds to

$$H = \sum_{\mathbf{k}} \sum_{\sigma} c_{\mathbf{k}\sigma}^{\dagger} \xi_{\mathbf{k}} c_{\mathbf{k}\sigma} + \frac{1}{\mathcal{N}} \sum_{\mathbf{k}} \left(c_{\mathbf{k}\uparrow}^{\dagger} [\Delta_{\mathbf{k}}]_{\downarrow}^{\uparrow} c_{-\mathbf{k}\downarrow}^{\dagger} + \text{h.c.} \right), \quad (6.10)$$

where we have used the symmetry $[\Delta_{\mathbf{k}}]_{\tilde{\mu}_j}^{\tilde{\mu}_i} = -[\Delta_{-\mathbf{k}}]_{\tilde{\mu}_i}^{\tilde{\mu}_j}$ for the order parameter derived in equation (4.25).

Considering only nearest neighbors and using the previous decomposition in terms of the point group form factors, the superconducting order parameter is given by

$$\begin{aligned} [\Delta_{\mathbf{k}}]_{\downarrow}^{\uparrow} &= \frac{1}{\mathcal{N}} \sum_{\mathbf{k}'} \sum_{\sigma} [V_{\mathbf{k}-\mathbf{k}'}]_{\downarrow,\bar{\sigma}}^{\uparrow,\sigma} \langle c_{-\mathbf{k}'\bar{\sigma}} c_{\mathbf{k}'\sigma} \rangle \\ &= \frac{2}{\mathcal{N}} \sum_{\mathbf{k}'} \sum_{\sigma} [U]_{\downarrow,\bar{\sigma}}^{\uparrow,\sigma} [\cos(k_x - k'_x) + \cos(k_y - k'_y)] \langle c_{-\mathbf{k}'\bar{\sigma}} c_{\mathbf{k}'\sigma} \rangle \\ &= (\cos k_x + \cos k_y) [\Delta_{A_{1g}}]_{\downarrow}^{\uparrow} + (\cos k_x - \cos k_y) [\Delta_{B_{1g}}]_{\downarrow}^{\uparrow} \\ &\quad + i\sqrt{2} \sin k_x [\Delta_{E_{xu}}]_{\downarrow}^{\uparrow} + i\sqrt{2} \sin k_y [\Delta_{E_{yu}}]_{\downarrow}^{\uparrow}, \end{aligned} \quad (6.11)$$

where we have classified the order parameter component according to each IR,

$$\begin{aligned} [\Delta_{A_{1g}}]_{\downarrow}^{\uparrow} &= \frac{1}{\mathcal{N}} \sum_{\mathbf{k}'} \sum_{\sigma} [U]_{\downarrow,\bar{\sigma}}^{\uparrow,\sigma} (\cos k'_x + \cos k'_y) \langle c_{-\mathbf{k}'\bar{\sigma}} c_{\mathbf{k}'\sigma} \rangle, \\ [\Delta_{B_{1g}}]_{\downarrow}^{\uparrow} &= \frac{1}{\mathcal{N}} \sum_{\mathbf{k}'} \sum_{\sigma} [U]_{\downarrow,\bar{\sigma}}^{\uparrow,\sigma} (\cos k'_x - \cos k'_y) \langle c_{-\mathbf{k}'\bar{\sigma}} c_{\mathbf{k}'\sigma} \rangle, \\ [\Delta_{E_{xu}}]_{\downarrow}^{\uparrow} &= \frac{1}{\mathcal{N}} \sum_{\mathbf{k}'} \sum_{\sigma} [U]_{\downarrow,\bar{\sigma}}^{\uparrow,\sigma} (-i\sqrt{2} \sin k'_x) \langle c_{-\mathbf{k}'\bar{\sigma}} c_{\mathbf{k}'\sigma} \rangle, \\ [\Delta_{E_{yu}}]_{\downarrow}^{\uparrow} &= \frac{1}{\mathcal{N}} \sum_{\mathbf{k}'} \sum_{\sigma} [U]_{\downarrow,\bar{\sigma}}^{\uparrow,\sigma} (-i\sqrt{2} \sin k'_y) \langle c_{-\mathbf{k}'\bar{\sigma}} c_{\mathbf{k}'\sigma} \rangle. \end{aligned} \quad (6.12)$$

As previously stated, in this notation the g and the u denote the even and the odd IR, respectively, which can be identified by distinguishing how the different form factors transform under $\mathbf{k} \rightarrow -\mathbf{k}$.

We also note that we have added an imaginary unit in the form factor for the odd irreducible representations. The origin of this comes from the fact that time reversal symmetry (TRS) must be preserved. Remembering that in momentum space TRS changes $\mathbf{k} \rightarrow -\mathbf{k}$, for an odd function such as $\sin(k_x)$ or $\sin(k_y)$, this symmetry would be broken [53]. However, since the TRS operator contains a complex conjugation, by adding the i factor we ensure that it is preserved.

The results obtained in this case for the order parameter in momentum space can be seen in Figure 6.1. With the purpose of studying the coexistence of two irreducible representations, we only consider the two even basis functions, corresponding to the A_{1g} and B_{1g} IRs, and we omit both E_g form factors. The expression for the electronic dispersion is the same as in the previous one-band model with on-site interactions, corresponding to $\xi_{\mathbf{k}} = -2t(\cos k_x + \cos k_y)$. As observed, depending on the value of the average electron density $\langle n \rangle$ we can obtain the two different solutions for the order parameter, one corresponding to a non-zero contribution from the A_{1g} order parameter (Figure 6.1a), whereas the other is given by the B_{1g} solution (Figure 6.1b).

Since it will be helpful to understand the coexistence of two irreducible representations, we can further investigate the dependence of the leading IR on the average electron density, as shown in Figure 6.2a. For a lower $\langle n \rangle$, the A_{1g} IR is the dominant one and the B_{1g} is suppressed, while for a larger $\langle n \rangle$ the opposite occurs. In particular, there is a range for the average electron density between approximately 0.35 and 0.5 where both phases coexist. Thus, it is also interesting to fix the electron density within this region and calculate the superconducting order parameters as a function of temperature for each irreducible representation, as plotted in Figure 6.2b by fixing $\langle n \rangle = 0.4$. Noticeably, each irreducible representation has a different transition temperature. As we will see in Chapter 8, this contrasts with the case of Sr_2RuO_4 , where different IRs seem to have the same critical temperature.

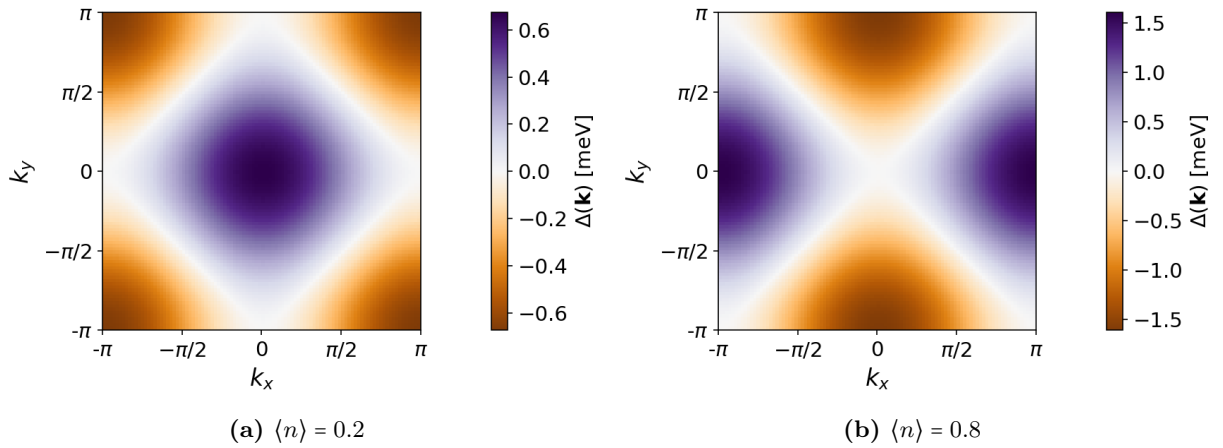


Figure 6.1: Superconducting order parameter in momentum space $\Delta(\mathbf{k})$ including nearest-neighbor interactions. We consider $N = 100$, $k_B T = 0.001t$ and $g = -t$, with $t = 1$ meV. We fix a different average electron density $\langle n \rangle$ in each case, as indicated in the captions.

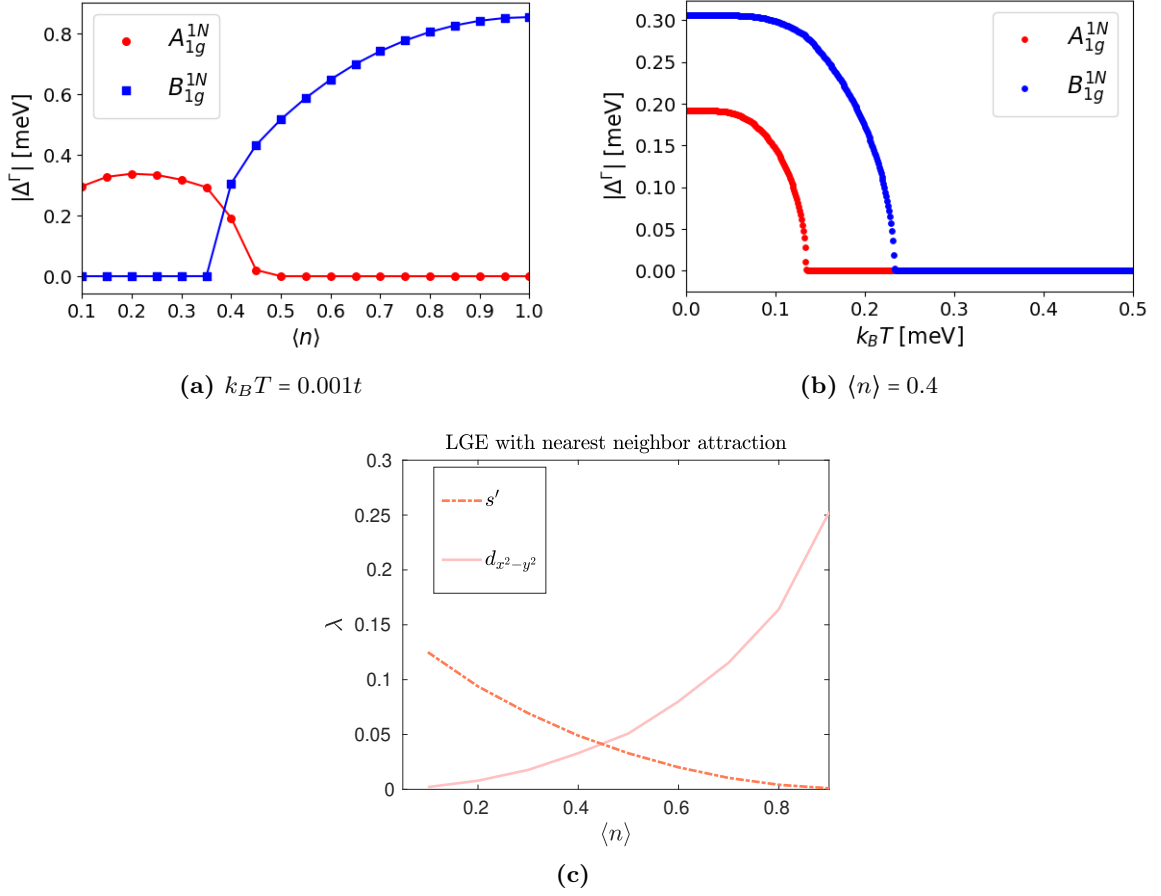


Figure 6.2: Superconducting order parameter irreducible representations $|\Delta^\Gamma|$ as a function of a) the average electron density $\langle n \rangle$ and b) temperature $k_B T$, including nearest-neighbors interactions. We consider in both cases $N = 100$, and $g = -t$, with $t = 1$ meV. In a) we take $k_B T = 0.001t$, while in b) $\langle n \rangle = 0.4$. In c) the results from the linearized gap equation are shown for the eigenvalues as a function of the average electron density, where the largest eigenvalue λ corresponds to the leading instability. This image was provided by Dr. Astrid T. Rømer.

Using the common notation for the superconducting state, the A_{1g} IR corresponds to an s' state, whereas the B_{1g} is the $d_{x^2-y^2}$. Therefore, depending on the electron density, we have found that it is possible to stabilize both an s -wave and a d -wave superconductor. It is also instructive to compare with the results from the linearized gap equation, shown in Figure 6.2c. Importantly, the region of coexistence agrees with the self-consistent outcome (Figure 6.2a). In the case of Sr_2RuO_4 , we will also seek agreement using both approaches.

The next question that arises is the state resulting from the coexistence, which in principle could be $s + d$ or $s + id$. With this purpose, we can check for time-reversal symmetry breaking. As it is well-known, in the usual spin basis $\{\uparrow, \downarrow\}$, the time-reversal symmetry operator is given

by $\Theta = i\sigma_y K$, where K denotes complex conjugation [53]. Since in our case there is a non-trivial phase between the s -wave and the d -wave channels, TRS is broken.

With these results in mind, it is extremely interesting to focus on the real space problem to see the effect of an impurity. For an $s + id$ superconductor, if a defect is introduced we expect the appearance of currents in the system, as a consequence of breaking TRS. The derivation presented in this section is based on the previous work in Ref. [54], where the current operator was introduced using the Bogoliubov transformations.

In the one-band model with nearest-neighbors interactions, the Hamiltonian in equation (4.9) can be written as

$$H^{\text{MF}} = - \sum_{\mathbf{R}, \mathbf{R}'} \sum_{\sigma} (t_{\mathbf{R}, \mathbf{R}'} + \mu_0 \delta_{\mathbf{R}, \mathbf{R}'}) \hat{c}_{\mathbf{R}\sigma}^{\dagger} \hat{c}_{\mathbf{R}'\sigma} + \frac{1}{2} \sum_{\mathbf{R}, \mathbf{R}'} \left(\Delta_{\mathbf{R}, \mathbf{R}'} (\hat{c}_{\mathbf{R}\uparrow}^{\dagger} \hat{c}_{\mathbf{R}'\downarrow}^{\dagger} - \hat{c}_{\mathbf{R}\downarrow}^{\dagger} \hat{c}_{\mathbf{R}'\uparrow}^{\dagger}) + \text{h.c.} \right), \quad (6.13)$$

where we have defined the order parameter to include only the singlet terms explicitly as

$$\Delta_{\mathbf{R}, \mathbf{R}'} = V_{\mathbf{R}, \mathbf{R}'} (\langle \hat{c}_{\mathbf{R}'\uparrow} \hat{c}_{\mathbf{R}\downarrow} \rangle - \langle \hat{c}_{\mathbf{R}'\downarrow} \hat{c}_{\mathbf{R}\uparrow} \rangle), \quad (6.14)$$

so that only the s -wave and d -wave superconducting states are included, omitting the odd-parity order parameters.

In order to introduce the local current operator, we need to define first a local polarization operator, corresponding to

$$\vec{P}_{\mathbf{R}} = \sum \vec{r}_i \hat{n}_{\mathbf{R}, \sigma}, \quad (6.15)$$

where $\hat{n}_{\mathbf{R}, \sigma} = \hat{c}_{\mathbf{R}, \sigma}^{\dagger} \hat{c}_{\mathbf{R}, \sigma}$. The change of polarization over time corresponds to a charge transfer, and therefore we can define the local current operator at site \mathbf{R} as

$$\langle \vec{J}_{\mathbf{R}} \rangle = \left\langle \frac{\partial \vec{P}_{\mathbf{R}}}{\partial t} \right\rangle = i \langle [H^{\text{MF}}, \vec{P}_{\mathbf{R}}] \rangle = -it \sum_{\sigma, \hat{\delta}} \hat{\delta} \left\langle \hat{c}_{\mathbf{R}, \sigma}^{\dagger} \hat{c}_{\mathbf{R}+\hat{\delta}, \sigma}^{\dagger} + \text{h.c.} \right\rangle, \quad (6.16)$$

where $\hat{\delta} = \{\pm\hat{x}, \pm\hat{y}\}$ denotes the nearest neighbors, and we consider the same hopping t for all first neighbors. Using the Bogoliubov transformation, we can rewrite it as

$$\langle \vec{J}_{\mathbf{R}} \rangle = -2t \sum_{n, \hat{\delta}} \hat{\delta} \text{Im} [u_{\mathbf{R}+\hat{\delta}\uparrow}^* u_{\mathbf{R}\uparrow} f(E_n) + v_{\mathbf{R}+\hat{\delta}\downarrow}^* v_{\mathbf{R}\downarrow} f(-E_n)]. \quad (6.17)$$

Therefore, with this result we are able to study the currents at each site in the region of coexistence of both phases when an impurity is included in the center site, as shown in Figure 6.3. In this case, we choose to fix the chemical potential, corresponding to an electron density of $\langle n \rangle = 0.45$. Importantly, we see the existence of a supercurrent, which breaks TRS. We also note that C_4 symmetry is broken due to the coexistence with a B_{1g} IR. Moreover, we observe the presence of current loops along the $\pm\pi/2$ directions.

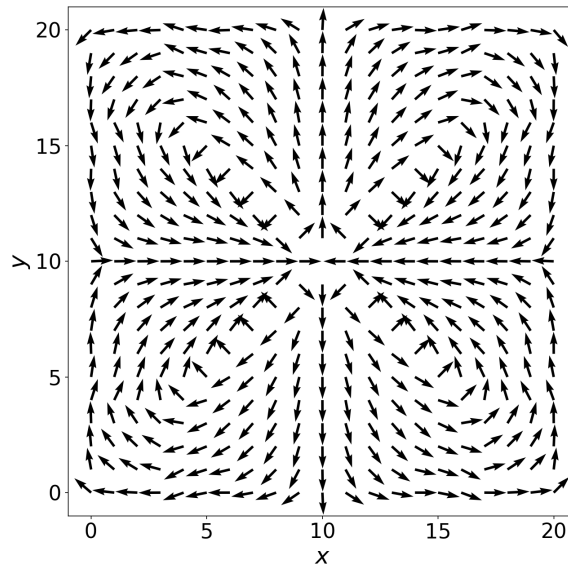


Figure 6.3: Current structure for an $s + id$ superconductor with an impurity in the center site. The local currents are normalized with $|\vec{J}_i|$. We consider a system size 21×21 , $\mu = -1.72$, $g = -t$, $k_B T = 0.001t$ and $V_{\text{imp}} = 3t$, with $t = 1$ meV.

Chapter 7

Spin-fluctuation mediated pairing

In this section, we assume that superconductivity originates from a spin-fluctuation mechanism. As previously remarked, until now superconductivity has been included by inducing an effective attractive interaction ($U, g < 0$) between electrons on the same site and nearest neighbors. In order to construct a realistic model for Sr_2RuO_4 , we will compute the order parameter components by introducing interaction potentials describing spin-fluctuations. Since the calculation of the pairing interactions is complicated and could be a separate project by itself, we will just present a brief overview of its derivation. More information on the details of the origin of the spin-fluctuation strength can be found in the Supplementary Material of Ref. [9].

The effective electron-electron interaction in the Cooper channel is derived from the multi-orbital Hubbard Hamiltonian, including intra- and interorbital Coulomb interactions and Hund's coupling terms. It is calculated by considering higher-order interactions derived diagrammatically from ladder and bubble diagrams, describing transverse and longitudinal spin fluctuations, respectively. To obtain the final form of the interaction all ladder and bubble diagrams are summed to infinite order. Finally, the interaction is expressed in terms of the bare parameters U, U', J, J' and the random phase approximation (RPA) spin susceptibilities. With this procedure, the interaction Hamiltonian corresponds to

$$H_{SC}^{SF} = \frac{1}{2} \sum_{\mathbf{k}, \mathbf{k}', \{\tilde{\mu}\}} [V(\mathbf{k}, \mathbf{k}')]_{\tilde{\mu}_3, \tilde{\mu}_4}^{\tilde{\mu}_1, \tilde{\mu}_2} c_{\mathbf{k}\tilde{\mu}_1}^\dagger c_{-\mathbf{k}\tilde{\mu}_3}^\dagger c_{-\mathbf{k}'\tilde{\mu}_2} c_{\mathbf{k}'\tilde{\mu}_4}, \quad (7.1)$$

where the pairing interaction is given by

$$[V(\mathbf{k}, \mathbf{k}')]_{\tilde{\mu}_3, \tilde{\mu}_4}^{\tilde{\mu}_1, \tilde{\mu}_2} = [U]_{\tilde{\mu}_3, \tilde{\mu}_4}^{\tilde{\mu}_1, \tilde{\mu}_2} + \left[U \frac{1}{1 - \chi_0 U} \chi_0 U \right]_{\tilde{\mu}_3, \tilde{\mu}_4}^{\tilde{\mu}_1, \tilde{\mu}_2} (\mathbf{k} + \mathbf{k}') - \left[U \frac{1}{1 - \chi_0 U} \chi_0 U \right]_{\tilde{\mu}_3, \tilde{\mu}_2}^{\tilde{\mu}_1, \tilde{\mu}_4} (\mathbf{k} - \mathbf{k}'). \quad (7.2)$$

In the expression above, $\chi_0 = [\chi_0]_{\tilde{\mu}_3, \tilde{\mu}_4}^{\tilde{\mu}_1, \tilde{\mu}_2}(\mathbf{q}, i\omega_n = 0)$ corresponds to the real part of the generalized multi-orbital spin susceptibility in the presence of spin-orbit coupling.

In this part of the thesis, we focus on the comparison of four Hund's couplings, $J = \{0, 12, 24, 36\}$ meV, whereas $U = 120$ meV is kept fixed, so that we are allowed to move in

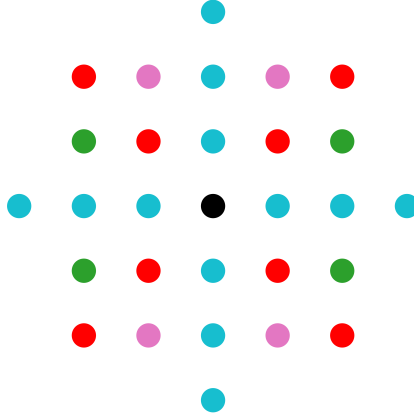


Figure 7.1: Neighbors considered for each lattice point (in black) when the spin-fluctuation pairing mechanism is included. The colors represent different form factors, since in a certain direction for further neighbors we will obtain higher harmonics of the same functions.

a horizontal line in the phase diagram in Figure 3.2. Rotational symmetry is assumed, and therefore we consider $J' = J$ and $U' = U - 2J$. As previously stated, the band is parametrized by $\{t_1, t_2, t_3, t_4, t_5, t'\} = \{88, 9, 80, 40, 5, 0\}$ meV, a spin-orbit coupling $\lambda_{\text{SOC}} = 35$ meV, and for the initial chemical potential $\mu = 109$ meV, since the electron density will be kept fixed to 4. Note that since spin-orbit coupling is much larger than the hybridization $g(\mathbf{k})$, the latter can be set to zero when spin-orbit coupling is finite. In addition, it is also remarked that spin-orbit coupling is included both in the electronic structure and the pairing interaction.

Since it is difficult to truncate the interactions coming from perturbation theory, we start from a real-space picture, where only up to sixth nearest neighbors are included, as illustrated in Figure 7.1. Therefore, the interactions are Fourier transformed to real space using a numerical code, and the corresponding pairing strengths for each J value are provided in different data files¹, which include

$$(x, y) \quad \mu_1 \quad \mu_2 \quad \mu_3 \quad \mu_4 \quad \sigma_1 \quad \sigma_2 \quad \sigma_3 \quad \sigma_4 \quad V' \quad V'', \quad (7.3)$$

where for our picture $x, y = \{-3, -2, -1, 0, 1, 2, 3\}$, the orbital and spin indices are the ones appearing in equation (7.1), and V' refers to the real part of the interaction potential, whereas V'' corresponds to the imaginary part. This pairing potential does not include the bare interaction given by U, J, U', J' (previously presented in equation (3.7)), so we have to add it separately. Notice that since now $U, J > 0$, the inclusion of this term will result in a strong on-site repulsion.

¹The files with the pairing strength including higher order interactions are provided by Dr. Astrid T. Rømer.

In order to find superconductivity through the self-consistent calculation, we are allowed to boost the interactions provided,

$$\begin{aligned} V' &\longrightarrow \alpha V', \\ V'' &\longrightarrow \alpha V'', \end{aligned} \quad (7.4)$$

where α is the boost parameter. The effect of the boost will be discussed in the results Chapter, as we will see that due to the multi-orbital model the boost does not change the results in a linear way, and new phases may appear if the boost is too large.

Hence, since we are interested in solving for the order parameter in \mathbf{k} -space, we can do a Fourier transformation from the real space interactions,

$$V(\mathbf{q}) = \sum_{i,j} e^{-i\mathbf{q}\cdot\mathbf{r}_{ij}} V(\mathbf{r}_{ij}), \quad (7.5)$$

where i, j denote the real space coordinates. This allows us to perform a similar study in terms of the irreducible representations as in the previous one-band model with off-site interactions.

The next step is to find an expression for the gap in momentum space. To do so, we need to recall equation (4.21),

$$[\Delta_{\mathbf{k}}]_{\tilde{\mu}_j}^{\tilde{\mu}_i} = \frac{1}{\mathcal{N}} \sum_{\mathbf{k}'} \sum_{\tilde{\mu}_k, \tilde{\mu}_l} [V_{\mathbf{k}, \mathbf{k}'}]_{\tilde{\mu}_j, \tilde{\mu}_l}^{\tilde{\mu}_i, \tilde{\mu}_k} \langle \hat{c}_{-\mathbf{k}'\tilde{\mu}_l} \hat{c}_{\mathbf{k}'\tilde{\mu}_k} \rangle. \quad (7.6)$$

We have to be very careful now since the Fourier transform is made in \mathbf{q} , so that to transform back to \mathbf{k} -space we need to introduce the symmetrized pairing interaction, as defined in equation (4) of Ref. [9]. Therefore, the gap equation becomes

$$[\Delta_{\mathbf{k}}]_{\tilde{\mu}_j}^{\tilde{\mu}_i} = \frac{1}{\mathcal{N}} \sum_{\mathbf{k}'} \sum_{\tilde{\mu}_k, \tilde{\mu}_l} \left([U]_{\tilde{\mu}_j, \tilde{\mu}_l}^{\tilde{\mu}_i, \tilde{\mu}_k} + [V_{\mathbf{k}+\mathbf{k}'}]_{\tilde{\mu}_j, \tilde{\mu}_l}^{\tilde{\mu}_i, \tilde{\mu}_k} - [V_{\mathbf{k}-\mathbf{k}'}]_{\tilde{\mu}_j, \tilde{\mu}_l}^{\tilde{\mu}_i, \tilde{\mu}_k} \right) \langle \hat{c}_{-\mathbf{k}'\tilde{\mu}_l} \hat{c}_{\mathbf{k}'\tilde{\mu}_k} \rangle, \quad (7.7)$$

where $[U]_{\tilde{\mu}_j, \tilde{\mu}_l}^{\tilde{\mu}_i, \tilde{\mu}_k}$ refers to the bare interaction in equation (3.7). Note that the full interaction above by construction fulfills the symmetries in equation (4.23),

$$[V_{\mathbf{k}-\mathbf{k}'}]_{\tilde{\mu}_j, \tilde{\mu}_l}^{\tilde{\mu}_i, \tilde{\mu}_k} = -[V_{\mathbf{k}+\mathbf{k}'}]_{\tilde{\mu}_j, \tilde{\mu}_k}^{\tilde{\mu}_i, \tilde{\mu}_l} = -[V_{-\mathbf{k}-\mathbf{k}'}]_{\tilde{\mu}_i, \tilde{\mu}_l}^{\tilde{\mu}_j, \tilde{\mu}_k}, \quad (7.8)$$

as required due to fermionic statistics.

From the expression (7.7) for the gap, we can introduce the Fourier transform so that we can write it as a function of the real space pairings,

$$\begin{aligned} [\Delta_{\mathbf{k}}]_{\tilde{\mu}_j}^{\tilde{\mu}_i} &= \frac{1}{\mathcal{N}} \sum_{\mathbf{k}'} \sum_{\tilde{\mu}_k, \tilde{\mu}_l} \left([U]_{\tilde{\mu}_j, \tilde{\mu}_l}^{\tilde{\mu}_i, \tilde{\mu}_k} + \sum_{i,j} [V(\mathbf{r}_{ij})]_{\tilde{\mu}_j, \tilde{\mu}_l}^{\tilde{\mu}_i, \tilde{\mu}_k} e^{-i(\mathbf{k}+\mathbf{k}')\cdot\mathbf{r}_{ij}} - \sum_{i,j} [V(\mathbf{r}_{ij})]_{\tilde{\mu}_j, \tilde{\mu}_k}^{\tilde{\mu}_i, \tilde{\mu}_l} e^{-i(\mathbf{k}-\mathbf{k}')\cdot\mathbf{r}_{ij}} \right) \\ &\quad \times \langle \hat{c}_{-\mathbf{k}'\tilde{\mu}_l} \hat{c}_{\mathbf{k}'\tilde{\mu}_k} \rangle, \end{aligned} \quad (7.9)$$

where it is the last term $[V(\mathbf{r}_{ij})]_{\tilde{\mu}_j, \tilde{\mu}_k}^{\tilde{\mu}_i, \tilde{\mu}_l}$ the one stated in the pairing real space file.

Then, we can follow the same approach as in the previous one-band model to obtain the equation for the superconducting order parameter, so that we separate into different IR. Even though this may seem more complicated, it presents two important advantages. On the one hand, we are able to characterize the IR in orbital and spin space. On the other hand, a major computational speed increase is obtained in the numerical code, since we do not need to perform a sum in \mathbf{k}' for all \mathbf{k} , and larger system sizes can be studied.

7.1 Identification of the irreducible representations

In this three-band model including off-site interactions, it is no longer true that the order parameter is always even under $\mathbf{k} \rightarrow -\mathbf{k}$. Recalling equation (6.8) for the order parameter, we can separate the odd and the even irreducible representations based on the form factor $g_{\mathbf{k}}^{\Gamma}$,

$$[\Delta_{\mathbf{k}}]_{\tilde{\mu}_j}^{\tilde{\mu}_i} = \sum_{\Gamma \in \text{IR}} g_{\mathbf{k}}^{\Gamma} [\Delta_{\Gamma}]_{\tilde{\mu}_j}^{\tilde{\mu}_i} = \sum_{\Gamma_g \in \text{IR}} g_{\mathbf{k}}^{\Gamma_g} [\Delta_{\Gamma_g}]_{\tilde{\mu}_j}^{\tilde{\mu}_i} + \sum_{\Gamma_u \in \text{IR}} g_{\mathbf{k}}^{\Gamma_u} [\Delta_{\Gamma_u}]_{\tilde{\mu}_j}^{\tilde{\mu}_i}, \quad (7.10)$$

where Γ_g and Γ_u correspond to the even and odd basis functions, respectively. Therefore, we need to consider again the implications of the symmetry $[\Delta_{\mathbf{k}}]_{\tilde{\mu}_j}^{\tilde{\mu}_i} = -[\Delta_{-\mathbf{k}}]_{\tilde{\mu}_i}^{\tilde{\mu}_j}$, which become more clear when considering the inverse relation $[\Delta_{\Gamma}]_{\tilde{\mu}_j}^{\tilde{\mu}_i} = \frac{1}{N} \sum_{\mathbf{k}} (g_{\mathbf{k}}^{\Gamma})^* [\Delta_{\mathbf{k}}]_{\tilde{\mu}_j}^{\tilde{\mu}_i}$.

We consider both cases separately, and take first the case for even form factors, which fulfill $g_{-\mathbf{k}}^{\Gamma_g} = g_{\mathbf{k}}^{\Gamma_g}$. In this case, since the symmetry for the order parameter leads to $[\Delta_{\Gamma_g}]_{\tilde{\mu}_j}^{\tilde{\mu}_i} = -[\Delta_{\Gamma_g}]_{\tilde{\mu}_i}^{\tilde{\mu}_j}$, to identify the IR in spin/orbital space the procedure is similar to the on-site superconductivity. In the same way as in equation (5.36), we can construct the matrix

$$\hat{\Delta}_{\Gamma_g} = \begin{pmatrix} 0 & [\Delta_{\Gamma_g}]_{1\downarrow}^{1\uparrow} & [\Delta_{\Gamma_g}]_{2\uparrow}^{1\uparrow} & [\Delta_{\Gamma_g}]_{2\downarrow}^{1\uparrow} & [\Delta_{\Gamma_g}]_{3\uparrow}^{1\uparrow} & [\Delta_{\Gamma_g}]_{3\downarrow}^{1\uparrow} \\ -[\Delta_{\Gamma_g}]_{1\downarrow}^{1\uparrow} & 0 & [\Delta_{\Gamma_g}]_{2\uparrow}^{1\downarrow} & [\Delta_{\Gamma_g}]_{2\downarrow}^{1\downarrow} & [\Delta_{\Gamma_g}]_{3\uparrow}^{1\downarrow} & [\Delta_{\Gamma_g}]_{3\downarrow}^{1\downarrow} \\ -[\Delta_{\Gamma_g}]_{2\uparrow}^{1\uparrow} & -[\Delta_{\Gamma_g}]_{2\uparrow}^{1\downarrow} & 0 & [\Delta_{\Gamma_g}]_{2\downarrow}^{2\uparrow} & [\Delta_{\Gamma_g}]_{3\uparrow}^{2\uparrow} & [\Delta_{\Gamma_g}]_{3\downarrow}^{2\uparrow} \\ -[\Delta_{\Gamma_g}]_{2\downarrow}^{1\uparrow} & -[\Delta_{\Gamma_g}]_{2\downarrow}^{1\downarrow} & -[\Delta_{\Gamma_g}]_{2\downarrow}^{2\uparrow} & 0 & [\Delta_{\Gamma_g}]_{3\uparrow}^{2\downarrow} & [\Delta_{\Gamma_g}]_{3\downarrow}^{2\downarrow} \\ -[\Delta_{\Gamma_g}]_{3\uparrow}^{1\uparrow} & -[\Delta_{\Gamma_g}]_{3\uparrow}^{1\downarrow} & -[\Delta_{\Gamma_g}]_{3\uparrow}^{2\uparrow} & -[\Delta_{\Gamma_g}]_{3\uparrow}^{2\downarrow} & 0 & [\Delta_{\Gamma_g}]_{3\downarrow}^{3\uparrow} \\ -[\Delta_{\Gamma_g}]_{3\downarrow}^{1\uparrow} & -[\Delta_{\Gamma_g}]_{3\downarrow}^{1\downarrow} & -[\Delta_{\Gamma_g}]_{3\downarrow}^{2\uparrow} & -[\Delta_{\Gamma_g}]_{3\downarrow}^{2\downarrow} & -[\Delta_{\Gamma_g}]_{3\downarrow}^{3\uparrow} & 0 \end{pmatrix}. \quad (7.11)$$

Following the same calculations and using the convenient notation $\hat{\Delta} = i(\hat{\psi} + \hat{d} \cdot \boldsymbol{\sigma})\sigma_y$ for the order parameter, we obtain the results summarized in Table 7.1.

As in the case of on-site interactions, we can see that in Table 7.1 there are four reducible representations. Hence, following the same procedure explained in section 5.3.2, it is convenient to write them into four irreducible representations, since then we know how they behave under the point group operations. The four resulting IRs are written in Table 7.2.

Table 7.1: Combinations of the order parameter matrix components transforming as irreducible representations of the point group D_{4h} that couple with an even form factor $g_{-\mathbf{k}}^{\Gamma_g} = g_{\mathbf{k}}^{\Gamma_g}$. We include how each combination couples to orbital and spin space, and specify if they correspond to triplet or singlet.

$\hat{\Delta}_{\Gamma_g}$	Orbital Space	λ	Spin space	σ	IR
$\frac{1}{3}([\Delta_{\Gamma_g}]_{1\downarrow}^{1\uparrow} + [\Delta_{\Gamma_g}]_{2\downarrow}^{2\uparrow} + [\Delta_{\Gamma_g}]_{3\downarrow}^{3\uparrow})$	Triplet, Intra	$\mathbf{1}_\lambda$	Singlet	$\mathbf{1}_\sigma$	A_{1g}
$\frac{1}{2}([\Delta_{\Gamma_g}]_{2\downarrow}^{1\uparrow} - [\Delta_{\Gamma_g}]_{2\uparrow}^{1\downarrow})$	Triplet	λ_1	Singlet	$\mathbf{1}_\sigma$	B_{2g}
$\frac{1}{2}([\Delta_{\Gamma_g}]_{1\downarrow}^{1\uparrow} - [\Delta_{\Gamma_g}]_{2\downarrow}^{2\uparrow})$	Triplet, Intra	λ_3	Singlet	$\mathbf{1}_\sigma$	B_{1g}
$\frac{1}{2}([\Delta_{\Gamma_g}]_{3\downarrow}^{1\uparrow} - [\Delta_{\Gamma_g}]_{3\uparrow}^{1\downarrow})$	Triplet	λ_4	Singlet	$\mathbf{1}_\sigma$	$E_{yg}(i)$
$\frac{1}{2}([\Delta_{\Gamma_g}]_{3\downarrow}^{2\uparrow} - [\Delta_{\Gamma_g}]_{3\uparrow}^{2\downarrow})$	Triplet	λ_6	Singlet	$\mathbf{1}_\sigma$	$E_{xg}(i)$
$\frac{1}{2\sqrt{3}}([\Delta_{\Gamma_g}]_{1\downarrow}^{1\uparrow} + [\Delta_{\Gamma_g}]_{2\downarrow}^{2\uparrow} - 2[\Delta_{\Gamma_g}]_{3\downarrow}^{3\uparrow})$	Triplet, Intra	λ_8	Singlet	$\mathbf{1}_\sigma$	A_{1g}
$\frac{1}{2}([\Delta_{\Gamma_g}]_{2\uparrow}^{1\uparrow} + [\Delta_{\Gamma_g}]_{2\downarrow}^{1\downarrow})$	Singlet	λ_2	Triplet	σ_y	$E_{yg}(ii)$
$\frac{i}{2}([\Delta_{\Gamma_g}]_{2\downarrow}^{1\uparrow} + [\Delta_{\Gamma_g}]_{2\uparrow}^{1\downarrow})$	Singlet	λ_2	Triplet	σ_z	A_{1g}
$\frac{-i}{2}([\Delta_{\Gamma_g}]_{2\uparrow}^{1\uparrow} - [\Delta_{\Gamma_g}]_{2\downarrow}^{1\downarrow})$	Singlet	λ_2	Triplet	σ_x	$E_{xg}(ii)$
$\frac{1}{2}([\Delta_{\Gamma_g}]_{3\uparrow}^{1\uparrow} + [\Delta_{\Gamma_g}]_{3\downarrow}^{1\downarrow})$	Singlet	λ_5	Triplet	σ_y	Reducible
$\frac{i}{2}([\Delta_{\Gamma_g}]_{3\downarrow}^{1\uparrow} + [\Delta_{\Gamma_g}]_{3\uparrow}^{1\downarrow})$	Singlet	λ_5	Triplet	σ_z	$E_{yg}(iii)$
$\frac{-i}{2}([\Delta_{\Gamma_g}]_{3\uparrow}^{1\uparrow} - [\Delta_{\Gamma_g}]_{3\downarrow}^{1\downarrow})$	Singlet	λ_5	Triplet	σ_x	Reducible
$\frac{1}{2}([\Delta_{\Gamma_g}]_{3\uparrow}^{2\uparrow} + [\Delta_{\Gamma_g}]_{3\downarrow}^{2\downarrow})$	Singlet	λ_7	Triplet	σ_y	Reducible
$\frac{i}{2}([\Delta_{\Gamma_g}]_{3\downarrow}^{2\uparrow} + [\Delta_{\Gamma_g}]_{3\uparrow}^{2\downarrow})$	Singlet	λ_7	Triplet	σ_z	$E_{xg}(iii)$
$\frac{-i}{2}([\Delta_{\Gamma_g}]_{3\uparrow}^{2\uparrow} - [\Delta_{\Gamma_g}]_{3\downarrow}^{2\downarrow})$	Singlet	λ_7	Triplet	σ_x	Reducible

Table 7.2: Irreducible representations coupling to an even form factor obtained by combining the four reducible representations in Table 7.1.

$\hat{\Delta}_{\Gamma_g}$	Combined spin and orbital	Orbital	Spin	IR
$\frac{1}{4}([\Delta_{\Gamma_g}]_{3\uparrow}^{1\uparrow} + [\Delta_{\Gamma_g}]_{3\downarrow}^{1\downarrow} - i([\Delta_{\Gamma_g}]_{3\uparrow}^{2\uparrow} - [\Delta_{\Gamma_g}]_{3\downarrow}^{2\downarrow}))$	$\lambda_5\sigma_y + \lambda_7\sigma_x$	Singlet	Triplet	A_{2g}
$\frac{1}{4}([\Delta_{\Gamma_g}]_{3\uparrow}^{1\uparrow} + [\Delta_{\Gamma_g}]_{3\downarrow}^{1\downarrow} + i([\Delta_{\Gamma_g}]_{3\uparrow}^{2\uparrow} - [\Delta_{\Gamma_g}]_{3\downarrow}^{2\downarrow}))$	$\lambda_5\sigma_y - \lambda_7\sigma_x$	Singlet	Triplet	B_{2g}
$\frac{1}{4}(-i([\Delta_{\Gamma_g}]_{3\uparrow}^{1\uparrow} - [\Delta_{\Gamma_g}]_{3\downarrow}^{1\downarrow}) + [\Delta_{\Gamma_g}]_{3\uparrow}^{2\uparrow} + [\Delta_{\Gamma_g}]_{3\downarrow}^{2\downarrow})$	$\lambda_5\sigma_x + \lambda_7\sigma_y$	Singlet	Triplet	B_{1g}
$\frac{1}{4}(-i([\Delta_{\Gamma_g}]_{3\uparrow}^{1\uparrow} - [\Delta_{\Gamma_g}]_{3\downarrow}^{1\downarrow}) - [\Delta_{\Gamma_g}]_{3\uparrow}^{2\uparrow} - [\Delta_{\Gamma_g}]_{3\downarrow}^{2\downarrow})$	$\lambda_5\sigma_x - \lambda_7\sigma_y$	Singlet	Triplet	A_{1g}

Secondly, we consider the case of odd form factors, $g_{-\mathbf{k}}^{\Gamma_u} = -g_{\mathbf{k}}^{\Gamma_u}$. The symmetry for the order parameter leads now to $[\Delta_{\Gamma_u}]_{\tilde{\mu}_j}^{\tilde{\mu}_i} = [\Delta_{\Gamma_u}]_{\tilde{\mu}_i}^{\tilde{\mu}_j}$. Hence, the 6×6 matrix in orbital and spin space corresponds to

$$\hat{\Delta}_{\Gamma_u} = \begin{pmatrix} [\Delta_{\Gamma_u}]_{1\uparrow}^{1\uparrow} & [\Delta_{\Gamma_u}]_{1\downarrow}^{1\uparrow} & [\Delta_{\Gamma_u}]_{2\uparrow}^{1\uparrow} & [\Delta_{\Gamma_u}]_{2\downarrow}^{1\uparrow} & [\Delta_{\Gamma_u}]_{3\uparrow}^{1\uparrow} & [\Delta_{\Gamma_u}]_{3\downarrow}^{1\uparrow} \\ [\Delta_{\Gamma_u}]_{1\downarrow}^{1\uparrow} & [\Delta_{\Gamma_u}]_{1\downarrow}^{1\downarrow} & [\Delta_{\Gamma_u}]_{2\uparrow}^{1\downarrow} & [\Delta_{\Gamma_u}]_{2\downarrow}^{1\downarrow} & [\Delta_{\Gamma_u}]_{3\uparrow}^{1\downarrow} & [\Delta_{\Gamma_u}]_{3\downarrow}^{1\downarrow} \\ [\Delta_{\Gamma_u}]_{2\uparrow}^{1\uparrow} & [\Delta_{\Gamma_u}]_{2\uparrow}^{1\downarrow} & [\Delta_{\Gamma_u}]_{2\uparrow}^{2\uparrow} & [\Delta_{\Gamma_u}]_{2\downarrow}^{2\uparrow} & [\Delta_{\Gamma_u}]_{3\uparrow}^{2\uparrow} & [\Delta_{\Gamma_u}]_{3\downarrow}^{2\uparrow} \\ [\Delta_{\Gamma_u}]_{2\downarrow}^{1\uparrow} & [\Delta_{\Gamma_u}]_{2\downarrow}^{1\downarrow} & [\Delta_{\Gamma_u}]_{2\uparrow}^{2\downarrow} & [\Delta_{\Gamma_u}]_{2\downarrow}^{2\downarrow} & [\Delta_{\Gamma_u}]_{3\uparrow}^{2\downarrow} & [\Delta_{\Gamma_u}]_{3\downarrow}^{2\downarrow} \\ [\Delta_{\Gamma_u}]_{3\uparrow}^{1\uparrow} & [\Delta_{\Gamma_u}]_{3\uparrow}^{1\downarrow} & [\Delta_{\Gamma_u}]_{3\uparrow}^{2\uparrow} & [\Delta_{\Gamma_u}]_{3\uparrow}^{2\downarrow} & [\Delta_{\Gamma_u}]_{3\uparrow}^{3\uparrow} & [\Delta_{\Gamma_u}]_{3\downarrow}^{3\uparrow} \\ [\Delta_{\Gamma_u}]_{3\downarrow}^{1\uparrow} & [\Delta_{\Gamma_u}]_{3\downarrow}^{1\downarrow} & [\Delta_{\Gamma_u}]_{3\downarrow}^{2\uparrow} & [\Delta_{\Gamma_u}]_{3\downarrow}^{2\downarrow} & [\Delta_{\Gamma_u}]_{3\downarrow}^{3\uparrow} & [\Delta_{\Gamma_u}]_{3\downarrow}^{3\downarrow} \end{pmatrix}. \quad (7.12)$$

Using the same procedure, this matrix can be rewritten using the Pauli and Gell-Mann matrices for spin and orbital space, respectively. The combinations found in this case can be seen in Table 7.4. Likewise, we find four reducible representations, which again can be combined to lead to irreducible representations, as shown in Table 7.3. It is important to remark that the results presented in both tables are in agreement with the ones in Appendix C of Ref. [31].

Table 7.3: Irreducible representations coupling to an odd form factor obtained by combining the four reducible representations in Table 7.4.

$\hat{\Delta}_{\Gamma_u}$	Combined spin and orbital	Orbital	Spin	IR
$\frac{-1}{4}(i[\Delta_{\Gamma_u}]_{3\uparrow}^{1\uparrow} + i[\Delta_{\Gamma_u}]_{3\downarrow}^{1\downarrow} + [\Delta_{\Gamma_u}]_{3\uparrow}^{2\uparrow} - [\Delta_{\Gamma_u}]_{3\downarrow}^{2\downarrow})$	$\lambda_4\sigma_y + \lambda_6\sigma_x$	Triplet	Triplet	A_{2g}
$\frac{-1}{4}(i[\Delta_{\Gamma_u}]_{3\uparrow}^{1\uparrow} + i[\Delta_{\Gamma_u}]_{3\downarrow}^{1\downarrow} - [\Delta_{\Gamma_u}]_{3\uparrow}^{2\uparrow} + [\Delta_{\Gamma_u}]_{3\downarrow}^{2\downarrow})$	$\lambda_4\sigma_y - \lambda_6\sigma_x$	Triplet	Triplet	B_{2g}
$\frac{-1}{4}([\Delta_{\Gamma_u}]_{3\uparrow}^{1\uparrow} - [\Delta_{\Gamma_u}]_{3\downarrow}^{1\downarrow}) + i[\Delta_{\Gamma_u}]_{3\uparrow}^{2\uparrow} + i[\Delta_{\Gamma_u}]_{3\downarrow}^{2\downarrow})$	$\lambda_4\sigma_x + \lambda_6\sigma_y$	Triplet	Triplet	B_{1g}
$\frac{-1}{4}([\Delta_{\Gamma_u}]_{3\uparrow}^{1\uparrow} - [\Delta_{\Gamma_u}]_{3\downarrow}^{1\downarrow}) - i[\Delta_{\Gamma_u}]_{3\uparrow}^{2\uparrow} - i[\Delta_{\Gamma_u}]_{3\downarrow}^{2\downarrow})$	$\lambda_4\sigma_x - \lambda_6\sigma_y$	Triplet	Triplet	A_{1g}

Table 7.4: Combinations of the order parameter matrix components transforming as irreducible representations of the point group D_{4h} that couple with an odd form factor $g_{-\mathbf{k}}^{\Gamma_u} = -g_{\mathbf{k}}^{\Gamma_u}$. We include how each combination couples to orbital and spin space, and specify if they correspond to triplet or singlet.

$\hat{\Delta}_{\Gamma_u}$	Orbital Space	λ	Spin space	σ	IR
$\frac{i}{2}([\Delta_{\Gamma_u}]_{2\downarrow}^{1\uparrow} - [\Delta_{\Gamma_u}]_{2\uparrow}^{1\downarrow})$	Singlet	λ_2	Singlet	$\mathbb{1}_\sigma$	A_{2g}
$\frac{i}{2}([\Delta_{\Gamma_u}]_{3\downarrow}^{1\uparrow} - [\Delta_{\Gamma_u}]_{3\uparrow}^{1\downarrow})$	Singlet	λ_5	Singlet	$\mathbb{1}_\sigma$	$E_{yg}(i)$
$\frac{i}{2}([\Delta_{\Gamma_u}]_{3\downarrow}^{2\uparrow} - [\Delta_{\Gamma_u}]_{3\uparrow}^{2\downarrow})$	Singlet	λ_7	Singlet	$\mathbb{1}_\sigma$	$E_{xg}(i)$
$\frac{-i}{6}([\Delta_{\Gamma_u}]_{1\uparrow}^{1\uparrow} + [\Delta_{\Gamma_u}]_{1\downarrow}^{1\downarrow} + [\Delta_{\Gamma_u}]_{2\uparrow}^{2\uparrow} + [\Delta_{\Gamma_u}]_{2\downarrow}^{2\downarrow} + [\Delta_{\Gamma_u}]_{3\uparrow}^{3\uparrow} + [\Delta_{\Gamma_u}]_{3\downarrow}^{3\downarrow})$	Triplet, Intra	$\mathbb{1}_\lambda$	Triplet	σ_y	$E_{yg}(ii)$
$\frac{1}{3}([\Delta_{\Gamma_u}]_{1\downarrow}^{1\uparrow} + [\Delta_{\Gamma_u}]_{2\downarrow}^{2\uparrow} + [\Delta_{\Gamma_u}]_{3\downarrow}^{3\uparrow})$	Triplet, Intra	$\mathbb{1}_\lambda$	Triplet	σ_z	A_{2g}
$\frac{-1}{6}([\Delta_{\Gamma_u}]_{1\uparrow}^{1\uparrow} - [\Delta_{\Gamma_u}]_{1\downarrow}^{1\downarrow} + [\Delta_{\Gamma_u}]_{2\uparrow}^{2\uparrow} - [\Delta_{\Gamma_u}]_{2\downarrow}^{2\downarrow} + [\Delta_{\Gamma_u}]_{3\uparrow}^{3\uparrow} - [\Delta_{\Gamma_u}]_{3\downarrow}^{3\downarrow})$	Triplet, Intra	$\mathbb{1}_\lambda$	Triplet	σ_x	$E_{xg}(ii)$
$\frac{-i}{2}([\Delta_{\Gamma_u}]_{2\uparrow}^{1\uparrow} + [\Delta_{\Gamma_u}]_{2\downarrow}^{1\downarrow})$	Triplet	λ_1	Triplet	σ_y	$E_{yg}(iii)$
$\frac{1}{2}([\Delta_{\Gamma_u}]_{2\downarrow}^{1\uparrow} + [\Delta_{\Gamma_u}]_{2\uparrow}^{1\downarrow})$	Triplet	λ_1	Triplet	σ_z	B_{1g}
$\frac{-1}{2}([\Delta_{\Gamma_u}]_{2\uparrow}^{1\uparrow} - [\Delta_{\Gamma_u}]_{2\downarrow}^{1\downarrow})$	Triplet	λ_1	Triplet	σ_x	$E_{xg}(iii)$
$\frac{-i}{4}([\Delta_{\Gamma_u}]_{1\uparrow}^{1\uparrow} + [\Delta_{\Gamma_u}]_{1\downarrow}^{1\downarrow} - [\Delta_{\Gamma_u}]_{2\uparrow}^{2\uparrow} - [\Delta_{\Gamma_u}]_{2\downarrow}^{2\downarrow})$	Triplet, Intra	λ_3	Triplet	σ_y	$E_{yg}(iv)$
$\frac{1}{2}([\Delta_{\Gamma_u}]_{1\downarrow}^{1\uparrow} - [\Delta_{\Gamma_u}]_{2\downarrow}^{2\uparrow})$	Triplet, Intra	λ_3	Triplet	σ_z	B_{2g}
$\frac{-1}{4}([\Delta_{\Gamma_u}]_{1\uparrow}^{1\uparrow} - [\Delta_{\Gamma_u}]_{1\downarrow}^{1\downarrow} - [\Delta_{\Gamma_u}]_{2\uparrow}^{2\uparrow} + [\Delta_{\Gamma_u}]_{2\downarrow}^{2\downarrow})$	Triplet, Intra	λ_3	Triplet	σ_x	$E_{xg}(iv)$
$\frac{-i}{2}([\Delta_{\Gamma_u}]_{3\uparrow}^{1\uparrow} + [\Delta_{\Gamma_u}]_{3\downarrow}^{1\downarrow})$	Triplet	λ_4	Triplet	σ_y	Reducible
$\frac{1}{2}([\Delta_{\Gamma_u}]_{3\downarrow}^{1\uparrow} + [\Delta_{\Gamma_u}]_{3\uparrow}^{1\downarrow})$	Triplet	λ_4	Triplet	σ_z	$E_{yg}(v)$
$\frac{-1}{2}([\Delta_{\Gamma_u}]_{3\uparrow}^{1\uparrow} - [\Delta_{\Gamma_u}]_{3\downarrow}^{1\downarrow})$	Triplet	λ_4	Triplet	σ_x	Reducible
$\frac{-i}{2}([\Delta_{\Gamma_u}]_{3\uparrow}^{2\uparrow} + [\Delta_{\Gamma_u}]_{3\downarrow}^{2\downarrow})$	Triplet	λ_6	Triplet	σ_y	Reducible
$\frac{1}{2}([\Delta_{\Gamma_u}]_{3\downarrow}^{2\uparrow} + [\Delta_{\Gamma_u}]_{3\uparrow}^{2\downarrow})$	Triplet	λ_6	Triplet	σ_z	$E_{xg}(v)$
$\frac{-1}{2}([\Delta_{\Gamma_u}]_{3\uparrow}^{2\uparrow} - [\Delta_{\Gamma_u}]_{3\downarrow}^{2\downarrow})$	Triplet	λ_6	Triplet	σ_x	Reducible
$\frac{-i}{4\sqrt{3}}([\Delta_{\Gamma_u}]_{1\uparrow}^{1\uparrow} + [\Delta_{\Gamma_u}]_{1\downarrow}^{1\downarrow} + [\Delta_{\Gamma_u}]_{2\uparrow}^{2\uparrow} + [\Delta_{\Gamma_u}]_{2\downarrow}^{2\downarrow} - 2[\Delta_{\Gamma_u}]_{3\uparrow}^{3\uparrow} - 2[\Delta_{\Gamma_u}]_{3\downarrow}^{3\downarrow})$	Triplet, Intra	λ_8	Triplet	σ_y	$E_{yg}(vi)$
$\frac{1}{2\sqrt{3}}([\Delta_{\Gamma_u}]_{1\downarrow}^{1\uparrow} + [\Delta_{\Gamma_u}]_{2\downarrow}^{2\uparrow} - 2[\Delta_{\Gamma_u}]_{3\downarrow}^{3\uparrow})$	Triplet, Intra	λ_8	Triplet	σ_z	A_{2g}
$\frac{-1}{4\sqrt{3}}([\Delta_{\Gamma_u}]_{1\uparrow}^{1\uparrow} - [\Delta_{\Gamma_u}]_{1\downarrow}^{1\downarrow} + [\Delta_{\Gamma_u}]_{2\uparrow}^{2\uparrow} - [\Delta_{\Gamma_u}]_{2\downarrow}^{2\downarrow} - 2[\Delta_{\Gamma_u}]_{3\uparrow}^{3\uparrow} + 2[\Delta_{\Gamma_u}]_{3\downarrow}^{3\downarrow})$	Triplet, Intra	λ_8	Triplet	σ_x	$E_{xg}(vi)$

7.2 Superconducting order parameter in terms of the basis functions for the different neighbors

In this section, we present a detailed mathematical derivation to obtain the equation for the gap when different neighbors are included. For further neighbors, the rewriting in terms of the basis functions and the identification of the irreducible representation becomes more complex. A summary of the main results for the basis functions of the different neighbors is included in Tables 7.5, 7.6. In the next Chapter, the main results using this formalism will be presented.

7.2.1 Nearest neighbors

We consider first the case with only nearest neighbors interactions mediated through the spin-fluctuation mechanism. To simplify the expression of the gap equation it is very convenient to consider the symmetries encoded in the pairing interaction. We focus first on the nearest-neighbors, and notice that

$$\begin{aligned} [V_{(1,0)}]_{\tilde{\mu}_j, \tilde{\mu}_l}^{\tilde{\mu}_i, \tilde{\mu}_k} &= [V_{(-1,0)}]_{\tilde{\mu}_j, \tilde{\mu}_l}^{\tilde{\mu}_i, \tilde{\mu}_k} \equiv [V_x^{1N}]_{\tilde{\mu}_j, \tilde{\mu}_l}^{\tilde{\mu}_i, \tilde{\mu}_k}, \\ [V_{(0,1)}]_{\tilde{\mu}_j, \tilde{\mu}_l}^{\tilde{\mu}_i, \tilde{\mu}_k} &= [V_{(0,-1)}]_{\tilde{\mu}_j, \tilde{\mu}_l}^{\tilde{\mu}_i, \tilde{\mu}_k} \equiv [V_y^{1N}]_{\tilde{\mu}_j, \tilde{\mu}_l}^{\tilde{\mu}_i, \tilde{\mu}_k}. \end{aligned} \quad (7.13)$$

Hence, in this case, equation (7.9) for the gap is given by

$$\begin{aligned} [\Delta_{\mathbf{k}}^{1N}]_{\tilde{\mu}_j}^{\tilde{\mu}_i} &= \frac{1}{\mathcal{N}} \sum_{\mathbf{k}'} \sum_{\tilde{\mu}_k, \tilde{\mu}_l} \left\{ [V_x^{1N}]_{\tilde{\mu}_j, \tilde{\mu}_l}^{\tilde{\mu}_i, \tilde{\mu}_k} \left(e^{-i(k_x+k'_x)} + e^{i(k_x+k'_x)} \right) + [V_y^{1N}]_{\tilde{\mu}_j, \tilde{\mu}_l}^{\tilde{\mu}_i, \tilde{\mu}_k} \left(e^{-i(k_y+k'_y)} + e^{i(k_y+k'_y)} \right) \right. \\ &\quad \left. - [V_x^{1N}]_{\tilde{\mu}_j, \tilde{\mu}_k}^{\tilde{\mu}_i, \tilde{\mu}_l} \left(e^{-i(k_x-k'_x)} + e^{i(k_x-k'_x)} \right) - [V_y^{1N}]_{\tilde{\mu}_j, \tilde{\mu}_k}^{\tilde{\mu}_i, \tilde{\mu}_l} \left(e^{-i(k_y-k'_y)} + e^{i(k_y-k'_y)} \right) \right\} \langle \hat{c}_{-\mathbf{k}'\tilde{\mu}_l} \hat{c}_{\mathbf{k}'\tilde{\mu}_k} \rangle. \end{aligned} \quad (7.14)$$

This can be easily rewritten in terms of the cosine functions as

$$[\Delta_{\mathbf{k}}^{1N}]_{\tilde{\mu}_j}^{\tilde{\mu}_i} = \frac{1}{\mathcal{N}} \sum_{\mathbf{k}'} \sum_{\tilde{\mu}_k, \tilde{\mu}_l} \left\{ [V_x^{1N}]_{\tilde{\mu}_j, \tilde{\mu}_l}^{\tilde{\mu}_i, \tilde{\mu}_k} 2 \cos(k_x + k'_x) + [V_y^{1N}]_{\tilde{\mu}_j, \tilde{\mu}_l}^{\tilde{\mu}_i, \tilde{\mu}_k} 2 \cos(k_y + k'_y) \right. \quad (7.15)$$

$$\left. - [V_x^{1N}]_{\tilde{\mu}_j, \tilde{\mu}_k}^{\tilde{\mu}_i, \tilde{\mu}_l} 2 \cos(k_x - k'_x) - [V_y^{1N}]_{\tilde{\mu}_j, \tilde{\mu}_k}^{\tilde{\mu}_i, \tilde{\mu}_l} 2 \cos(k_y - k'_y) \right\} \langle \hat{c}_{-\mathbf{k}'\tilde{\mu}_l} \hat{c}_{\mathbf{k}'\tilde{\mu}_k} \rangle. \quad (7.16)$$

Similar to the previous Chapter, we want to project the interaction into the different form factors. With this purpose, we can expand the cosine functions, so that

$$\begin{aligned} [\Delta_{\mathbf{k}}^{1N}]_{\tilde{\mu}_j}^{\tilde{\mu}_i} &= \frac{1}{\mathcal{N}} \sum_{\mathbf{k}'} \sum_{\tilde{\mu}_k, \tilde{\mu}_l} \left\{ [V_x^{1N}]_{\tilde{\mu}_j, \tilde{\mu}_l}^{\tilde{\mu}_i, \tilde{\mu}_k} 2(\cos k_x \cos k'_x - \sin k_x \sin k'_x) \right. \\ &\quad + [V_y^{1N}]_{\tilde{\mu}_j, \tilde{\mu}_l}^{\tilde{\mu}_i, \tilde{\mu}_k} 2(\cos k_y \cos k'_y - \sin k_y \sin k'_y) \\ &\quad - [V_x^{1N}]_{\tilde{\mu}_j, \tilde{\mu}_k}^{\tilde{\mu}_i, \tilde{\mu}_l} 2(\cos k_x \cos k'_x + \sin k_x \sin k'_x) \\ &\quad \left. - [V_y^{1N}]_{\tilde{\mu}_j, \tilde{\mu}_k}^{\tilde{\mu}_i, \tilde{\mu}_l} 2(\cos k_y \cos k'_y - \sin k_y \sin k'_y) \right\} \langle \hat{c}_{-\mathbf{k}'\tilde{\mu}_l} \hat{c}_{\mathbf{k}'\tilde{\mu}_k} \rangle. \end{aligned} \quad (7.17)$$

Once we have this expression, with some algebra manipulation we can finally write it in terms of the different form factors for the first neighbors, corresponding to

$$\begin{aligned}
[\Delta_{\mathbf{k}}^{1N}]_{\tilde{\mu}_j}^{\tilde{\mu}_i} &= \frac{1}{\mathcal{N}} \sum_{\mathbf{k}'} \sum_{\tilde{\mu}_k, \tilde{\mu}_l} \langle \hat{c}_{-\mathbf{k}'\tilde{\mu}_l} \hat{c}_{\mathbf{k}'\tilde{\mu}_k} \rangle \left\{ -[i\sqrt{2} \sin k_y] \left[-i\sqrt{2} \left([V_y^{1N}]_{\tilde{\mu}_j, \tilde{\mu}_l}^{\tilde{\mu}_i, \tilde{\mu}_k} + [V_y^{1N}]_{\tilde{\mu}_j, \tilde{\mu}_k}^{\tilde{\mu}_i, \tilde{\mu}_l} \right) \sin k'_y \right] \right. \\
&\quad - [i\sqrt{2} \sin k_x] \left[-i\sqrt{2} \left([V_x^{1N}]_{\tilde{\mu}_j, \tilde{\mu}_l}^{\tilde{\mu}_i, \tilde{\mu}_k} + [V_x^{1N}]_{\tilde{\mu}_j, \tilde{\mu}_k}^{\tilde{\mu}_i, \tilde{\mu}_l} \right) \sin k'_x \right] \\
&\quad + [\cos k_x + \cos k_y] \left[\left([V_x^{1N}]_{\tilde{\mu}_j, \tilde{\mu}_l}^{\tilde{\mu}_i, \tilde{\mu}_k} - [V_x^{1N}]_{\tilde{\mu}_j, \tilde{\mu}_k}^{\tilde{\mu}_i, \tilde{\mu}_l} \right) \cos k'_x + \left([V_y^{1N}]_{\tilde{\mu}_j, \tilde{\mu}_l}^{\tilde{\mu}_i, \tilde{\mu}_k} - [V_y^{1N}]_{\tilde{\mu}_j, \tilde{\mu}_k}^{\tilde{\mu}_i, \tilde{\mu}_l} \right) \cos k'_y \right] \\
&\quad \left. + [\cos k_x - \cos k_y] \left[\left([V_x^{1N}]_{\tilde{\mu}_j, \tilde{\mu}_l}^{\tilde{\mu}_i, \tilde{\mu}_k} - [V_x^{1N}]_{\tilde{\mu}_j, \tilde{\mu}_k}^{\tilde{\mu}_i, \tilde{\mu}_l} \right) \cos k'_x - \left([V_y^{1N}]_{\tilde{\mu}_j, \tilde{\mu}_l}^{\tilde{\mu}_i, \tilde{\mu}_k} - [V_y^{1N}]_{\tilde{\mu}_j, \tilde{\mu}_k}^{\tilde{\mu}_i, \tilde{\mu}_l} \right) \cos k'_y \right] \right\}. \tag{7.18}
\end{aligned}$$

From this equation, we can identify that we have two even and two odd form factors, corresponding in the first case to the irreducible representations A_{1g} , B_{1g} , whereas the odd basis functions correspond to the two-dimensional odd irreducible representation of D_{4h} . This results are summarized in Table 7.5. Using the same notation as in equation (6.8), the matrix for the order parameter in \mathbf{k} -space reads

$$\hat{\Delta}_{\mathbf{k}} = g_{\mathbf{k}}^{A_{1g}, 1N} \hat{\Delta}_{A_{1g}}^{1N} + g_{\mathbf{k}}^{B_{1g}, 1N} \hat{\Delta}_{B_{1g}}^{1N} - g_{\mathbf{k}}^{E_{xu}, 1N} \hat{\Delta}_{E_{xu}}^{1N} - g_{\mathbf{k}}^{E_{yu}, 1N} \hat{\Delta}_{E_{yu}}^{1N}, \tag{7.19}$$

where each 6×6 matrix can be written using the Bogoliubov transformation:

$$\begin{aligned}
[\Delta_{A_{1g}}^{1N}]_{\tilde{\mu}_j}^{\tilde{\mu}_i} &= -\frac{1}{\mathcal{N}} \sum_{\mathbf{k}'} \sum_{\tilde{\mu}_k, \tilde{\mu}_l} \left[\left([V_x^{1N}]_{\tilde{\mu}_j, \tilde{\mu}_l}^{\tilde{\mu}_i, \tilde{\mu}_k} - [V_x^{1N}]_{\tilde{\mu}_j, \tilde{\mu}_k}^{\tilde{\mu}_i, \tilde{\mu}_l} \right) \cos k'_x + \left([V_y^{1N}]_{\tilde{\mu}_j, \tilde{\mu}_l}^{\tilde{\mu}_i, \tilde{\mu}_k} - [V_y^{1N}]_{\tilde{\mu}_j, \tilde{\mu}_k}^{\tilde{\mu}_i, \tilde{\mu}_l} \right) \cos k'_y \right] \\
&\quad \times \sum_n u_{\mathbf{k}'\tilde{\mu}_k}^n v_{-\mathbf{k}'\tilde{\mu}_l}^{n*} \tanh\left(\frac{\beta E_{\mathbf{k}'n}}{2}\right), \\
[\Delta_{B_{1g}}^{1N}]_{\tilde{\mu}_j}^{\tilde{\mu}_i} &= -\frac{1}{\mathcal{N}} \sum_{\mathbf{k}'} \sum_{\tilde{\mu}_k, \tilde{\mu}_l} \left[\left([V_x^{1N}]_{\tilde{\mu}_j, \tilde{\mu}_l}^{\tilde{\mu}_i, \tilde{\mu}_k} - [V_x^{1N}]_{\tilde{\mu}_j, \tilde{\mu}_k}^{\tilde{\mu}_i, \tilde{\mu}_l} \right) \cos k'_x - \left([V_y^{1N}]_{\tilde{\mu}_j, \tilde{\mu}_l}^{\tilde{\mu}_i, \tilde{\mu}_k} - [V_y^{1N}]_{\tilde{\mu}_j, \tilde{\mu}_k}^{\tilde{\mu}_i, \tilde{\mu}_l} \right) \cos k'_y \right] \\
&\quad \times \sum_n u_{\mathbf{k}'\tilde{\mu}_k}^n v_{-\mathbf{k}'\tilde{\mu}_l}^{n*} \tanh\left(\frac{\beta E_{\mathbf{k}'n}}{2}\right), \\
[\Delta_{E_{xu}}^{1N}]_{\tilde{\mu}_j}^{\tilde{\mu}_i} &= -\frac{1}{\mathcal{N}} \sum_{\mathbf{k}'} \sum_{\tilde{\mu}_k, \tilde{\mu}_l} \left[-i\sqrt{2} \left([V_x^{1N}]_{\tilde{\mu}_j, \tilde{\mu}_l}^{\tilde{\mu}_i, \tilde{\mu}_k} + [V_x^{1N}]_{\tilde{\mu}_j, \tilde{\mu}_k}^{\tilde{\mu}_i, \tilde{\mu}_l} \right) \sin k'_x \right] \sum_n u_{\mathbf{k}'\tilde{\mu}_k}^n v_{-\mathbf{k}'\tilde{\mu}_l}^{n*} \tanh\left(\frac{\beta E_{\mathbf{k}'n}}{2}\right), \\
[\Delta_{E_{yu}}^{1N}]_{\tilde{\mu}_j}^{\tilde{\mu}_i} &= -\frac{1}{\mathcal{N}} \sum_{\mathbf{k}'} \sum_{\tilde{\mu}_k, \tilde{\mu}_l} \left[-i\sqrt{2} \left([V_y^{1N}]_{\tilde{\mu}_j, \tilde{\mu}_l}^{\tilde{\mu}_i, \tilde{\mu}_k} + [V_y^{1N}]_{\tilde{\mu}_j, \tilde{\mu}_k}^{\tilde{\mu}_i, \tilde{\mu}_l} \right) \sin k'_y \right] \sum_n u_{\mathbf{k}'\tilde{\mu}_k}^n v_{-\mathbf{k}'\tilde{\mu}_l}^{n*} \tanh\left(\frac{\beta E_{\mathbf{k}'n}}{2}\right). \tag{7.20}
\end{aligned}$$

7.2.2 Further neighbors

Following the same procedure, we can derive the equation for the gap for up to sixth neighbors, so that 28 neighbors in total are added. The derivation in these cases is shown in Appendix E, where we also derive the inclusion of the on-site interactions, which should contain the bare interactions and the ones arising from the spin-fluctuation mechanism. In Tables 7.5, 7.6, we summarize the representative basis functions found for all neighbors.

Table 7.5: Representative basis functions for each irreducible representation indicating the neighbor that they correspond to, including from first to third neighbors.

IR	Representative basis functions		
	1st neighbors	2nd neighbors	3rd neighbors
A_{1g}	$\cos k_x + \cos k_y$	$2 \cos k_x \cos k_y$	$\cos 2k_x + \cos 2k_y$
A_{2g}	-	-	-
B_{1g}	$\cos k_x - \cos k_y$	-	$\cos 2k_x - \cos 2k_y$
B_{2g}	-	$2 \sin k_x \sin k_y$	-
E_{xu}	$i\sqrt{2} \sin k_x$	$2i \sin k_x \cos k_y$	$i\sqrt{2} \sin 2k_x$
E_{yu}	$i\sqrt{2} \sin k_y$	$2i \sin k_y \cos k_x$	$i\sqrt{2} \sin 2k_y$

Table 7.6: Representative basis functions for each irreducible representation indicating the neighbor that they correspond to, including from fourth to sixth neighbors.

IR	Representative basis functions		
	4th neighbors	5th neighbors	6th neighbors
A_{1g}	$\sqrt{2} \cos 2k_x \cos k_y + \sqrt{2} \cos k_x \cos 2k_y$	$2 \cos 2k_x \cos 2k_y$	$\cos 3k_x + \cos 3k_y$
A_{2g}	$\sqrt{2} \sin 2k_x \sin k_y - \sqrt{2} \sin k_x \sin 2k_y$	-	-
B_{1g}	$\sqrt{2} \cos 2k_x \cos k_y - \sqrt{2} \cos k_x \cos 2k_y$	-	$\cos 3k_x - \cos 3k_y$
B_{2g}	$\sqrt{2} \sin 2k_x \sin k_y + \sqrt{2} \sin k_x \sin 2k_y$	$2 \sin 2k_x \sin 2k_y$	-
E_{xu}	$2i \sin k_x \cos 2k_y, 2i \sin 2k_x \cos k_y$	$2i \sin 2k_x \cos 2k_y$	$i\sqrt{2} \sin 3k_x$
E_{yu}	$2i \sin k_y \cos 2k_x, 2i \sin 2k_y \cos k_x$	$2i \sin 2k_y \cos 2k_x$	$i\sqrt{2} \sin 3k_y$

The final expression for the superconducting order parameter including up to sixth neighbors and on-site interactions introduced in the program is given by

$$\begin{aligned}
\hat{\Delta}_{\mathbf{k}} = & \hat{\Delta}_{A_{1g}}^{\text{On-site}} + (\cos k_x + \cos k_y) \hat{\Delta}_{A_{1g}}^{1N} + (\cos k_x - \cos k_y) \hat{\Delta}_{B_{1g}}^{1N} - i\sqrt{2} \sin k_x \hat{\Delta}_{E_{xu}}^{1N} - i\sqrt{2} \sin k_x \hat{\Delta}_{E_{yu}}^{1N} \\
& + (2 \cos k_x \cos k_y) \hat{\Delta}_{A_{1g}}^{2N} + (2 \sin k_x \sin k_y) \hat{\Delta}_{B_{2g}}^{2N} - 2i \sin k_x \cos k_y \hat{\Delta}_{E_{xu}}^{2N} - 2i \sin k_y \cos k_x \hat{\Delta}_{E_{yu}}^{2N} \\
& + (\cos 2k_x + \cos 2k_y) \hat{\Delta}_{A_{1g}}^{3N} + (\cos 2k_x - \cos 2k_y) \hat{\Delta}_{B_{1g}}^{3N} - i\sqrt{2} \sin 2k_x \hat{\Delta}_{E_{xu}}^{3N} - i\sqrt{2} \sin 2k_x \hat{\Delta}_{E_{yu}}^{3N} \\
& + \sqrt{2}(\cos 2k_x \cos k_y + \cos k_x \cos 2k_y) \hat{\Delta}_{A_{1g}}^{4N} + \sqrt{2}(\cos 2k_x \cos k_y + \cos k_x \cos 2k_y) \hat{\Delta}_{B_{1g}}^{4N} \\
& + \sqrt{2}(\sin 2k_x \sin k_y + \sin k_x \sin 2k_y) \hat{\Delta}_{B_{2g}}^{4N} + \sqrt{2}(\sin 2k_x \sin k_y - \sin k_x \sin 2k_y) \hat{\Delta}_{A_{2g}}^{4N} \\
& - 2i \sin k_x \cos 2k_y \hat{\Delta}_{E_{xu},1}^{4N} - 2i \sin k_y \cos 2k_x \hat{\Delta}_{E_{yu},1}^{4N} - 2i \sin 2k_x \cos k_y \hat{\Delta}_{E_{xu},2}^{4N} \\
& - 2i \sin 2k_y \cos k_x \hat{\Delta}_{E_{yu},2}^{4N} + (2 \cos 2k_x \cos 2k_y) \hat{\Delta}_{A_{1g}}^{5N} + (2 \sin 2k_x \sin 2k_y) \hat{\Delta}_{B_{2g}}^{5N} \\
& - 2i \sin 2k_x \cos 2k_y \hat{\Delta}_{E_{xu}}^{5N} - 2i \sin 2k_y \cos 2k_x \hat{\Delta}_{E_{yu}}^{5N} + (\cos 3k_x + \cos 3k_y) \hat{\Delta}_{A_{1g}}^{6N} \\
& + (\cos 3k_x - \cos 3k_y) \hat{\Delta}_{B_{1g}}^{6N} - i\sqrt{2} \sin 3k_x \hat{\Delta}_{E_{xu}}^{6N} - i\sqrt{2} \sin 3k_x \hat{\Delta}_{E_{yu}}^{6N},
\end{aligned} \tag{7.21}$$

where each Δ_{Γ}^{mN} is a 6×6 matrix, and m denotes the neighbors. In Figure 8.1, an example for the obtained first neighbors matrices $\Delta_{A_{1g}}^{1N}$ and $\Delta_{B_{1g}}^{1N}$ is shown.

7.3 Entropy and specific heat

To study the phase transitions that can appear between the different superconducting states, it is convenient to calculate two very important physical quantities, the entropy and the specific heat. The entropy per unit volume of a superconductor is given in terms of the Bogoliubov quasiparticle spectrum by

$$S(T) = -\frac{2k_B}{\mathcal{N}} \sum_{\mathbf{k},n} \{f(E_{\mathbf{k}n}) \ln[f(E_{\mathbf{k}n})] + (1 - f(E_{\mathbf{k}n})) \ln[1 - f(E_{\mathbf{k}n})]\}, \tag{7.22}$$

where again $f(E_{\mathbf{k}n})$ is the Fermi distribution function. From the result for the entropy at each temperature, we can calculate the specific heat by performing a numerical derivative,

$$C_e(T) = T \left(\frac{\partial S}{\partial T} \right). \tag{7.23}$$

Since we are considering that superconductivity is originated from a spin-fluctuation mechanism, we will obtain the electronic specific heat. Notice that since we are considering $k_B = 1$, the entropy and the specific heat are dimensionless in our units.

Since it will be convenient later on for comparisons, the entropy and the specific heat have been calculated using the self-consistent code in the normal-state. The result obtained for the specific heat is shown in Figure 7.2, where it can be seen that in the normal state it corresponds to a straight line, as expected for a metal at low temperatures. The same behaviour is observed in the case of the entropy.

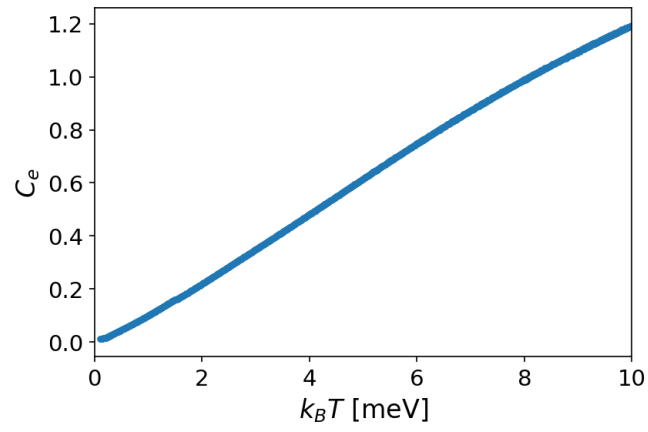


Figure 7.2: Specific heat as a function of temperature in the normal state with $N = 51$.

Chapter 8

Results from spin-fluctuation mediated pairing

8.1 Results for the different neighbors

In this Chapter, we show the results in the process of constructing the full picture of 28 neighbors and on-site interactions. In the first results presented, on-site interactions are not included, since in the case of longer range neighbors it is easier for the code to overcome the repulsive interaction and converge. To begin with, only the inclusion of first neighbors will be considered to understand the different channels obtained. In the next intermediate step, we will add up to third neighbors. Finally, up to sixth neighbors with on-site interactions are included.

Since it will become important in the results shown, we need to explain how the labeling of the different channels is presented. The first label will always correspond to the form factor irreducible representation, including the range of the interaction. Secondly, we will detail the orbital and spin information. The matrices coupling to an odd form factor are always suppressed in the cases considered in this thesis. Thus, we will include the irreducible representations according to Tables 7.1, 7.2 and the particular spin character, noticing that the orbital character is implicit once the previous information is provided, since the total gap must be antisymmetric under the exchange of two electrons.

8.1.1 Numerical implementation

We detail how the pairing interactions and the different neighbors have been implemented in the code, since major modifications were needed. The self-consistent solution is obtained in the same way as in the first part of the thesis, setting a precision for both the order parameter components and the electron density for the code to converge, which is always set to 0.001 meV. On the contrary, from the pairing interactions, 36 matrices 6×6 are generated encoding all orbital and spin combinations.

The order parameter matrix is initialized as containing m 6×6 matrices, where m is the total number of odd and even irreducible representations included, which will depend on the number of neighbors considered (see Tables 7.5, 7.6). For instance, when 6 neighbors and on-site interactions are included we will have 29 matrices. Once the code has converged, to obtain the orbital and spin information, the Tables 7.1, 7.2, 7.4 and 7.3 are generated for each matrix.

8.1.2 Inclusion of first neighbors

As a first step, we include only the interactions of the first neighbors. To understand the results obtained from the code, it is interesting to visualize first the order parameter matrices, so that we can see the leading orbital and spin contributions. With this objective, we can plot the 6×6 matrices for the case of $J = 12$ meV, as shown in Figure 8.1. We can see the form of the matrices coupling to $\cos k_x + \cos k_y$ (A_{1g}) and $\cos k_x - \cos k_y$ (B_{1g}), remembering that non-zero values for the order parameter components only arise in the matrices coupling to an even form factor, and the matrices coupling to an odd form factor are completely suppressed.

Nevertheless, when the program is run several times for the same initial values, only the absolute values of the order parameters are preserved, due to the freedom to choose a gauge. To make the results reproducible in terms of real and imaginary parts, we take the element with the largest absolute value comparing the four matrices,

$$\text{Abs}_{\max} = \max \left\{ \left| [\Delta_{A_{1g}}]_{\tilde{\mu}_i, \tilde{\mu}_j}^{\tilde{\mu}_i} \right|, \left| [\Delta_{B_{1g}}]_{\tilde{\mu}_i, \tilde{\mu}_j}^{\tilde{\mu}_i} \right|, \left| [\Delta_{E_{xu}}]_{\tilde{\mu}_i, \tilde{\mu}_j}^{\tilde{\mu}_i} \right|, \left| [\Delta_{E_{yu}}]_{\tilde{\mu}_i, \tilde{\mu}_j}^{\tilde{\mu}_i} \right| \right\}, \quad (8.1)$$

with a corresponding real part Re_{\max} and imaginary part Im_{\max} . Then, we choose the gauge as

$$\theta = \arctan \left(\frac{\text{Im}_{\max}}{\text{Re}_{\max}} \right), \quad (8.2)$$

and we can multiply all mean fields by this gauge,

$$[\Delta_{\Gamma}]_{\tilde{\mu}_i, \tilde{\mu}_j}^{\tilde{\mu}_i} = e^{-i\theta} [\Delta_{\Gamma}]_{\tilde{\mu}_i, \tilde{\mu}_j}^{\tilde{\mu}_i}. \quad (8.3)$$

This choice is convenient since, as can be seen in Figure 8.1, we are able to decouple the real and the imaginary part of both matrices.

For the B_{1g} matrix (Figure 8.1f), we can see that the major contributions originate from the intraorbital interaction with opposite spin, $\{xy \uparrow, xy \downarrow\}$. This contrasts with the A_{1g} matrix, where the bigger order parameter components appear in the interorbital components with the same spin: $\{xy \uparrow, xz \uparrow\}$, $\{xy \uparrow, yz \uparrow\}$, $\{xy \downarrow, xz \downarrow\}$, and $\{xy \downarrow, yz \downarrow\}$.

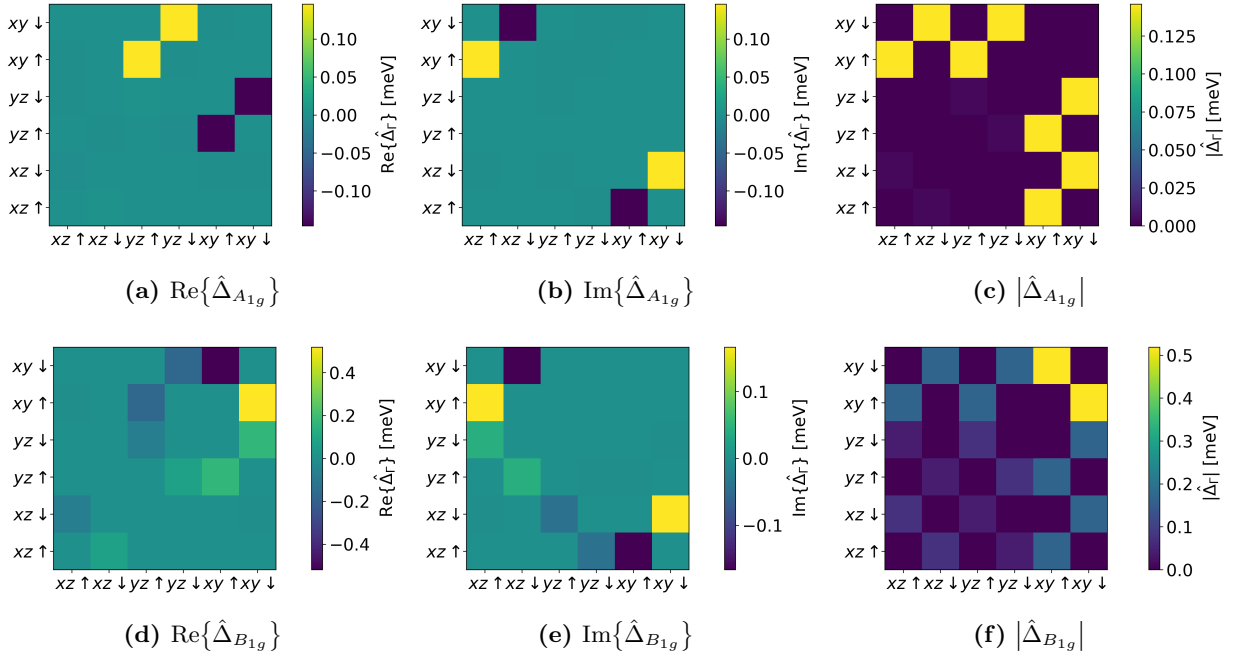


Figure 8.1: Non-zero superconducting order parameter matrices Δ_{1g}^{1N} , Δ_{B1g}^{1N} coupling to the A_{1g} and B_{1g} form factors, according to equation (7.21). Only nearest neighbors are included, and the parameters chosen are $N = 31$, $\lambda_{\text{SOC}} = 35$ meV, $k_B T = 0.01$ meV, $J = 12$ meV and a boost $\alpha = 3$. The matrices coupling to an odd form factor are completely suppressed.

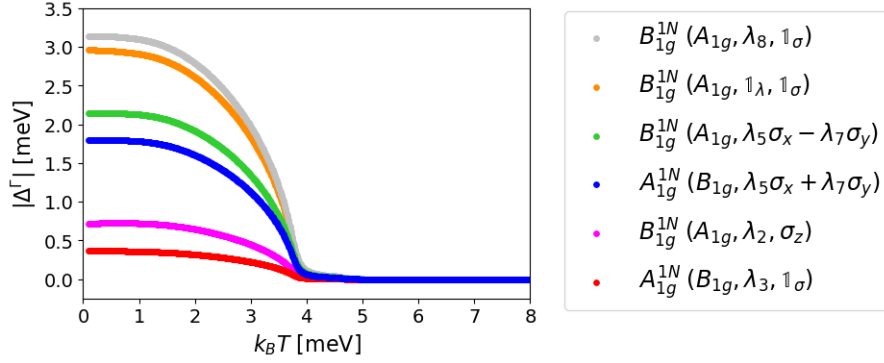
At this point, the previous analysis regarding the internal structure (orbital and spin) for a matrix coupling to an even form factor must be recalled. Figure 8.2a shows the different irreducible representations obtained from the combinations in Tables 7.1, 7.2 in the case $J = 12$ meV. Importantly, we should remark that in the labeling of the figure the first IR corresponds to the form factor, and in parenthesis it is detailed the IR in spin and orbital space and how it couples to these spaces. The leading solutions correspond to spin singlets, since they couple to $\mathbb{1}_\sigma$, whereas the spin-triplet solutions, the ones coupling to the Pauli matrices $\{\sigma_x, \sigma_y, \sigma_z\}$, are subleading. Moreover, in agreement with the previous Figure 8.1, the dominant channels originate from the order parameter components coupling to the B_{1g} matrix.

Remarkably, all channels have the same transition temperature to the normal state. In this way, we cannot forget that for a complete description of the order parameter we should give an overall label including the form factors IR and the spin/orbital IR, which would result in the product of representations. Recalling the product tables for IRs in the point group D_{4h} , in all channels shown the overall IR would be B_{1g} , which could explain why a single transition temperature is observed.

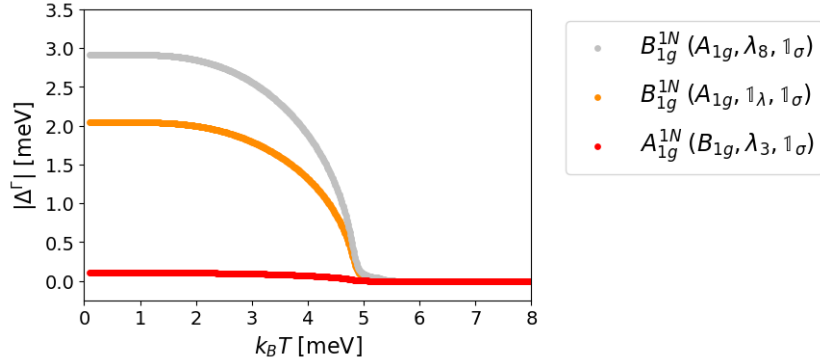
To further understand the information given after combining orbital and spin space, it is convenient to compare with the case of zero spin-orbit coupling. The results for the different

channels in this case can be seen in Figure 8.2b, where we introduce a small hybridization in the band parametrization between xz and yz orbitals. As expected, in the case of zero spin-orbit coupling there should not be coexistence between the singlet and triplet channels. Therefore, only the singlet channels emerge as possible solutions, and the triplet channels are completely suppressed. This behaviour is also found in the cases of $J = \{0, 24, 36\}$ meV.

From now on, since the inclusion of all the channels can be a bit overwhelming, only the dominant symmetry with spin singlet and spin triplet will be shown. For instance, since both channels in Table 7.1 coupling to $\mathbf{1}_\lambda, \mathbf{1}_\sigma$ and $\lambda_8, \mathbf{1}_\sigma$ correspond to the A_{1g} irreducible representation with orbital triplet and spin singlet, only the dominant one will be plotted.



(a) $\lambda_{\text{SOC}} = 35$ meV, $g = 0$ meV



(b) $\lambda_{\text{SOC}} = 0$ meV, $g = 4.4$ meV

Figure 8.2: Non-zero superconducting order parameter channels according to Tables 7.1, 7.2 as a function of temperature for nearest-neighbors interactions. The odd-parity solutions are suppressed. We consider $N = 31$, $J = 12$ meV in both cases, and a) a boost $\alpha = 3$, $\lambda_{\text{SOC}} = 35$ meV, $g = 0$ meV, whereas in b) $\alpha = 2$, $\lambda_{\text{SOC}} = 0$ meV, $g = 4.4$ meV. The first label in the legend corresponds to the basis function IR specifying the range of the interaction, and inside the parentheses it is included the IR in orbital and spin space, detailing how each combination couples to orbital (λ) and spin space (σ).

8.1.3 Inclusion of up to third neighbors

The next step has been to add second neighbors. However, their contribution is small compared to the first neighbors, and thus they do not change the previous classification significantly. Consequently, we proceeded to the case in which up to third neighbors are included.

Similar to the previous case, we consider first an example for the form of the matrices after convergence, as shown in Figure 8.3. In agreement with Table 7.5, since the matrices coupling to an odd form factor are suppressed and there are 8 even form factors, we have 8 order parameter matrices. At first sight, it can be noted that the components belonging to the B_{2g} matrix are completely suppressed when solving self-consistently for the order parameter. Furthermore, the third neighbors have the most important role, since they show the largest mean-field values, despite the fact that the specific orbital and spin components for a certain IR are similar for all neighbors.

Following the same procedure, we can study in detail the dominant channels when considering the spin and orbital character of the different superconducting order parameter matrices. As we can see in Figure 8.4, in agreement with the previous matrix forms, the dominant contributions correspond to the third neighbors with the form factors $\cos 2k_x + \cos 2k_y$ (A_{1g}^{3N}) and $\cos 2k_x - \cos 2k_y$ (B_{1g}^{3N}). In the case $J = 12$ meV, the contributions of both components is similar at all

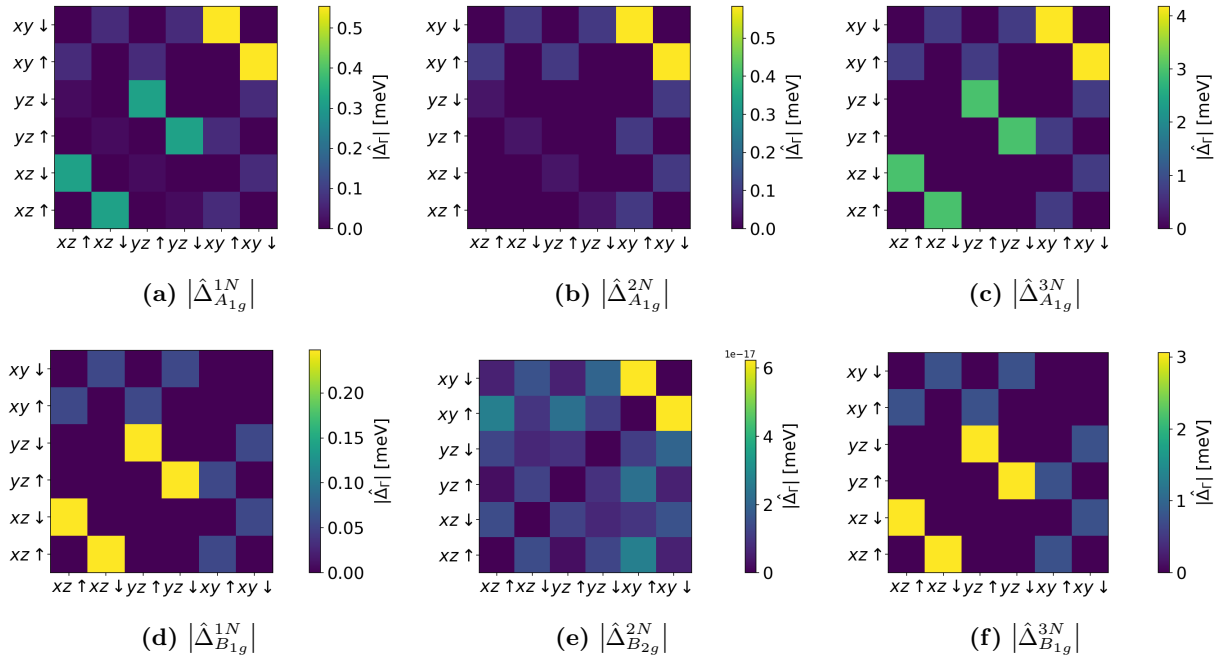


Figure 8.3: Superconducting order parameter matrices coupling to the even form factors including up to third neighbors with $N = 31$, $\lambda_{\text{SOC}} = 35$ meV, $k_B T = 0.01$ meV, $J = 12$ meV and a boost $\alpha = 2$. The components of the matrices coupling to an odd form factor are completely suppressed.

temperatures. This contrasts with the results for the larger $J = 24$ meV, where we can see a larger difference between the leading and sub-leading irreducible representation.

In both cases, the dominant contributions arise from the spin-singlet combinations. As previously discussed, due to the effect of a large spin-orbit coupling, the possibility of a mixed state with both spin characters is possible. This is indeed what we observe in Figure 8.4, since a non-zero spin triplet contribution is also present. Nevertheless, there appears to be a difference in the mixture between both characters depending on the Hund's coupling J . We will address this issue again when longer range neighbors are included.

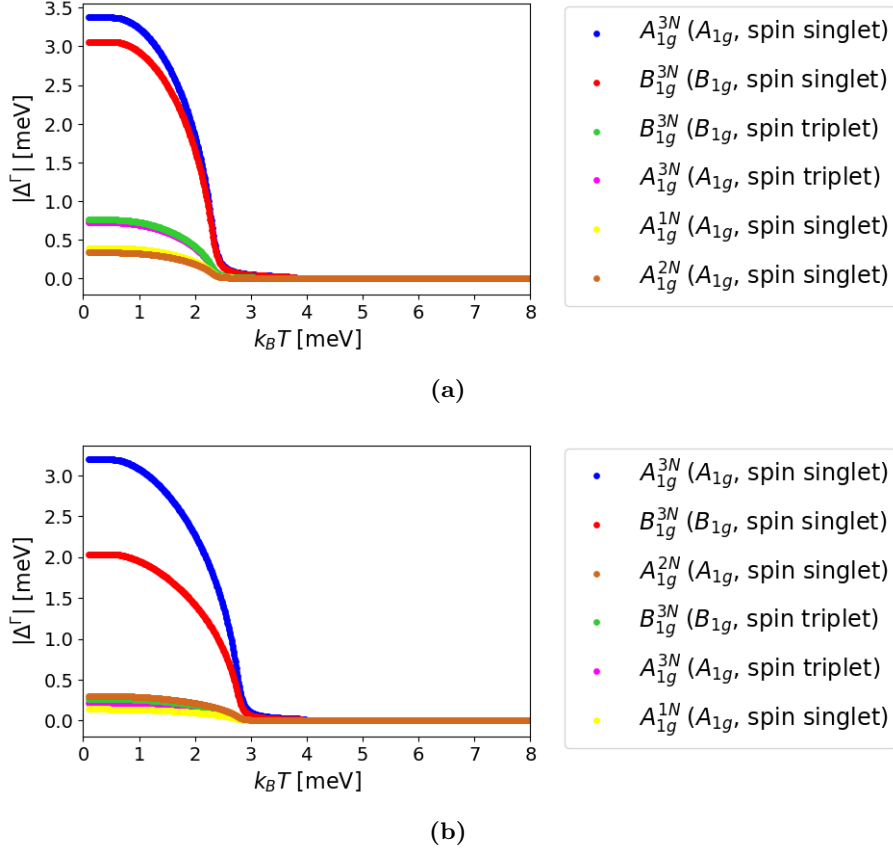


Figure 8.4: Leading superconducting order parameter channels according to Table 7.1 as a function of temperature, including up to third neighbors. The odd-parity solutions are suppressed. We consider $N = 31$ and $\lambda_{\text{SOC}} = 35$ meV in both cases. In a) we take a boost $\alpha = 2$ and $J = 12$ meV, whereas in b) $\alpha = 1.5$ and $J = 24$ meV. The first label in the legend corresponds to the basis function IR specifying the range of the interaction, and inside the parenthesis it is included the IR in orbital and spin space, detailing the spin character. Other channels with a smaller gap are also present, but they all have the same transition temperature.

8.1.4 Inclusion of up to sixth neighbors with on-site interactions

Ideally, we will have included enough neighbors in the model when no remarkable differences are seen by including further interactions. Therefore, since the spin-fluctuation mechanism seems to lead to stronger interactions in the neighbors located in the x and y direction (see Figure 7.1), up to sixth neighbors have been included. The contributions of the fourth, fifth and sixth neighbors is smaller in comparison to the third ones, and hence we can consider that the picture including 28 neighbors will provide reliable results. With this purpose, also the on-site interactions must be included, since the strong repulsion will affect the outcome. Furthermore, we are also seeking agreement with STM experiments (Figure 2.7), introduced in Chapter 2. Consequently, since the gap reported is of the order of a few meV, the boost applied to the spin-fluctuations and to the bare interactions will be adjusted to stabilize mean fields of this order.

The results for the order parameter irreducible representations as a function of temperature can be seen in Figure 8.5 for the four different values of the Hund's coupling. Only the dominant irreducible representations and their corresponding spin-singlet and spin-triplet contributions are shown. Note that also in this case all the odd-parity channels are suppressed. At first sight, it must be highlighted that the leading channels originate from the contributions of the third neighbors, although other neighbors also have smaller contributions with the same transition temperature. Remarkably, also the on-site order parameter matrix has non-zero values in all cases studied, although it is not leading. Considering spin and orbital decomposition (Table 7.1), the on-site order parameter is only non-zero in the singlet channel.

Two important features become apparent when comparing the four J values plotted. Firstly, we observe that the mixture between spin-singlet and spin-triplet character seems to be different. In the case $J = 0$ meV, both solutions are extremely mixed, and at the lowest temperature the values of the order parameter are close in energy. Nonetheless, as J is increased, the coexistence is suppressed, until the case of $J = 36$ meV, where the singlet character dominates the superconducting phase. Therefore, spin-orbit coupling seems to have a larger effect for a smaller Hund's coupling. Secondly, we can focus on the leading IR. Although in all cases the dominant IR in momentum space corresponds to an A_{1g} , for the smallest Hund's coupling it is very close in energy with the B_{1g} solution. However, when J is increased the latter is reduced.

As stated in a previous section, all channels seem to have the same transition temperature. This could be a consequence of the fact that, considering the global transformation including both momentum and orbital/spin spaces, all channels transform as an A_{1g} IR.

Moreover, the dependence on the system partitions has also been studied. The results for systems 31×31 up to 181×181 in steps of 10 have been compared for the same value of J , temperature, spin-orbit coupling and boost. As previously mentioned, since we aim to stabilize values for the gap of the order of a few meV in agreement with STM experiments, we require larger N . It has been verified that from systems with $N = 81$ up to $N = 181$ no major differences are observed in the results.

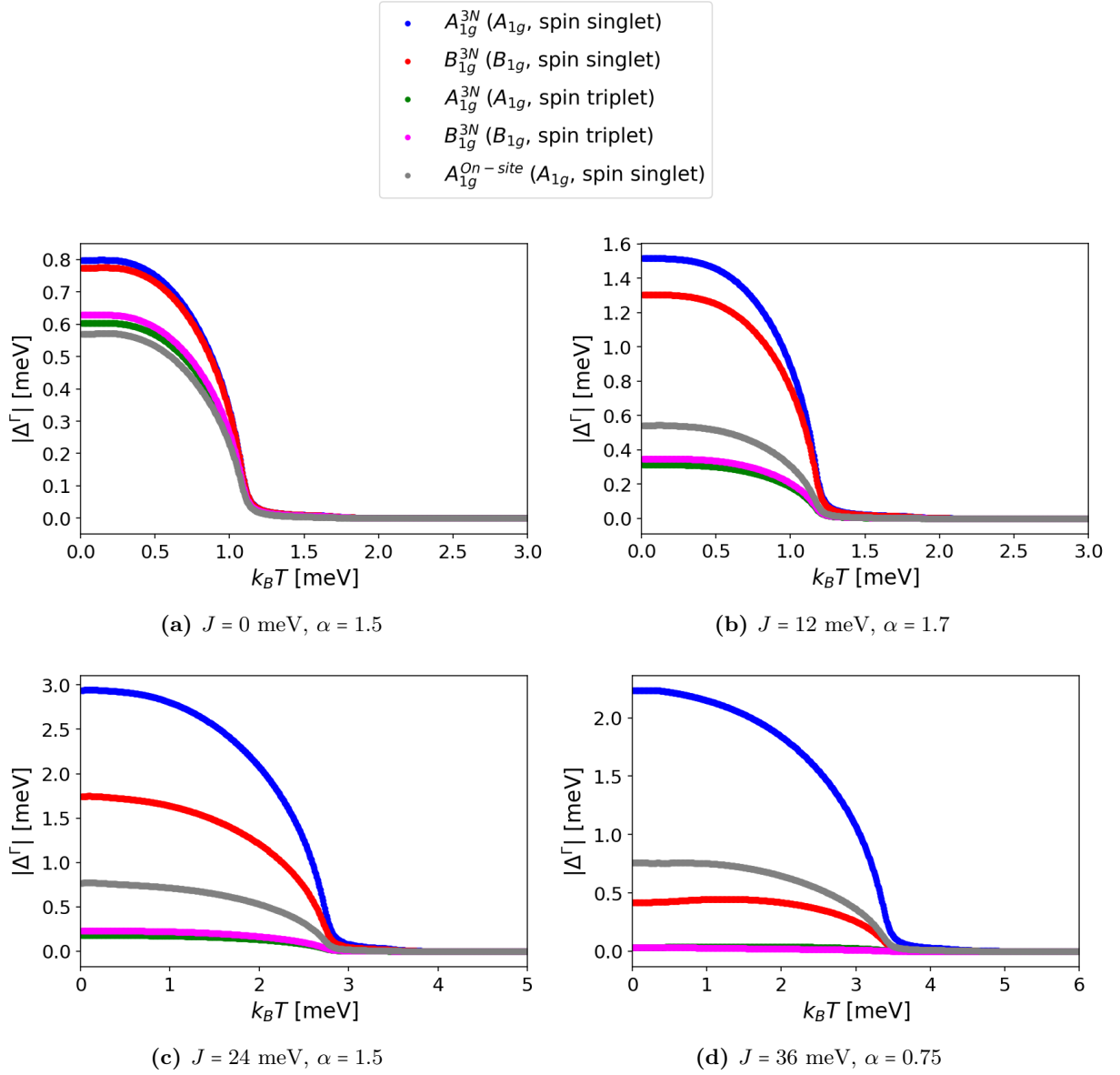


Figure 8.5: Leading superconducting order parameter channels according to Table 7.1 as a function of temperature, including up to sixth neighbors and on-site interaction. The odd-parity solutions are suppressed in all cases. We consider $N = 81$ and $\lambda_{\text{SOC}} = 35$ meV in all plots, whereas the J value and the boost (α) are different, as specified in each caption. The first label in the legend corresponds to the basis function IR specifying the range of the interaction, and inside the parenthesis it is included the IR in orbital and spin space, detailing the spin character. Other channels with a smaller gap are also present, but they all have the same transition temperature.

8.2 Comparison with the linearized gap equation

In this section, we want to confirm the reliability of the results obtained self-consistently by comparing close to the critical temperature with the linearized gap equation outcomes shown in Figure 3.2. Prior to this, it is necessary to compare the different notations used to identify the results. Similarly to Ref. [43], we use the following notation to refer to the irreducible representations of the D_{4h} group:

- s' : A_{1g} in D_{4h} ;
- $g_{xy(x^2-y^2)}$: A_{2g} in D_{4h} ;
- $d_{x^2-y^2}$: B_{1g} in D_{4h} ;
- d_{xy} : B_{2g} in D_{4h} ;
- *helical*: one-component odd-parity solutions of D_{4h} ;
- *chiral*: two-component E_u solution in D_{4h} .

In addition, the linearized gap equation solutions provide information on the dominant solution projected into the forms factor, and does not contain the information in orbital/spin space. Therefore, we should compare only focusing on the first label of the figures, which indicates the IR transformation in momentum space.

Apparently, there seems to be no agreement since, using the previous notation, when solving self-consistently the BdG equation the s' solution is the leading one for all Hund's coupling (Figure 8.5). Furthermore, in the larger J regimes, the helical solution dominates the diagram in the linearized gap equation, but the odd-parity solutions are completely suppressed in the self-consistent solution.

Several approaches have been followed to understand this result. In this way, even further neighbors have been included in the picture, concretely up to the tenth neighbors only in the x and y direction, since the basis functions are simple and correspond to higher harmonics of the first neighbors. Additionally, larger system sizes have been studied, up to 200×200 , but still no odd parity solutions were captured.

Finally, to establish a comparison of the same system, the picture from the linearized gap equation has been truncated to include only the 28 neighbors and on-site interactions, instead of the full picture used to derive Figure 3.2. In this case, an overall agreement is obtained close to the critical temperature, since using both methods the leading solution is the s' state for all J values. In the smaller J cases, the subleading solution is the $d_{x^2-y^2}$, in agreement with the results found self-consistently, where the B_{1g} appears close in energy to the A_{1g} IR. Remarkably, in the larger Hund's coupling regime the helical state appears to be the subleading solution. Therefore, this would explain why we are not able to capture the odd-parity solutions in the full self-consistent solution.

8.3 Effect of spin-orbit coupling

As a natural next step, we want to emphasise and study the effect of the spin-orbit coupling, and how it leads to the differences in the mixture of spin-singlet and spin-triplet character. With this purpose, only the cases of $J = 0$ meV and $J = 12$ meV are considered, since, according to Figure 8.5, for those values the mixture is larger. The results obtained can be seen in Figure 8.6.

Surprisingly, a smaller value for the spin-orbit coupling changes completely the previous picture with $\lambda_{\text{SOC}} = 35$ meV (Figure 8.5). For both Hund's values considered, the dominant order parameter channels arise from the first neighbors, in particular from the matrix coupling to the form factor $\cos k_x - \cos k_y$, corresponding to the B_{1g} IR. Also in contrast with the previous results, the A_{1g} IR is subleading, corresponding to the form factor $\cos k_x + \cos k_y$, and for the case $J = 0$ meV it is almost suppressed. In addition, if we define a global transformation including both momentum and orbital/spin space, all channels would transform as an A_{1g} IR. Finally, as shown in Figure 8.6, the on-site matrix elements are almost negligible, also in contraposition with the results for $\lambda_{\text{SOC}} = 35$ meV.

Nevertheless, the results obtained accomplish the initial purpose of this study, since in the case where spin-orbit coupling is almost suppressed ($\lambda_{\text{SOC}} = 1$ meV), the channels with a spin triplet vanish. Only in the case of a larger coupling ($\lambda_{\text{SOC}} = 10$ meV), the coexistence between both spin characters becomes apparent, since the spin-triplet solutions have finite values.

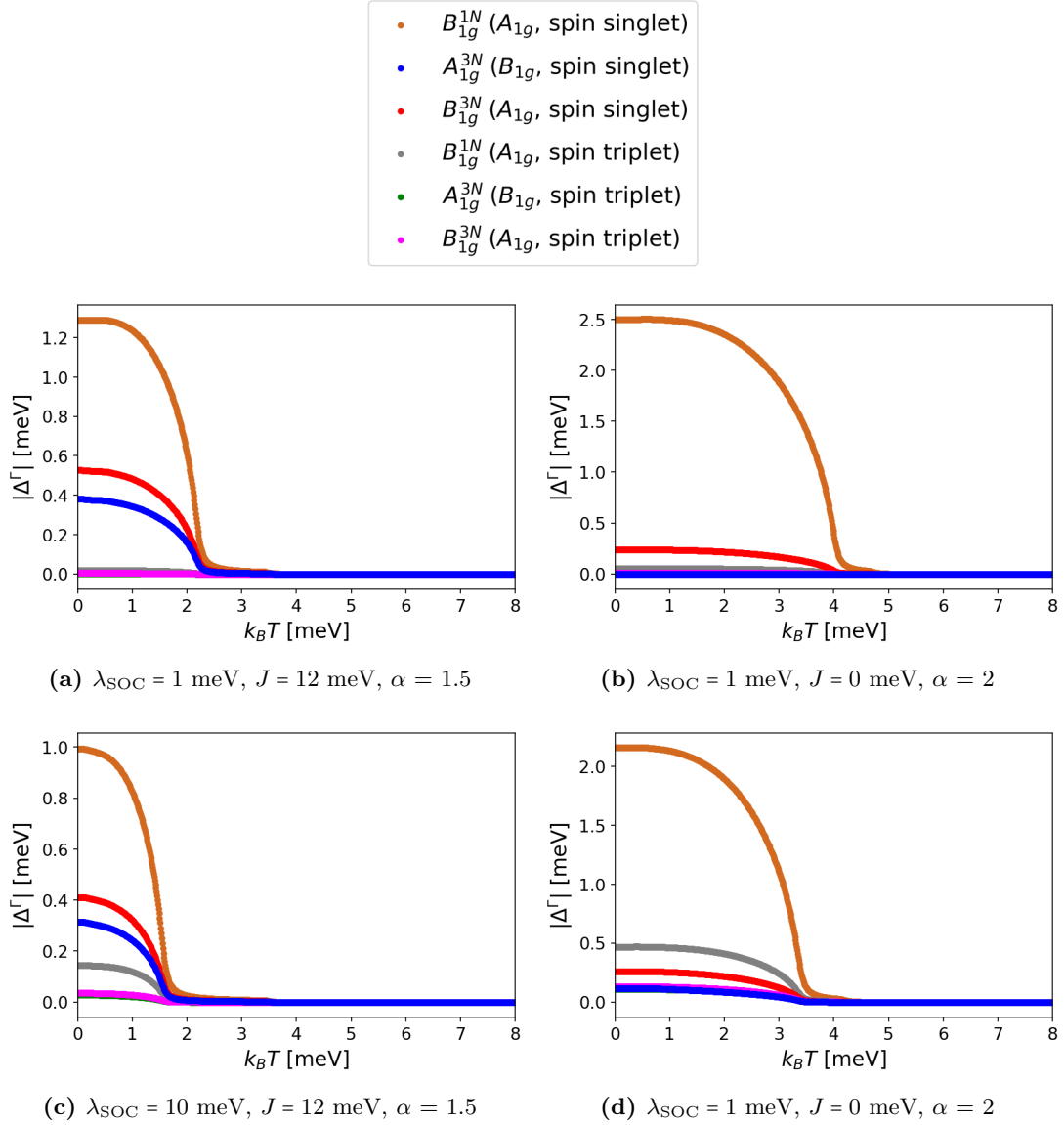


Figure 8.6: Leading superconducting order parameter channels according to Table 7.1 as a function of temperature, including up to sixth neighbors and on-site interaction. The odd-parity solutions are suppressed in all cases. We consider $N = 81$ in all plots, but the λ_{SOC} , the J and the boost (α) values are different, as specified in each caption. The first label in the legend corresponds to the basis function IR specifying the range of the interaction, and inside the parenthesis it is included the IR in orbital and spin space, detailing the spin character. Other channels with a smaller gap are also present, but they all have the same transition temperature.

8.4 Nodal structure

Another interesting characterization of the superconducting state is obtained by looking at the form of the nodal structure, so that we are able to see if the gap has accidental nodes (zeros of the order parameter) or symmetry imposed nodes due to the form of the basis function in momentum space. In addition, we seek agreement with the spectroscopic probes that have shown evidence for nodes in the superconducting gap [55, 56]. In this section, we will always consider the full model with 28 neighbors.

With this purpose, we want to include the combination for all neighbors considered in our picture arising from the same channel, according to Table 7.1, but only including the form factors transforming as the same IR. Thus, we are able to characterize with the same IR in momentum space, as well as detail the orbital/spin IR. Hence, including up to sixth neighbors with an on-site interaction, if we are interested in the A_{1g} irreducible representation in momentum space, we need to calculate

$$\begin{aligned} \Delta_{\mathbf{k}}^{A_{1g}} = & \Sigma_i^{0N} + (\cos k_x + \cos k_y) \Sigma_i^{1N} + 2 \cos k_x \cos k_y \Sigma_i^{2N} + (\cos 2k_x + \cos 2k_y) \Sigma_i^{3N} \\ & + \sqrt{2}(\cos 2k_x \cos k_y + \cos k_x \cos 2k_y) \Sigma_i^{4N} + 2 \cos 2k_x \cos 2k_y \Sigma_i^{5N} + (\cos 3k_x + \cos 3k_y) \Sigma_i^{6N}, \end{aligned} \quad (8.4)$$

where Σ_i^{mN} corresponds to one of the channels given in Table 7.1 and mN indicates the different neighbors, with $0N$ denoting the on-site superconducting order parameter contribution. For instance, if we are interested in the A_{1g} intraorbital triplet and spin singlet (first row of the Table), in the case of first neighbors this corresponds to $\Sigma_1^{1N} = \frac{1}{3}([\Delta_{A_{1g}}^{1N}]_{1\downarrow}^{1\uparrow} + [\Delta_{A_{1g}}^{1N}]_{2\downarrow}^{2\uparrow} + [\Delta_{A_{1g}}^{1N}]_{3\downarrow}^{3\uparrow})$. If we focus now on the case of the B_{1g} irreducible representation, the expression becomes simpler,

$$\begin{aligned} \Delta_{\mathbf{k}}^{B_{1g}} = & (\cos k_x - \cos k_y) \Sigma_i^{1N} + (\cos 2k_x - \cos 2k_y) \Sigma_i^{3N} \\ & + \sqrt{2}(\cos 2k_x \cos k_y - \cos k_x \cos 2k_y) \Sigma_i^{4N} + (\cos 3k_x - \cos 3k_y) \Sigma_i^{6N}. \end{aligned} \quad (8.5)$$

As stated in the previous section, from Figure 8.5 it can be seen that the leading contributions are given by the A_{1g} and B_{1g} irreducible representations. Consequently, we can focus only on the nodal structure from those 2 IRs, distinguishing the spin-singlet and spin-triplet characters. In Figure 8.7, the convergent values after performing the self-consistent calculations are shown, corresponding to spin singlet and, therefore, orbital triplet, remembering that all odd-parity channels are suppressed. As observed, the structure for the A_{1g} IR fulfills all the symmetries of the point group D_{4h} , whereas the B_{1g} IR breaks some symmetries, and it has nodes along the diagonals.

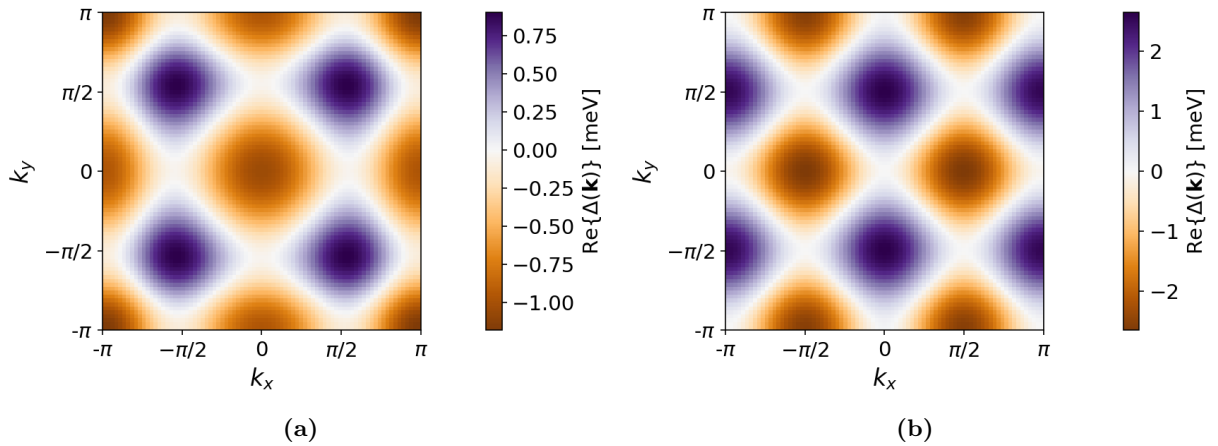


Figure 8.7: Real part of the superconducting order parameter in momentum space for a) A_{1g} and b) B_{1g} irreducible representations. The color bar corresponds to the values of the gap, and the zeros indicate the nodes. We consider $N = 81$, $k_B T = 0.01$ meV, $J = 12$ meV, $\lambda_{\text{SOC}} = 35$ meV and a boost $\alpha = 1.7$. Both cases correspond to the leading spin-singlet and orbital-triplet channel in Table 7.1.

Since we are interested in the values of the gap at the Fermi level, where the electrons contributing to superconductivity are located, the best way to visualize the zeros of the gap is to project the nodal structure onto the Fermi surface. We can see the results of this projection in Figure 8.8, where it is plotted the momentum dependence of the superconducting gap for the leading even-parity solutions A_{1g} and B_{1g} , distinguishing now between spin-singlet and spin-triplet solutions.

In agreement with Figure 8.5b, the leading solution corresponds to the basis functions transforming as an A_{1g} IR, whereas the ones transforming as a B_{1g} are subleading. In addition, it can also be seen that the spin-triplet character has a non-negligible contribution, although the nodal structure shows significant differences when comparing with the singlet case. In particular, from Figure 8.8b we can observe that for the A_{1g} IR with spin triplet, the α and the β bands have no nodes. This contrasts with Figure 8.8d, which corresponds to the B_{1g} IR again with spin-triplet character, since all bands display nodes. We can realize that the real part of the order parameter is plotted, since we are interested in the changes of the sign of the gap. Importantly, as shown in Figure 8.9, the absolute value of the gap displays the same nodes.

The nodal structure for other Hund's coupling values has also been calculated, as presented in Appendix F. Importantly, all Hund's couplings studied have an almost identical structure of the gap for the leading irreducible representations. Additionally, the results for the nodal structure omitting the on-site interactions are also included (see Figure F.3).

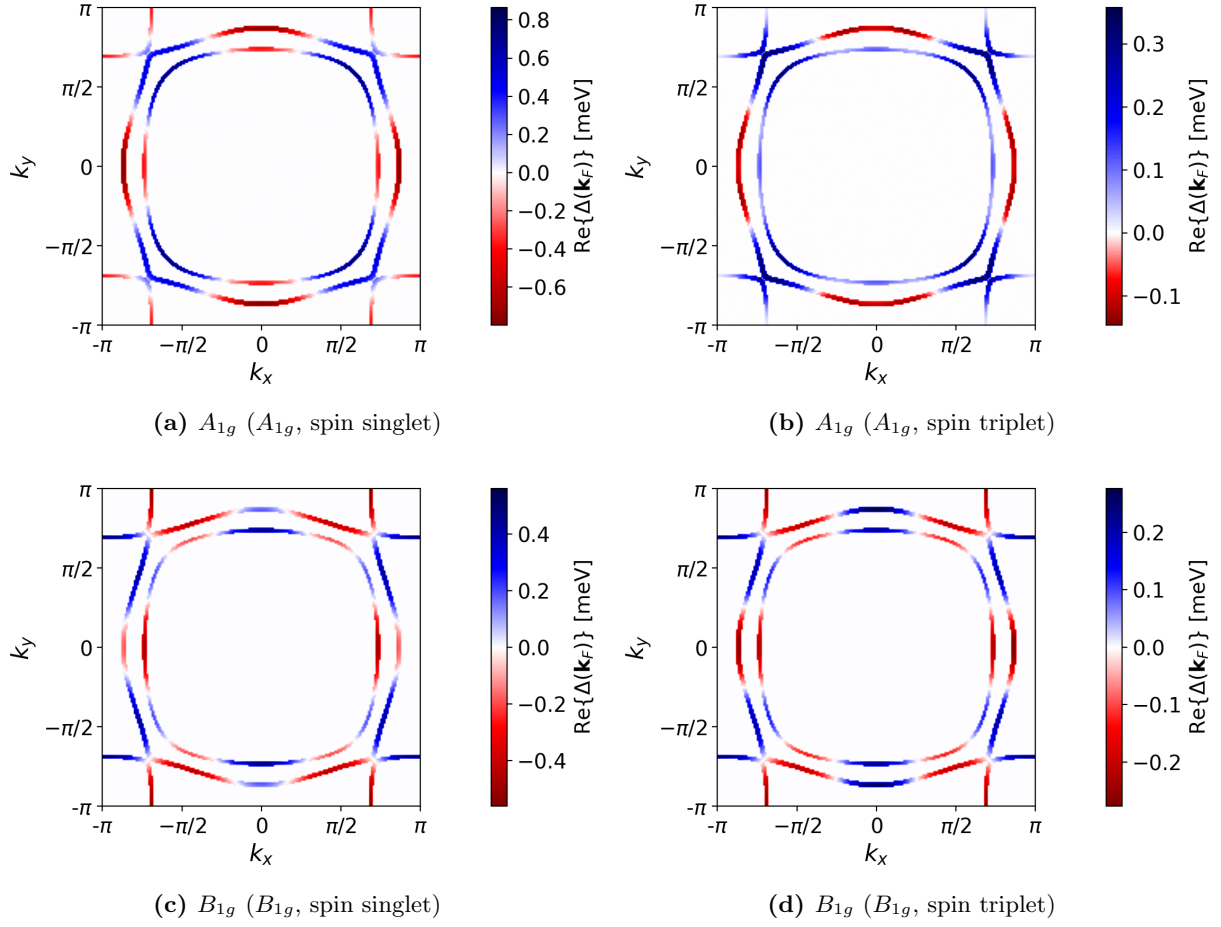


Figure 8.8: Real part of the superconducting order parameter projected on the Fermi surface, where the color bar corresponds to the values of the gap. We consider $N = 81$, $k_B T = 0.01$ meV, $J = 12$ meV, $\lambda_{\text{SOC}} = 35$ meV and a boost $\alpha = 1.7$. The corresponding irreducible representation in momentum space is specified in each caption, and in parenthesis it is detailed the IR in orbital/spin space and the spin character of the particular channel.

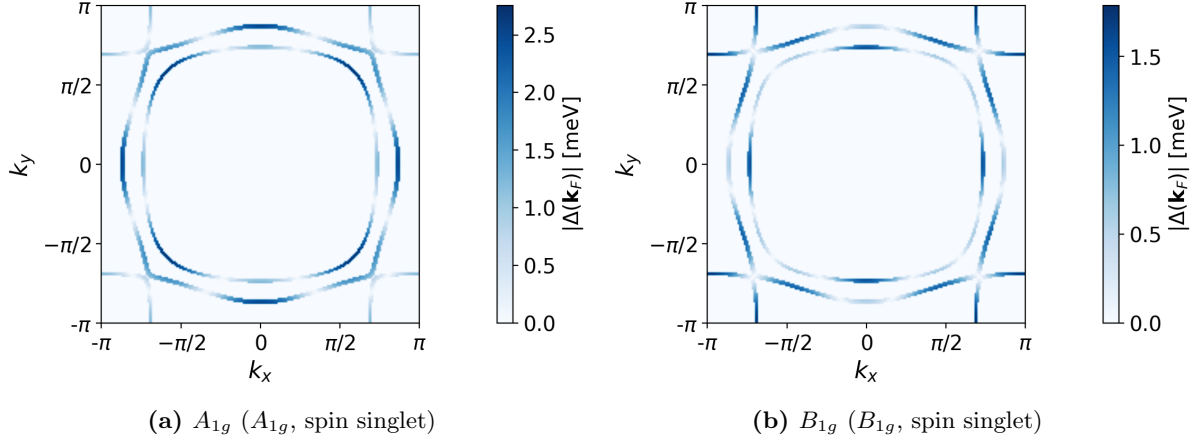


Figure 8.9: Absolute value of the superconducting order parameter projected on the Fermi surface, where the color bar corresponds to the values of the gap. We consider $N = 81$, $k_B T = 0.01$ meV, $J = 12$ meV, $\lambda_{\text{SOC}} = 35$ meV and a boost $\alpha = 1.7$. The corresponding irreducible representation in momentum space is specified in each caption, and in parenthesis it is detailed the IR in orbital/spin space and the spin character of the particular channel.

8.5 Time-reversal symmetry

From the previous results, it is clearly seen that at low temperatures there is a coexistence of s' (A_{1g}) and $d_{x^2-y^2}$ (B_{1g}). Therefore, this seem to indicate that the total superconducting state could be in a combination of the type $s' \pm d_{x^2-y^2}$ or $s' \pm id_{x^2-y^2}$. At this point, time-reversal symmetry (TRS) becomes crucial to identify the state, since the second proposal would break it as a consequence of the i factor. Nevertheless, we are dealing with a multi-orbital model, and, as a consequence, we need to generalise the TRS operator in the basis $\{xz \uparrow, xz \downarrow, yz \uparrow, yz \downarrow, xy \uparrow, xy \downarrow\}$. With this purpose, we remember that, as previously stated, in the usual spin basis $\{\uparrow, \downarrow\}$, the TRS operator is given by $\Theta = i\sigma_y K$, where K denotes complex conjugation.

Since in the orbital degrees of freedom TRS acts only as a complex conjugation, in the basis chosen the generalization is simple and corresponds to

$$\Theta = \mathbb{1}_\lambda \otimes (i\sigma_y)K. \quad (8.6)$$

Therefore, the Hamiltonian including the normal-state and the spin-orbit coupling, and the order parameter 6×6 matrices fulfill TRS if

$$\begin{aligned} \hat{h}(\mathbf{k}) &= \Theta \hat{h}(\mathbf{k}) \Theta^{-1}, \\ \hat{\Delta}(\mathbf{k}) &= \Theta \hat{\Delta}(\mathbf{k}) \Theta^{-1}. \end{aligned} \quad (8.7)$$

With the explicit form of the operator in the 6×6 basis, these expressions correspond to

$$\begin{aligned}\hat{h}(\mathbf{k}) &= \mathbb{1}_\lambda \otimes \sigma_y [\hat{h}(-\mathbf{k})]^* \mathbb{1}_\lambda \otimes \sigma_y, \\ \hat{\Delta}(\mathbf{k}) &= \mathbb{1}_\lambda \otimes \sigma_y [\hat{\Delta}(-\mathbf{k})]^* \mathbb{1}_\lambda \otimes \sigma_y.\end{aligned}\tag{8.8}$$

We can verify first that the normal-state Hamiltonian will be invariant under TRS, which is trivial when recalling its form given in equation (5.33), as it couples to $\mathbb{1}_\sigma$ and is real and even under $\mathbf{k} \rightarrow -\mathbf{k}$. The same happens for the spin-orbit coupling Hamiltonian,

$$H_{\text{SOC}} = \frac{\lambda_{\text{SOC}}}{2} (\lambda_2 \sigma_z - \lambda_5 \sigma_x + \lambda_7 \sigma_y),\tag{8.9}$$

which fulfills

$$\mathbb{1}_\lambda \otimes \sigma_y [\lambda_2 \sigma_z - \lambda_5 \sigma_x + \lambda_7 \sigma_y]^* \mathbb{1}_\lambda \otimes \sigma_y = \sigma_y (-\lambda_2 \sigma_z + \lambda_5 \sigma_x + \lambda_7 \sigma_y) \sigma_y = H_{\text{SOC}},\tag{8.10}$$

using the form of the Gell-Mann matrices shown in Appendix B.

Once the previous checks have been performed, we can see if the order parameter fulfills TRS. As a first step, a test case has been considered with the simple case of a three band model with on-site attraction, back to the first part of the thesis. By applying the TRS operator, we have been able to demonstrate that this symmetry is not broken. However, an appropriate choice of the gauge has to be made so that all order parameter components are real.

Finally, we are able to deal with the model for Sr_2RuO_4 including the spin-fluctuation mechanism. Remarkably, for all Hund's couplings considered, below the transition temperature TRS is broken, which would be in agreement with the muon spin relaxation and polar Kerr effect experimental evidences introduced in Chapter 2. Further studies should be performed to verify this. Similar to the one-band model with nearest neighbors interactions, a natural next approach would be to solve the same three-orbital model in the real space case, so that the existence of currents around impurities could be studied, as expected for a TRS breaking state (see Figure 6.3).

8.6 Specific heat

After having studied the coexistence of the different channels, it is also interesting to compute the electronic specific heat. This way, we are able to see if the different irreducible representations lead to different phase transitions or, on the other hand, if only one phase transition is found, which would agree with the experimental evidence shown in Figure 2.6a.

In Figure 8.10, it is plotted the entropy, the electronic specific heat and the electronic specific heat divided by temperature as a function of temperature, for the case $J = 12$ and a boost $\alpha = 1.7$. Therefore, it corresponds to the same data shown for the order parameter channels as in Figure 8.5b, and we can indeed see that the phase transition from the superconducting to the normal

state occurs at the same temperature. As expected, above the critical temperature the behaviour is the same as in the normal-state case, shown in Figure 7.2. Importantly, although we can see that the form for C_e/T seems to agree with the experimental measurements, no evidence for two phase transitions is observed. However, since all phases seem to have the same transition temperature it could be that they are all contained in the same curve.

In the case of Hund's couplings $J = 0$ meV and $J = 24$ meV, similar results have been observed displaying only one phase transition. Nonetheless, the case $J = 36$ meV is remarkable. As shown in Figure 8.11, the entropy only has a small bump, and therefore the shape of C_e/T is different. This behaviour is attributed to the effect of considering a very large Hund's coupling.

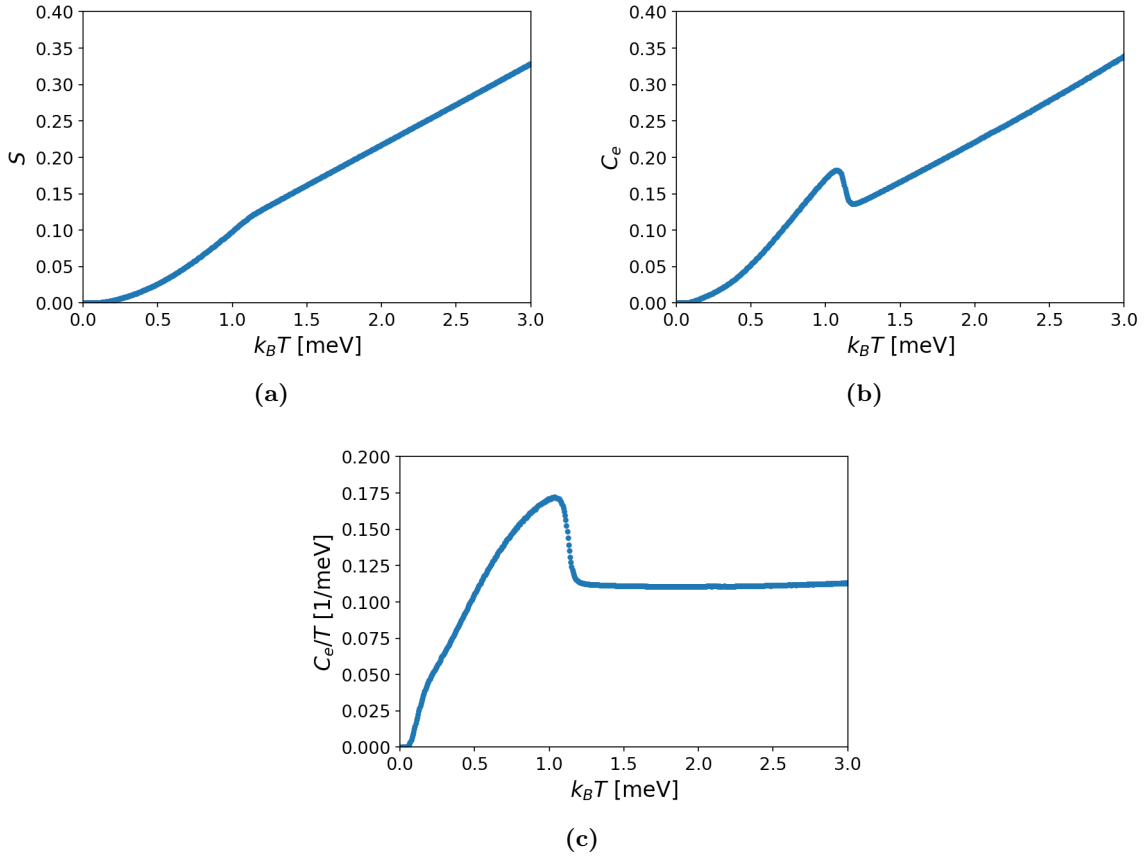


Figure 8.10: Entropy, specific heat and specific heat divided by temperature as a function of temperature, including up to sixth neighbors and on-site interactions. We consider $N = 141$, $J = 12$ meV, $\lambda_{\text{SOC}} = 35$ meV, and boost $\alpha = 1.7$.

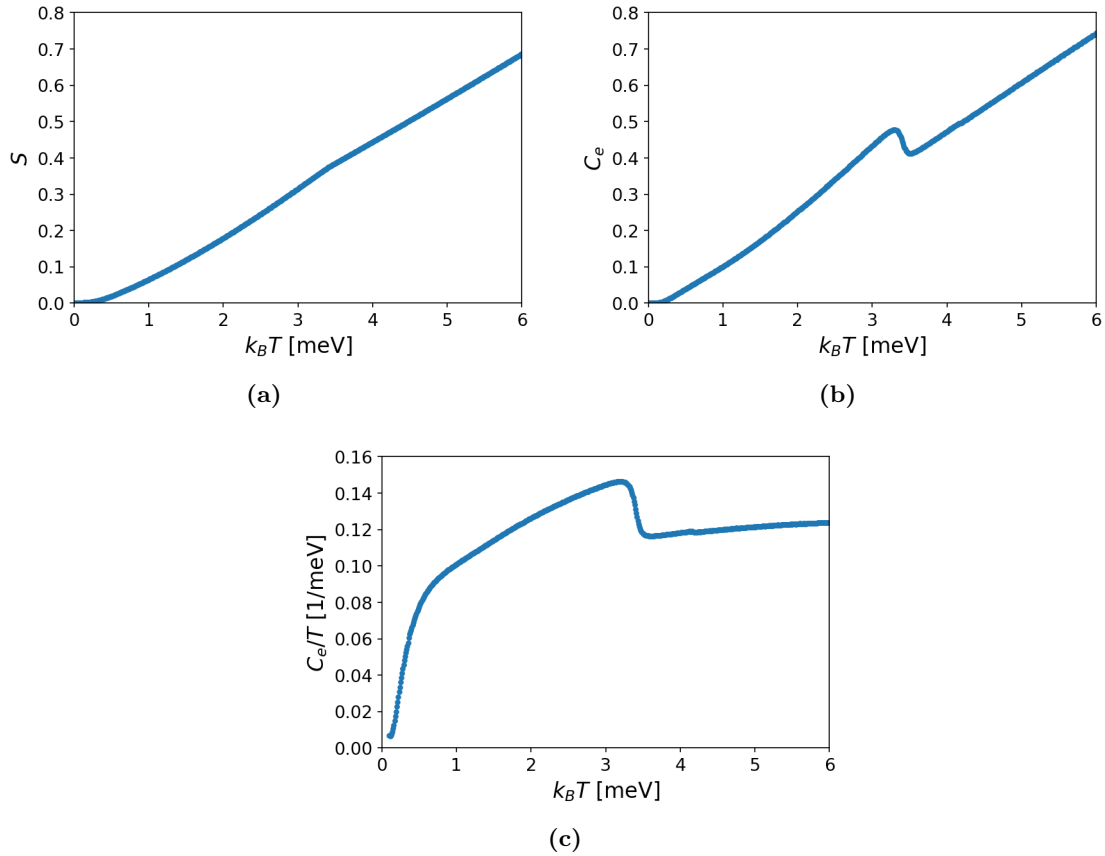


Figure 8.11: Entropy, specific heat and specific heat divided by temperature as a function of temperature, including up to sixth neighbors and on-site interactions. We consider $N = 81$, $J = 36$ meV, $\lambda_{\text{SOC}} = 35$ meV, and boost $\alpha = 0.75$.

8.7 Effect of the boost

As may have been noticed from the last sections, the appropriate choice of the boost has an important effect in order to obtain superconducting order parameters of the order of a few meV, in agreement with STM experiments (see Figure 2.7). In addition, since we have a complicated three-band model, the effect of the boost in the order parameters is not linear, as would be expected in a simple one-band model. Moreover, depending on the boost the transition temperature to the normal state changes accordingly.

In this section, we investigate the effect of a larger boost, leading to the appearance of new superconducting order parameters channels. Therefore, these results will allow us to study how the specific heat changes when new phases arise, and confirm if we are able to detect two phase transitions.

To begin with, we consider the case of $J = 12$ meV with a boost $\alpha = 3$. As seen in Figure 8.12a, two transition temperatures occur when looking at the order parameter IRs. The two distinct phase transitions could be explained since new order parameters appear with a global transformation B_{1g} , considering both momentum and spin/orbital behaviour, which is in contrast with the total transformation as an A_{1g} obtained for the order parameters channels with the larger transition temperature.

In this case, we would expect that the specific heat would show some jump at the lower transition temperature. However, as presented in Figure 8.12b, only one transition is seen. This could be due to a numerical convergence issue, since the transition to the normal state for the lower critical temperature does not show a sharp decrease, necessary to observe a jump in the specific heat. Therefore, this could be resolved by increasing the precision of the convergence condition.

In addition, we have also studied the same effect for the largest Hund's coupling, shown in Figure 8.13. Similarly, focusing on the order parameters, two transition temperatures can be seen, but the curves show a sharper decrease to the normal state. In contrast to the previous case, the specific heat displays two transitions, being the first one considerably smaller than the second one. Therefore, further studies should be performed in the future to see the effect of the numerical convergence, since it is extremely important to see a sharp transition to the normal state.

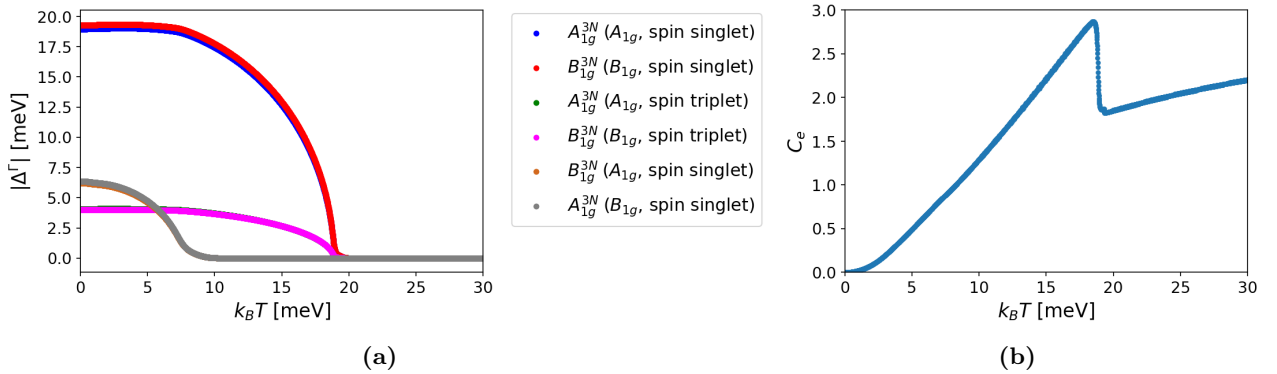


Figure 8.12: Leading superconducting order parameter channels according to Table 7.1 and corresponding specific heat as a function of temperature, including up to sixth neighbors and on-site interactions. The odd-parity solutions are suppressed. We consider $N = 81$, $J = 12$ meV, $\lambda_{\text{SOC}} = 35$ meV, and a boost $\alpha = 3$. The first label in the legend corresponds to the basis function IR specifying the range of the interaction, and inside the parenthesis it is included the IR in orbital and spin space, detailing the spin character. Other channels with a smaller gap are also present, with the same transition temperatures.

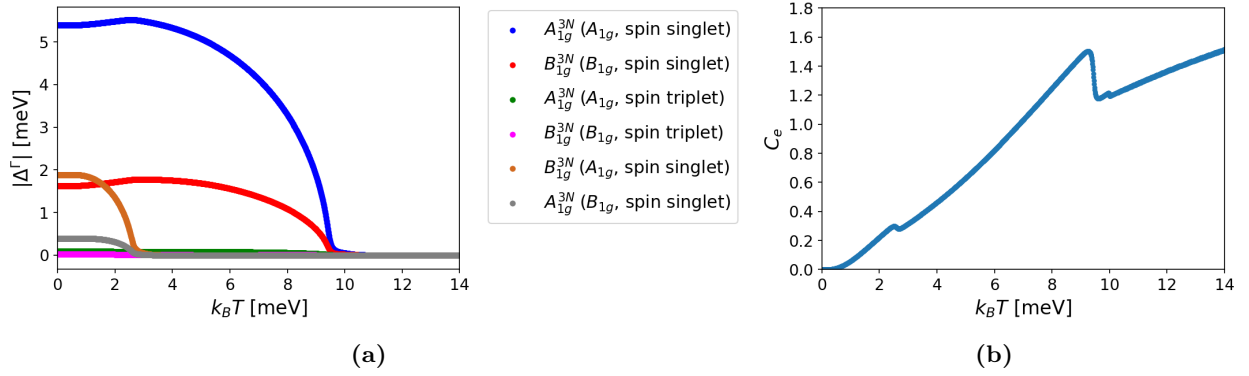


Figure 8.13: Leading superconducting order parameter channels according to Table 7.1 and corresponding specific heat as a function of temperature, including up to sixth neighbors and on-site interactions. The odd-parity solutions are suppressed. We consider $N = 81$, $J = 36$ meV, $\lambda_{\text{SOC}} = 35$ meV, and a boost $\alpha = 1$. The first label in the legend corresponds to the basis function IR specifying the range of the interaction, and inside the parenthesis it is included the IR in orbital and spin space, detailing the spin character. Other channels with a smaller gap are also present, with the same transition temperatures.

Chapter 9

Conclusions and outlook

9.1 Conclusions

In this thesis we have constructed a three-orbital model that is able to describe superconductivity in Sr_2RuO_4 , by performing a mean-field decoupling in the Cooper channel and solving self-consistently for the order parameter. In the first part, superconductivity was included as an on-site attractive term, whereas in the second part, a more realistic interaction was implemented driven by the spin-fluctuation mechanism. In the latter case, a new model was derived based on the inclusion of up to 28 neighbors, performing a thorough classification of the order parameter symmetry according to the basis functions and the orbital and spin space character, using the point group symmetry of Sr_2RuO_4 . This model successfully allowed us to distinguish the mixture between spin singlet and spin triplet, and introduced a numerical improvement when solving self-consistently.

In the three-orbital on-site attractive model, we have shown that impurities have an effect even in the sites further from the defect. The one-band model including nearest neighbor interactions revealed a region where the A_{1g} and the B_{1g} irreducible representations coexist. In contrast with the case of Sr_2RuO_4 , two separate transition temperatures were seen. By studying the currents in the coexistence region, we verified that time-reversal symmetry is broken.

The results obtained from a spin-fluctuation mechanism indicate that the s' phase is leading for all Hund's coupling considered, although for the smaller J values there is also an important subleading contribution from the $d_{x^2-y^2}$ symmetry. Therefore, our results prove that the coexistence does not correspond to an accidental degeneracy for a single Hund's coupling, since it is always present at lower temperatures. Remarkably, we have seen that both phases have the same transition temperature. Considering that smaller values for the spin-orbit coupling significantly changed the results, we have concluded that the role of a large coupling is extremely important. The effect of the boost has also been studied, showing that different transitions can be seen in the specific heat.

Finally, since the challenge in Sr_2RuO_4 is to propose a superconducting state compatible with all experimental observations, we conclude by comparing our results with the measurements. In agreement with the recent Knight shift experiments [6], we have observed that the leading symmetries always correspond to an even-parity spin-singlet character. The suppression of the odd-parity channels further corroborates that Sr_2RuO_4 can no longer be considered a chiral p -wave superconductor as previously accepted. Moreover, by generalizing the time-reversal symmetry operator to a multi-orbital system, we have seen that below the critical temperature this symmetry is broken, in agreement with muon spin relaxation and polar Kerr effect measurements [5, 37]. We have also observed the coexistence of the s' and the $d_{x^2-y^2}$ symmetries, corresponding to a two-component order parameter. In addition, we have studied the nodal structure of the superconducting order parameter at the Fermi surface, finding the existence of nodes in all the leading channels, in agreement with STM measurements [40, 41]. Furthermore, we have obtained a specific heat curve in the case $J/U = 0.1$ similar to the experimental measurements [38], where only one phase transition is observed.

9.2 Outlook

Recent ultrasound measurements have provided evidence for a two-component superconducting order parameter in Sr_2RuO_4 with a total symmetry xy [57, 58]. With the addition of longer-range Coulomb interactions in the linearized gap equation, it has been revealed the possibility of a $s' + id_{xy}$ phase [59], which seems to fulfill all experimental constrains. Hence, the inclusion of these longer-range Coulomb interactions would be a crucial additional investigation.

Furthermore, it has been suggested that the two phase transitions could be hidden inside the peak observed. As done in Ref. [43], this can be resolved by applying a strain to our system, which should separate the transition temperatures. Nevertheless, under the effect of a strain, the system lowers its symmetry to the point group D_{2h} . Consequently, the classification in terms of the irreducible representations of the point group D_{4h} no longer holds. In order to obtain the channels in the new point group, an essential continuation would be to derive the basis functions and the tables for orbital and spin space in this case.

Another further study would be to derive the same model for the real space case, including spin-fluctuation mediated pairing. This would allow us to observe the effect of impurities in a more realistic model, and see how they affect the homogeneous solutions. Importantly, with the inclusion of impurities we would be able to study the currents, and verify that time-reversal symmetry is broken below the critical temperature. Finally, another interesting extension would be to study the effect of magnetism. In this thesis, we have only included the mean-field decoupling in the Cooper channel to study solely the superconducting effects, but the decoupling in the particle-hole channel could also be added, probably yielding to the interplay of new exotic phenomena.

Bibliography

- [1] Y. Maeno, H. Hashimoto, K. Yoshida, S. Nishizaki, T. Fujita, J. Bednorz, and F. Lichtenberg, *Nature* **372**, 532 (1994).
- [2] T. M. Rice and M. Sigrist, *Journal of Physics: Condensed Matter* **7**, L643 (1995).
- [3] G. Baskaran, *Physica B: Condensed Matter* **223-224**, 490 (1996).
- [4] K. Ishida, H. Mukuda, Y. Kitaoka, K. Asayama, Z. Mao, Y. Mori, and Y. Maeno, *Nature* **396**, 658 (1998).
- [5] G. M. Luke, Y. Fudamoto, K. Kojima, M. Larkin, J. Merrin, B. Nachumi, Y. Uemura, Y. Maeno, Z. Mao, Y. Mori, *et al.*, *Nature* **394**, 558 (1998).
- [6] A. Pustogow, Y. Luo, A. Chronister, Y.-S. Su, D. Sokolov, F. Jerzembeck, A. P. Mackenzie, C. W. Hicks, N. Kikugawa, S. Raghu, *et al.*, *Nature* **574**, 72 (2019).
- [7] T. Oguchi, *Phys. Rev. B* **51**, 1385 (1995).
- [8] M. W. Haverkort, I. S. Elfimov, L. H. Tjeng, G. A. Sawatzky, and A. Damascelli, *Phys. Rev. Lett.* **101**, 026406 (2008).
- [9] A. T. Rømer, D. D. Scherer, I. M. Eremin, P. J. Hirschfeld, and B. M. Andersen, *Phys. Rev. Lett.* **123**, 247001 (2019).
- [10] K. Yoshida, Y. Maeno, S. Nishizaki, and T. Fujita, *Physica C: Superconductivity* **263**, 519 (1996).
- [11] Z. Mao, Y. Maeno, and H. Fukazawa, *Materials Research Bulletin* **35**, 1813 (2000).
- [12] A. P. Mackenzie, R. K. W. Haselwimmer, A. W. Tyler, G. G. Lonzarich, Y. Mori, S. Nishizaki, and Y. Maeno, *Phys. Rev. Lett.* **80**, 161 (1998).
- [13] A. P. Mackenzie, S. R. Julian, A. J. Diver, G. J. McMullan, M. P. Ray, G. G. Lonzarich, Y. Maeno, S. Nishizaki, and T. Fujita, *Phys. Rev. Lett.* **76**, 3786 (1996).

- [14] Y. Maeno, K. Yoshida, H. Hashimoto, S. Nishizaki, S.-i. Ikeda, M. Nohara, T. Fujita, A. P. Mackenzie, N. E. Hussey, J. G. Bednorz, and F. Lichtenberg, [Journal of the Physical Society of Japan](#) **66**, 1405 (1997).
- [15] Y. Maeno, T. M. Rice, and M. Sigrist, [Physics Today](#) **54**, 42 (2001).
- [16] C. Bergemann, S. R. Julian, A. P. Mackenzie, S. NishiZaki, and Y. Maeno, [Phys. Rev. Lett.](#) **84**, 2662 (2000).
- [17] A. Damascelli, D. H. Lu, K. M. Shen, N. P. Armitage, F. Ronning, D. L. Feng, C. Kim, Z.-X. Shen, T. Kimura, Y. Tokura, Z. Q. Mao, and Y. Maeno, [Phys. Rev. Lett.](#) **85**, 5194 (2000).
- [18] A. Tamai, M. Zingl, E. Rozbicki, E. Cappelli, S. Riccò, A. de la Torre, S. McKeown Walker, F. Y. Bruno, P. D. C. King, W. Meevasana, M. Shi, M. Radović, N. C. Plumb, A. S. Gibbs, A. P. Mackenzie, C. Berthod, H. U. R. Strand, M. Kim, A. Georges, and F. Baumberger, [Phys. Rev. X](#) **9**, 021048 (2019).
- [19] J. Bardeen, L. N. Cooper, and J. R. Schrieffer, [Phys. Rev.](#) **108**, 1175 (1957).
- [20] M. Sigrist, [AIP Conference Proceedings](#) **789**, 165 (2005).
- [21] A. P. Mackenzie and Y. Maeno, [Rev. Mod. Phys.](#) **75**, 657 (2003).
- [22] M. Braden, P. Steffens, Y. Sidis, J. Kulda, P. Bourges, S. Hayden, N. Kikugawa, and Y. Maeno, [Phys. Rev. Lett.](#) **92**, 097402 (2004).
- [23] J. R. Kirtley, C. Kallin, C. W. Hicks, E.-A. Kim, Y. Liu, K. A. Moler, Y. Maeno, and K. D. Nelson, [Phys. Rev. B](#) **76**, 014526 (2007).
- [24] C. W. Hicks, J. R. Kirtley, T. M. Lippman, N. C. Koshnick, M. E. Huber, Y. Maeno, W. M. Yuhasz, M. B. Maple, and K. A. Moler, [Phys. Rev. B](#) **81**, 214501 (2010).
- [25] P. J. Curran, S. J. Bending, W. M. Desoky, A. S. Gibbs, S. L. Lee, and A. P. Mackenzie, [Phys. Rev. B](#) **89**, 144504 (2014).
- [26] E. Pavarini and I. I. Mazin, [Phys. Rev. B](#) **74**, 035115 (2006).
- [27] E. J. Rozbicki, J. F. Annett, J.-R. Souquet, and A. P. Mackenzie, [Journal of Physics: Condensed Matter](#) **23**, 094201 (2011).
- [28] C. N. Veenstra, Z.-H. Zhu, M. Raichle, B. M. Ludbrook, A. Nicolaou, B. Slomski, G. Landolt, S. Kittaka, Y. Maeno, J. H. Dil, I. S. Elfimov, M. W. Haverkort, and A. Damascelli, [Phys. Rev. Lett.](#) **112**, 127002 (2014).

- [29] J. F. Annett, G. Litak, B. L. Györfy, and K. I. Wysokiński, *Phys. Rev. B* **73**, 134501 (2006).
- [30] T. Scaffidi, J. C. Romers, and S. H. Simon, *Phys. Rev. B* **89**, 220510 (2014).
- [31] A. Ramires and M. Sgrist, *Phys. Rev. B* **100**, 104501 (2019).
- [32] A. P. Mackenzie, T. Scaffidi, C. W. Hicks, and Y. Maeno, *npj Quantum Materials* **2**, 1 (2017).
- [33] S. A. Kivelson, A. C. Yuan, B. Ramshaw, and R. Thomale, *npj Quantum Materials* **5**, 1 (2020).
- [34] J. A. Duffy, S. M. Hayden, Y. Maeno, Z. Mao, J. Kulda, and G. J. McIntyre, *Phys. Rev. Lett.* **85**, 5412 (2000).
- [35] K. Ishida, M. Manago, T. Yamanaka, H. Fukazawa, Z. Q. Mao, Y. Maeno, and K. Miyake, *Phys. Rev. B* **92**, 100502 (2015).
- [36] K. Ishida, M. Manago, K. Kinjo, and Y. Maeno, *Journal of the Physical Society of Japan* **89**, 034712 (2020).
- [37] J. Xia, Y. Maeno, P. T. Beyersdorf, M. M. Fejer, and A. Kapitulnik, *Phys. Rev. Lett.* **97**, 167002 (2006).
- [38] S. NishiZaki, Y. Maeno, and Z. Mao, *Journal of the Physical Society of Japan* **69**, 572 (2000).
- [39] Y.-S. Li, N. Kikugawa, D. A. Sokolov, F. Jerzembeck, A. S. Gibbs, Y. Maeno, C. W. Hicks, J. Schmalian, M. Nicklas, and A. P. Mackenzie, *Proceedings of the National Academy of Sciences* **118** (2021), 10.1073/pnas.2020492118, <https://www.pnas.org/content/118/10/e2020492118.full.pdf> .
- [40] I. A. Firmo, S. Lederer, C. Lupien, A. P. Mackenzie, J. C. Davis, and S. A. Kivelson, *Phys. Rev. B* **88**, 134521 (2013).
- [41] R. Sharma, S. D. Edkins, Z. Wang, A. Kostin, C. Sow, Y. Maeno, A. P. Mackenzie, J. C. S. Davis, and V. Madhavan, *Proceedings of the National Academy of Sciences* **117**, 5222 (2020).
- [42] C. Bergemann, A. P. Mackenzie, S. R. Julian, D. Forsythe, and E. Ohmichi, *Advances in Physics* **52**, 639 (2003).
- [43] A. T. Rømer, A. Kreisel, M. A. Müller, P. J. Hirschfeld, I. M. Eremin, and B. M. Andersen, *Phys. Rev. B* **102**, 054506 (2020).

- [44] S. Cobo, F. Ahn, I. Eremin, and A. Akbari, [Phys. Rev. B **94**, 224507 \(2016\)](#).
- [45] Z. Wang, X. Wang, and C. Kallin, [Phys. Rev. B **101**, 064507 \(2020\)](#).
- [46] V. Zabolotnyy, D. Evtushinsky, A. Kordyuk, T. Kim, E. Carleschi, B. Doyle, R. Fittipaldi, M. Cuoco, A. Vecchione, and S. Borisenko, [Journal of Electron Spectroscopy and Related Phenomena **191**, 48 \(2013\)](#).
- [47] J. Mravlje, M. Aichhorn, T. Miyake, K. Haule, G. Kotliar, and A. Georges, [Phys. Rev. Lett. **106**, 096401 \(2011\)](#).
- [48] A. T. Rømer, *Spin-fluctuation mediated superconductivity and magnetic order in the cuprate $La_{1.88}Sr_{0.12}CuO_4$* , Ph.D. thesis, Niels Bohr Institute (2015).
- [49] J. F. Annett, *Superconductivity, superfluids and condensates*, Vol. 5 (Oxford University Press, 2004).
- [50] K. K. Ng and M. Sigrist, [Europhysics Letters \(EPL\) **49**, 473 \(2000\)](#).
- [51] M. Dresselhaus, G. Dresselhaus, and A. Jorio, *Group Theory: Application to the Physics of Condensed Matter* (Springer Berlin Heidelberg, 2007).
- [52] D. Mendler, *Topological phases in systems with coexisting density waves and superconductivity*, Ph.D. thesis, Karlsruhe Institute of Technology (2013).
- [53] J. J. Sakurai and J. Napolitano, *Modern Quantum Mechanics*, Quantum physics, quantum information and quantum computation (Cambridge University Press, Cambridge, 2017).
- [54] C. N. Breiø, *Impurity Induced Supercurrents in $s+id$ and $d+id$ superconductors*, Project Outside the Course Scope, Niels Bohr Institute (2020).
- [55] E. Hassinger, P. Bourgeois-Hope, H. Taniguchi, S. René de Cotret, G. Grissonnanche, M. S. Anwar, Y. Maeno, N. Doiron-Leyraud, and L. Taillefer, [Phys. Rev. X **7**, 011032 \(2017\)](#).
- [56] S. Kittaka, S. Nakamura, T. Sakakibara, N. Kikugawa, T. Terashima, S. Uji, D. A. Sokolov, A. P. Mackenzie, K. Irie, Y. Tsutsumi, K. Suzuki, and K. Machida, [Journal of the Physical Society of Japan **87**, 093703 \(2018\)](#).
- [57] S. Benhabib, C. Lupien, I. Paul, L. Berges, M. Dion, M. Nardone, A. Zitouni, Z. Mao, Y. Maeno, A. Georges, *et al.*, [Nature physics **17**, 194 \(2021\)](#).
- [58] S. Ghosh, A. Shekhter, F. Jerzembeck, N. Kikugawa, D. A. Sokolov, M. Brando, A. Mackenzie, C. W. Hicks, and B. Ramshaw, [Nature Physics **17**, 199 \(2021\)](#).
- [59] A. T. Rømer, P. Hirschfeld, and B. M. Andersen, [arXiv:2101.06972 \(2021\)](#).

Appendix A

On-site superconductivity in a one-band model using the spinor notation

We consider the BCS Hamiltonian, which is given by

$$H_{BCS} = \sum_{\mathbf{k}\sigma} \xi_{\mathbf{k}} c_{\mathbf{k}\sigma}^\dagger c_{\mathbf{k}\sigma} - \sum_{\mathbf{k}\mathbf{k}'} V_{\mathbf{k}\mathbf{k}'} c_{\mathbf{k}\uparrow}^\dagger c_{-\mathbf{k}\downarrow}^\dagger c_{-\mathbf{k}'\downarrow} c_{\mathbf{k}'\uparrow}. \quad (\text{A.1})$$

We perform a mean-field decoupling by introducing the gap $\Delta = -V \sum_{\mathbf{k}'} \langle c_{-\mathbf{k}'\downarrow} c_{\mathbf{k}'\uparrow} \rangle$, so that the Hamiltonian reads

$$H_{BCS}^{MF} = \sum_{\mathbf{k}\sigma} \xi_{\mathbf{k}} c_{\mathbf{k}\sigma}^\dagger c_{\mathbf{k}\sigma} + \sum_{\mathbf{k}} \Delta c_{\mathbf{k}\uparrow}^\dagger c_{-\mathbf{k}\downarrow}^\dagger + \sum_{\mathbf{k}} \Delta^* c_{-\mathbf{k}\downarrow} c_{\mathbf{k}\uparrow}. \quad (\text{A.2})$$

Introducing the Bogoliubov operators,

$$\begin{pmatrix} c_{\mathbf{k}\uparrow} \\ c_{-\mathbf{k}\downarrow}^\dagger \end{pmatrix} = \begin{pmatrix} u_{\mathbf{k}} & v_{\mathbf{k}}^* \\ -v_{\mathbf{k}} & u_{\mathbf{k}}^* \end{pmatrix} \begin{pmatrix} \gamma_{\mathbf{k}\uparrow} \\ \gamma_{-\mathbf{k}\downarrow}^\dagger \end{pmatrix}, \quad (\text{A.3})$$

the Hamiltonian becomes diagonal,

$$H_{BCS}^{MF} = \sum_{\mathbf{k}} E_{\mathbf{k}} \gamma_{\mathbf{k}\sigma}^\dagger \gamma_{\mathbf{k}\sigma}, \quad (\text{A.4})$$

with $E_{\mathbf{k}} = \sqrt{\xi_{\mathbf{k}}^2 + |\Delta|^2}$, $|u_{\mathbf{k}}| = \sqrt{\frac{1}{2} \left(1 + \frac{\xi_{\mathbf{k}}}{E_{\mathbf{k}}}\right)}$ and $|v_{\mathbf{k}}| = \sqrt{\frac{1}{2} \left(1 - \frac{\xi_{\mathbf{k}}}{E_{\mathbf{k}}}\right)}$.

The gap in terms of the new operators can then be written as

$$\Delta = -V \sum_{\mathbf{k}} u_{\mathbf{k}} v_{\mathbf{k}}^* (1 - 2f(E_{\mathbf{k}})) = -V \sum_{\mathbf{k}} \frac{\Delta}{2E_{\mathbf{k}}} \tanh \frac{E_{\mathbf{k}}}{2k_B T}, \quad (\text{A.5})$$

also in agreement with equation (5.15), which will be derived from a general formulation for a multi-orbital system.

The self-consistent equation for the gap can be solved numerically in \mathbf{k} -space for a 2D square lattice in the tight-binding model, considering the dispersion $\xi_{\mathbf{k}} = -2t(\cos k_x a + \cos k_y a)$. From the solution we can plot the gap Δ as a function of temperature, obtaining the plot in Figure A.1.

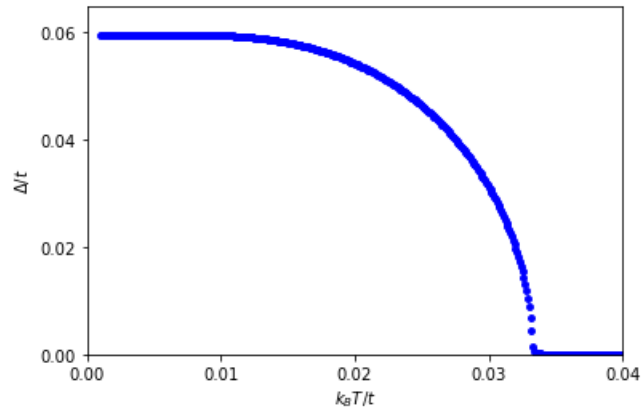


Figure A.1: Superconducting order parameter Δ as a function of temperature $k_B T$, considering an attraction strength of 1 meV.

Appendix B

SU(2) Generators and SU(3) Generators

The SU(2) Generators correspond to the Pauli matrices, forming a basis in 2×2 space with the identity matrix, and are given by

$$\sigma_x = \begin{pmatrix} 0 & 1 \\ 1 & 0 \end{pmatrix}, \quad \sigma_y = \begin{pmatrix} 0 & -i \\ i & 0 \end{pmatrix}, \quad \sigma_z = \begin{pmatrix} 1 & 0 \\ 0 & -1 \end{pmatrix}, \quad \mathbb{1}_\sigma = \begin{pmatrix} 1 & 0 \\ 0 & 1 \end{pmatrix}. \quad (\text{B.1})$$

Consequently, since they form a basis we can write all elements of a 2×2 matrix in terms of the previous matrices as

$$\begin{pmatrix} x & y \\ z & x' \end{pmatrix} = \frac{\mathbb{1}_\sigma + \sigma_z}{2}x + \frac{\mathbb{1}_\sigma - \sigma_z}{2}x' + \frac{\sigma_x + i\sigma_y}{2}y + \frac{\sigma_x - i\sigma_y}{2}z. \quad (\text{B.2})$$

The SU(3) Generators correspond to the Gell-Mann matrices, which form a basis in a 3×3 space, together with the identity matrix, and correspond to

$$\begin{aligned} \lambda_1 &= \begin{pmatrix} 0 & 1 & 0 \\ 1 & 0 & 0 \\ 0 & 0 & 0 \end{pmatrix}, & \lambda_2 &= \begin{pmatrix} 0 & -i & 0 \\ i & 0 & 0 \\ 0 & 0 & 0 \end{pmatrix}, & \lambda_3 &= \begin{pmatrix} 1 & 0 & 0 \\ 0 & -1 & 0 \\ 0 & 0 & 0 \end{pmatrix}, \\ \lambda_4 &= \begin{pmatrix} 0 & 0 & 1 \\ 0 & 0 & 0 \\ 1 & 0 & 0 \end{pmatrix}, & \lambda_5 &= \begin{pmatrix} 0 & 0 & -i \\ 0 & 0 & 0 \\ i & 0 & 0 \end{pmatrix}, & \lambda_6 &= \begin{pmatrix} 0 & 0 & 0 \\ 0 & 0 & 1 \\ 0 & 1 & 0 \end{pmatrix}, \\ \lambda_7 &= \begin{pmatrix} 0 & 0 & 0 \\ 0 & 0 & -i \\ 0 & i & 0 \end{pmatrix}, & \lambda_8 &= \frac{1}{\sqrt{3}} \begin{pmatrix} 1 & 0 & 0 \\ 0 & 1 & 0 \\ 0 & 0 & -2 \end{pmatrix}, & \mathbb{1}_\lambda &= \begin{pmatrix} 1 & 0 & 0 \\ 0 & 1 & 0 \\ 0 & 0 & 1 \end{pmatrix}. \end{aligned} \quad (\text{B.3})$$

Therefore, we can write each element of a 3×3 matrix as a combination of these 9 matrices:

$$\begin{aligned}
\begin{pmatrix} 1 & 0 & 0 \\ 0 & 0 & 0 \\ 0 & 0 & 0 \end{pmatrix} &= \frac{1}{3}\mathbb{1}_\lambda + \frac{1}{2}\lambda_3 + \frac{1}{2\sqrt{3}}\lambda_8, & \begin{pmatrix} 0 & 1 & 0 \\ 0 & 0 & 0 \\ 0 & 0 & 0 \end{pmatrix} &= \frac{1}{2}\lambda_1 + \frac{i}{2}\lambda_2, & \begin{pmatrix} 0 & 0 & 1 \\ 0 & 0 & 0 \\ 0 & 0 & 0 \end{pmatrix} &= \frac{1}{2}\lambda_4 + \frac{i}{2}\lambda_5, \\
\begin{pmatrix} 0 & 0 & 0 \\ 1 & 0 & 0 \\ 0 & 0 & 0 \end{pmatrix} &= \frac{1}{2}\lambda_1 - \frac{i}{2}\lambda_2, & \begin{pmatrix} 0 & 0 & 0 \\ 0 & 1 & 0 \\ 0 & 0 & 0 \end{pmatrix} &= \frac{1}{3}\mathbb{1}_\lambda - \frac{1}{2}\lambda_3 + \frac{1}{2\sqrt{3}}\lambda_8, & \begin{pmatrix} 0 & 0 & 0 \\ 0 & 0 & 1 \\ 0 & 0 & 0 \end{pmatrix} &= \frac{1}{2}\lambda_6 + \frac{i}{2}\lambda_7, \\
\begin{pmatrix} 0 & 0 & 0 \\ 0 & 0 & 0 \\ 1 & 0 & 0 \end{pmatrix} &= \frac{1}{2}\lambda_4 - \frac{i}{2}\lambda_5, & \begin{pmatrix} 0 & 0 & 0 \\ 0 & 0 & 0 \\ 0 & 1 & 0 \end{pmatrix} &= \frac{1}{2}\lambda_6 - \frac{i}{2}\lambda_7, & \begin{pmatrix} 0 & 0 & 0 \\ 0 & 0 & 0 \\ 0 & 0 & 1 \end{pmatrix} &= \frac{1}{3}\mathbb{1}_\lambda - \frac{1}{\sqrt{3}}\lambda_8. & (B.4)
\end{aligned}$$

Appendix C

Character table and product table for the point group D_{4h}

Table C.1: Character table for the group D_{4h} , including the irreducible representations (IR), where g and u denote respectively the even and odd IR, and the representative basis for rotations and functions to quadratic order.

IR	E	C_2	$2C_4$	$2C_2'$	$2C_2''$	\mathcal{I}	σ_h	$2S_4$	$2\sigma_v$	$2\sigma_d$	Linear, Rotations	Quadratic
A_{1g}	1	1	1	1	1	1	1	1	1	1	R_z	$x^2 + y^2, z^2$
A_{2g}	1	1	1	-1	-1	1	1	1	-1	-1		$x^2 - y^2$
B_{1g}	1	1	-1	1	-1	1	1	-1	1	-1		xy
B_{2g}	1	1	-1	-1	1	1	1	-1	-1	1		(xz, yz)
E_g	2	-2	0	0	0	2	-2	0	0	0		(R_x, R_y)
A_{1u}	1	1	1	1	1	-1	-1	-1	-1	-1	z	
A_{2u}	1	1	1	-1	-1	-1	-1	-1	1	1		
B_{1u}	1	1	-1	1	-1	-1	-1	1	-1	1		
B_{2u}	1	1	-1	-1	1	-1	-1	1	1	-1		
E_u	2	-2	0	0	0	-2	2	0	0	0		(x, y)

Table C.2: Product table for the point group D_{4h} .

\otimes	A_{1g}	A_{2g}	B_{1g}	B_{2g}	E_g	A_{1u}	A_{2u}	B_{1u}	B_{2u}	E_u
A_{1g}	A_{1g}	A_{2g}	B_{1g}	B_{2g}	E_g	A_{1u}	A_{2u}	B_{1u}	B_{2u}	E_u
A_{2g}	A_{2g}	A_{1g}	B_{2g}	B_{1g}	E_g	A_{2u}	A_{1u}	B_{2u}	B_{1u}	E_u
B_{1g}	B_{1g}	B_{2g}	A_{1g}	A_{2g}	E_g	B_{1u}	B_{2u}	A_{1u}	A_{2u}	E_u
B_{2g}	B_{2g}	B_{1g}	A_{2g}	A_{1g}	E_g	B_{2u}	B_{1u}	A_{2u}	A_{1u}	E_u
E_g	E_g	E_g	E_g	E_g	$A_{1g} \oplus A_{2g}$ $\oplus B_{1g} \oplus B_{2g}$	E_u	E_u	E_u	E_u	$A_{1u} \oplus A_{2u}$ $\oplus B_{1u} \oplus B_{2u}$
A_{1u}	A_{1u}	A_{2u}	B_{1u}	B_{2u}	E_u	A_{1g}	A_{2g}	B_{1g}	B_{2g}	E_g
A_{2u}	A_{2u}	A_{1u}	B_{2u}	B_{1u}	E_u	A_{2g}	A_{1g}	B_{2g}	B_{1g}	E_g
B_{1u}	B_{1u}	B_{2u}	A_{1u}	A_{2u}	E_u	B_{1g}	B_{2g}	A_{1g}	A_{2g}	E_g
B_{2u}	B_{2u}	B_{1u}	A_{2u}	A_{1u}	E_u	B_{2g}	B_{1g}	A_{2g}	A_{1g}	E_g
E_u	E_u	E_u	E_u	E_u	$A_{1u} \oplus A_{2u}$ $\oplus B_{1u} \oplus B_{2u}$	E_g	E_g	E_g	E_g	$A_{1g} \oplus A_{2g}$ $\oplus B_{1g} \oplus B_{2g}$

Appendix D

Representation in Nambu space

Due to spin-orbit coupling, we need to represent the elements $g \in D_{4h}$ in orbital and spin space. Nevertheless, Nambu space must also be included in the matrix representation. In this Appendix, the inclusion of the 2×2 Nambu space will be treated. The derivation is based in section 3.1 of Ref. [52].

We consider a general Hamiltonian describing a fermionic system of the form

$$\mathcal{H} = \hat{\Psi}^\dagger \hat{h} \hat{\Psi} + \frac{1}{2} \hat{\Psi}^\dagger \hat{\Delta} (\hat{\Psi})^T + \frac{1}{2} \hat{\Psi} \hat{\Delta} \hat{\Psi}, \quad (\text{D.1})$$

where $\hat{\Delta}$ and \hat{h} corresponds to the order parameter and non-interacting Hamiltonian, respectively, and $\hat{\Psi}^\dagger$ ($\hat{\Psi}$) are the Nambu spinors containing the single fermion creation (annihilation) operators for multiple bands (spin and orbital in our model for Sr_2RuO_4).

As detailed in [52], $\hat{\Delta}$ and \hat{h} will transform differently under a unitary transformation \mathcal{U} with matrix representation $\hat{d}(\mathcal{U})$, since they correspond to particle-hole and particle-particle terms, respectively. Therefore, they transform as

$$\begin{aligned} \hat{h}' &= \hat{d}^\dagger(\mathcal{U}) \hat{h} \hat{d}(\mathcal{U}) \\ \hat{\Delta}' &= \hat{d}^\dagger(\mathcal{U}) \hat{\Delta} \hat{d}^*(\mathcal{U}). \end{aligned} \quad (\text{D.2})$$

The Hamiltonian can be rewritten in matrix form by using the fermionic anticommutation relations as

$$\mathcal{H} = \frac{1}{2} \hat{\chi}^\dagger \hat{\mathcal{H}}^{\text{BdG}} \hat{\chi}, \quad \text{where} \quad \hat{\mathcal{H}}^{\text{BdG}} = \begin{pmatrix} \hat{h} & \hat{\Delta} \\ \hat{\Delta}^\dagger & -\hat{h}^T \end{pmatrix}. \quad (\text{D.3})$$

In the expression above, we have introduced the enlarged Nambu spinor $\hat{\chi}^\dagger = (\hat{\Psi}^\dagger \quad \hat{\Psi}^T)$ and have omitted the constant terms.

Under a unitary transformation, the Hamiltonian $\hat{\mathcal{H}}^{\text{BdG}}$ becomes

$$(\hat{\mathcal{H}}^{\text{BdG}})' = \hat{D}^\dagger(\mathcal{U}) \hat{\mathcal{H}}^{\text{BdG}} \hat{D}(\mathcal{U}). \quad (\text{D.4})$$

We can see that the matrix representation for this unitary transformation in Nambu space that leads to the correct transformations stated in equation (D.2) is given by

$$\hat{D}(\mathcal{U}) = \begin{pmatrix} \hat{d}(\mathcal{U}) & 0 \\ 0 & \hat{d}^*(\mathcal{U}) \end{pmatrix}. \quad (\text{D.5})$$

Including the description in both orbital and spin space, if we want to represent an element $g \in D_{4h}$, the matrix representation corresponds to

$$\hat{D}(g) = \begin{pmatrix} \hat{d}_\lambda(g)\hat{d}_\sigma(g) & 0 \\ 0 & \hat{d}_\lambda^*(g)\hat{d}_\sigma^*(g) \end{pmatrix} = \mathbb{1}_\tau \frac{\hat{d}_\lambda(g)\hat{d}_\sigma(g) + \hat{d}_\lambda^*(g)\hat{d}_\sigma^*(g)}{2} + \tau_z \frac{\hat{d}_\lambda(g)\hat{d}_\sigma(g) - \hat{d}_\lambda^*(g)\hat{d}_\sigma^*(g)}{2}, \quad (\text{D.6})$$

where the Pauli matrices and the identity 2×2 matrix $\{\mathbb{1}_\tau, \tau_x, \tau_y, \tau_z\}$ represent the basis for Nambu space.

At first sight, the full representation in Nambu space seems very involved. Nonetheless, here is where the notation $\hat{\Delta} = (\hat{\psi} + \hat{\mathbf{d}} \cdot \boldsymbol{\sigma})i\sigma_y \equiv \hat{\alpha}i\sigma_y$ becomes extremely convenient. If $i\sigma_y$ is absorbed into the spinor, the Hamiltonian can be written as

$$\mathcal{H} = \frac{1}{2} \hat{\chi}_1^\dagger \hat{\mathcal{H}}_1^{\text{BdG}} \hat{\chi}_1, \quad \text{where} \quad \hat{\mathcal{H}}_1^{\text{BdG}} = \begin{pmatrix} \hat{h} & \hat{\alpha} \\ \hat{\alpha}^\dagger & -\sigma_y \hat{h}^T \sigma_y \end{pmatrix}, \quad (\text{D.7})$$

where now the spinor is given by $\hat{\chi}^\dagger = (\hat{\Psi}^\dagger \quad -i\sigma_y \hat{\Psi}^T)$.

From equation (D.2), we can see that, under a unitary operation, $\hat{\alpha}$ transforms as

$$\hat{\alpha}' = \hat{d}^\dagger(\mathcal{U}) \hat{\alpha} \sigma_y \hat{d}^*(\mathcal{U}) \sigma_y. \quad (\text{D.8})$$

Thus, in this case, to obtain the correct form for the transformed Hamiltonian, the matrix representation for the unitary transformation corresponds to

$$\hat{D}'(\mathcal{U}) = \begin{pmatrix} \hat{d}(\mathcal{U}) & 0 \\ 0 & \sigma_y \hat{d}^*(\mathcal{U}) \sigma_y \end{pmatrix}. \quad (\text{D.9})$$

In the same way, adding explicitly the description in orbital and spin space and noticing that σ_y only acts in spin space, the matrix representation now leads to

$$\begin{aligned} \hat{D}'(g) &= \begin{pmatrix} \hat{d}_\lambda(g)\hat{d}_\sigma(g) & 0 \\ 0 & \hat{d}_\lambda^*(g)\sigma_y \hat{d}_\sigma^*(g)\sigma_y \end{pmatrix} \\ &= \mathbb{1}_\tau \frac{\hat{d}_\lambda(g)\hat{d}_\sigma(g) + \hat{d}_\lambda^*(g)\sigma_y \hat{d}_\sigma^*(g)\sigma_y}{2} + \tau_z \frac{\hat{d}_\lambda(g)\hat{d}_\sigma(g) - \hat{d}_\lambda^*(g)\sigma_y \hat{d}_\sigma^*(g)\sigma_y}{2}. \end{aligned} \quad (\text{D.10})$$

To simplify the expression above, we need to remember the matrices representing the different operations in the point group D_{4h} in orbital and spin space. On the one hand, from equation (5.49) we can observe that in our particular case all matrices in orbital space fulfill

$$d_\lambda^*(g) = d_\lambda(g) \quad (\text{D.11})$$

for all $g \in D_{4h}$, which means that the representations are real.

On the other hand, focusing on spin space, we recall the matrix representations written in equation (5.54). It can be easily checked that now the following condition is satisfied:

$$\sigma_y d_\sigma^*(g) \sigma_y = d_\sigma(g), \quad (\text{D.12})$$

again for all $g \in D_{4h}$.

Hence, the previous equation (D.10) can be simply rewritten as

$$\hat{D}'(g) = \mathbb{1}_\tau d_\lambda(g) d_\sigma(g). \quad (\text{D.13})$$

This form is extremely important since Nambu space will transform always as an A_{1g} irreducible representation. Recalling the product table in Appendix C, all IR will remain invariant under the product with A_{1g} . Consequently, we only need to focus on how orbital and spin space transform under the different point group operations.

Appendix E

Order parameter for further neighbors

In this section, we will include the derivation of the equation for the gap for the next-nearest neighbors up to the sixth neighbors. The representative basis functions found in each case is summarized in Tables 7.5, 7.6. The final expression including all neighbors is written in the main text, corresponding to equation (7.21).

Next-nearest neighbors

In this case, the pairing interactions in real space fulfill the following symmetries:

$$[V_{(1,1)}]_{\tilde{\mu}_j, \tilde{\mu}_l}^{\tilde{\mu}_i, \tilde{\mu}_k} = [V_{(-1,1)}]_{\tilde{\mu}_j, \tilde{\mu}_l}^{\tilde{\mu}_i, \tilde{\mu}_k} = [V_{(1,-1)}]_{\tilde{\mu}_j, \tilde{\mu}_l}^{\tilde{\mu}_i, \tilde{\mu}_k} = [V_{(-1,-1)}]_{\tilde{\mu}_j, \tilde{\mu}_l}^{\tilde{\mu}_i, \tilde{\mu}_k} \equiv [V^{2N}]_{\tilde{\mu}_j, \tilde{\mu}_l}^{\tilde{\mu}_i, \tilde{\mu}_k}. \quad (\text{E.1})$$

Therefore, including only second neighbors and taking the Fourier transform back to momentum space, equation (7.9) for the gap now corresponds to

$$\begin{aligned} [\Delta_{\mathbf{k}}^{2N}]_{\tilde{\mu}_j}^{\tilde{\mu}_i} &= \frac{1}{\mathcal{N}} \sum_{\mathbf{k}'} \sum_{\tilde{\mu}_k, \tilde{\mu}_l} \left\{ [V^{2N}]_{\tilde{\mu}_j, \tilde{\mu}_l}^{\tilde{\mu}_i, \tilde{\mu}_k} \left(e^{-i(k_x + k'_x + k_y + k'_y)} + e^{-i(-k_x - k'_x + k_y + k'_y)} \right) \right. \\ &\quad \left. + e^{-i(k_x + k'_x - k_y - k'_y)} + e^{i(k_x + k'_x + k_y + k'_y)} \right) \\ &\quad - [V^{2N}]_{\tilde{\mu}_j, \tilde{\mu}_k}^{\tilde{\mu}_i, \tilde{\mu}_l} \left(e^{-i(k_x - k'_x + k_y - k'_y)} + e^{-i(-k_x + k'_x + k_y - k'_y)} \right) \\ &\quad \left. + e^{-i(k_x - k'_x - k_y + k'_y)} + e^{i(k_x - k'_x + k_y - k'_y)} \right\} \langle \hat{c}_{-\mathbf{k}'\tilde{\mu}_l} \hat{c}_{\mathbf{k}'\tilde{\mu}_k} \rangle. \end{aligned} \quad (\text{E.2})$$

Likewise, this equation can also be written in terms of the cosine functions as

$$\begin{aligned} [\Delta_{\mathbf{k}}^{2N}]_{\tilde{\mu}_j}^{\tilde{\mu}_i} &= \frac{1}{\mathcal{N}} \sum_{\mathbf{k}'} \sum_{\tilde{\mu}_k, \tilde{\mu}_l} \left\{ [V^{2N}]_{\tilde{\mu}_j, \tilde{\mu}_l}^{\tilde{\mu}_i, \tilde{\mu}_k} 4 \cos(k_x + k'_x) \cos(k_y + k'_y) \right. \\ &\quad \left. - [V^{2N}]_{\tilde{\mu}_j, \tilde{\mu}_k}^{\tilde{\mu}_i, \tilde{\mu}_l} 4 \cos(k_x - k'_x) \cos(k_y - k'_y) \right\} \langle \hat{c}_{-\mathbf{k}'\tilde{\mu}_l} \hat{c}_{\mathbf{k}'\tilde{\mu}_k} \rangle. \end{aligned} \quad (\text{E.3})$$

To rewrite it with separate terms corresponding to different IR, we can rewrite the cosines of a sum and difference. After some manipulation, it can be expressed as

$$\begin{aligned}
[\Delta_{\mathbf{k}}^{2N}]_{\tilde{\mu}_j}^{\tilde{\mu}_i} &= \frac{1}{\mathcal{N}} \sum_{\mathbf{k}'} \sum_{\tilde{\mu}_k, \tilde{\mu}_l} \left\{ \left([V^{2N}]_{\tilde{\mu}_j, \tilde{\mu}_l}^{\tilde{\mu}_i, \tilde{\mu}_k} - [V^{2N}]_{\tilde{\mu}_j, \tilde{\mu}_k}^{\tilde{\mu}_i, \tilde{\mu}_l} \right) (2 \cos k_x \cos k'_x) (2 \cos k_y \cos k'_y) \right. \\
&\quad + \left([V^{2N}]_{\tilde{\mu}_j, \tilde{\mu}_l}^{\tilde{\mu}_i, \tilde{\mu}_k} - [V^{2N}]_{\tilde{\mu}_j, \tilde{\mu}_k}^{\tilde{\mu}_i, \tilde{\mu}_l} \right) (2 \sin k_x \sin k'_x) (2 \sin k_y \sin k'_y) \\
&\quad - \left([V^{2N}]_{\tilde{\mu}_j, \tilde{\mu}_k}^{\tilde{\mu}_i, \tilde{\mu}_l} + [V^{2N}]_{\tilde{\mu}_j, \tilde{\mu}_l}^{\tilde{\mu}_i, \tilde{\mu}_k} \right) (2 \cos k_x \cos k'_x) (2 \sin k_y \sin k'_y) \\
&\quad \left. - \left([V^{2N}]_{\tilde{\mu}_j, \tilde{\mu}_l}^{\tilde{\mu}_i, \tilde{\mu}_k} + [V^{2N}]_{\tilde{\mu}_j, \tilde{\mu}_k}^{\tilde{\mu}_i, \tilde{\mu}_l} \right) (2 \sin k_x \sin k'_x) (2 \cos k_y \cos k'_y) \right\} \langle \hat{c}_{-\mathbf{k}'\tilde{\mu}_l} \hat{c}_{\mathbf{k}'\tilde{\mu}_k} \rangle, \quad (\text{E.4})
\end{aligned}$$

so that we finally obtain

$$\begin{aligned}
[\Delta_{\mathbf{k}}^{2N}]_{\tilde{\mu}_j}^{\tilde{\mu}_i} &= \frac{1}{\mathcal{N}} \sum_{\mathbf{k}'} \sum_{\tilde{\mu}_k, \tilde{\mu}_l} \left\{ [2 \cos k_x \cos k_y] \left[\left([V^{2N}]_{\tilde{\mu}_j, \tilde{\mu}_l}^{\tilde{\mu}_i, \tilde{\mu}_k} - [V^{2N}]_{\tilde{\mu}_j, \tilde{\mu}_k}^{\tilde{\mu}_i, \tilde{\mu}_l} \right) 2 \cos k'_x \cos k'_y \right] \right. \\
&\quad + [2 \sin k_x \sin k_y] \left[\left([V^{2N}]_{\tilde{\mu}_j, \tilde{\mu}_l}^{\tilde{\mu}_i, \tilde{\mu}_k} - [V^{2N}]_{\tilde{\mu}_j, \tilde{\mu}_k}^{\tilde{\mu}_i, \tilde{\mu}_l} \right) 2 \sin k'_x \sin k'_y \right] \\
&\quad - [2i \sin k_x \cos k_y] \left[\left([V^{2N}]_{\tilde{\mu}_j, \tilde{\mu}_l}^{\tilde{\mu}_i, \tilde{\mu}_k} + [V^{2N}]_{\tilde{\mu}_j, \tilde{\mu}_k}^{\tilde{\mu}_i, \tilde{\mu}_l} \right) (-2i) \sin k'_x \cos k'_y \right] \\
&\quad \left. - [2i \sin k_y \cos k_x] \left[\left([V^{2N}]_{\tilde{\mu}_j, \tilde{\mu}_l}^{\tilde{\mu}_i, \tilde{\mu}_k} + [V^{2N}]_{\tilde{\mu}_j, \tilde{\mu}_k}^{\tilde{\mu}_i, \tilde{\mu}_l} \right) (-2i) \sin k'_y \cos k'_x \right] \right\} \langle \hat{c}_{-\mathbf{k}'\tilde{\mu}_l} \hat{c}_{\mathbf{k}'\tilde{\mu}_k} \rangle. \quad (\text{E.5})
\end{aligned}$$

Notice that the factors of 2 inside the basis functions in front of each term are necessary in order to fulfill the normalization condition $\frac{1}{\mathcal{N}} \sum_{\mathbf{k}} (g_{\mathbf{k}}^{\Gamma})^* g_{\mathbf{k}}^{\Gamma'} = \delta_{\Gamma, \Gamma'}$.

In this case, the identification of each IR becomes more involved. With this purpose, we can Fourier transform back to real space, and consider the basis functions up to second nearest neighbors. For instance, we can focus on the example $\sin k_x \sin k_y$. Expanding the sine functions and considering only second order terms,

$$\sin k_x \sin k_y \xrightarrow{\text{2nd order}} k_x k_y \xrightarrow{\text{Real space}} xy. \quad (\text{E.6})$$

Considering the character table for the group D_{4h} in C.1, we can see that this form factor transforms as the B_{2g} irreducible representation under all group operations. Identical analysis can be done for all basis functions. Therefore, as summarized in Table 7.5, the form factors by order of appearance in the previous expression correspond to the A_{1g} , B_{2g} , E_{xu} , E_{yu} irreducible representations.

Third neighbors

Similarly to the first neighbors case, the symmetry in the interactions corresponds to

$$\begin{aligned}
[V_{(2,0)}]_{\tilde{\mu}_j, \tilde{\mu}_l}^{\tilde{\mu}_i, \tilde{\mu}_k} &= [V_{(-2,0)}]_{\tilde{\mu}_j, \tilde{\mu}_l}^{\tilde{\mu}_i, \tilde{\mu}_k} \equiv [V_x^{3N}]_{\tilde{\mu}_j, \tilde{\mu}_l}^{\tilde{\mu}_i, \tilde{\mu}_k} \\
[V_{(0,2)}]_{\tilde{\mu}_j, \tilde{\mu}_l}^{\tilde{\mu}_i, \tilde{\mu}_k} &= [V_{(0,-2)}]_{\tilde{\mu}_j, \tilde{\mu}_l}^{\tilde{\mu}_i, \tilde{\mu}_k} \equiv [V_y^{3N}]_{\tilde{\mu}_j, \tilde{\mu}_l}^{\tilde{\mu}_i, \tilde{\mu}_k}. \quad (\text{E.7})
\end{aligned}$$

The procedure to write the equation for the gap is analogous to the first neighbors case, so that equation (7.18) now reads

$$\begin{aligned}
[\Delta_{\mathbf{k}}^{3N}]_{\tilde{\mu}_j}^{\tilde{\mu}_i} = & \frac{1}{\mathcal{N}} \sum_{\mathbf{k}'} \sum_{\tilde{\mu}_k, \tilde{\mu}_l} \langle \hat{c}_{-\mathbf{k}'} \tilde{\mu}_l \hat{c}_{\mathbf{k}'} \tilde{\mu}_k \rangle \left\{ -[i\sqrt{2} \sin 2k_y] \left[-i\sqrt{2} \left([V_y^{3N}]_{\tilde{\mu}_j, \tilde{\mu}_l}^{\tilde{\mu}_i, \tilde{\mu}_k} + [V_y^{3N}]_{\tilde{\mu}_j, \tilde{\mu}_k}^{\tilde{\mu}_i, \tilde{\mu}_l} \right) \sin 2k'_y \right] \right. \\
& - [i\sqrt{2} \sin 2k_x] \left[-i\sqrt{2} \left([V_x^{3N}]_{\tilde{\mu}_j, \tilde{\mu}_l}^{\tilde{\mu}_i, \tilde{\mu}_k} + [V_x^{3N}]_{\tilde{\mu}_j, \tilde{\mu}_k}^{\tilde{\mu}_i, \tilde{\mu}_l} \right) \sin 2k'_x \right] \\
& + [\cos 2k_x + \cos 2k_y] \left[\left([V_x^{3N}]_{\tilde{\mu}_j, \tilde{\mu}_l}^{\tilde{\mu}_i, \tilde{\mu}_k} - [V_x^{3N}]_{\tilde{\mu}_j, \tilde{\mu}_k}^{\tilde{\mu}_i, \tilde{\mu}_l} \right) \cos 2k'_x \right. \\
& + \left. \left([V_y^{3N}]_{\tilde{\mu}_j, \tilde{\mu}_l}^{\tilde{\mu}_i, \tilde{\mu}_k} - [V_y^{3N}]_{\tilde{\mu}_j, \tilde{\mu}_k}^{\tilde{\mu}_i, \tilde{\mu}_l} \right) \cos 2k'_y \right] \\
& + [\cos 2k_x - \cos 2k_y] \left[\left([V_x^{3N}]_{\tilde{\mu}_j, \tilde{\mu}_l}^{\tilde{\mu}_i, \tilde{\mu}_k} - [V_x^{3N}]_{\tilde{\mu}_j, \tilde{\mu}_k}^{\tilde{\mu}_i, \tilde{\mu}_l} \right) \cos 2k'_x \right. \\
& \left. - \left([V_y^{3N}]_{\tilde{\mu}_j, \tilde{\mu}_l}^{\tilde{\mu}_i, \tilde{\mu}_k} - [V_y^{3N}]_{\tilde{\mu}_j, \tilde{\mu}_k}^{\tilde{\mu}_i, \tilde{\mu}_l} \right) \cos 2k'_y \right] \left. \right\}. \tag{E.8}
\end{aligned}$$

We can observe that these form factors correspond to higher harmonics of the first neighbors case, and thus the corresponding irreducible representations would be the same, as shown in Table 7.5.

Fourth neighbors

In this case, from Figure 7.1 we can see that to account for all fourth neighbors we must include both the purple and the green dots. It has been checked that now the purple neighbors fulfill the symmetries for the real space pairing interaction given by

$$[V_{(2,1)}]_{\tilde{\mu}_j, \tilde{\mu}_l}^{\tilde{\mu}_i, \tilde{\mu}_k} = [V_{(-2,1)}]_{\tilde{\mu}_j, \tilde{\mu}_l}^{\tilde{\mu}_i, \tilde{\mu}_k} = [V_{(2,-1)}]_{\tilde{\mu}_j, \tilde{\mu}_l}^{\tilde{\mu}_i, \tilde{\mu}_k} = [V_{(-2,-1)}]_{\tilde{\mu}_j, \tilde{\mu}_l}^{\tilde{\mu}_i, \tilde{\mu}_k} \equiv [V_{x2}^{4N}]_{\tilde{\mu}_j, \tilde{\mu}_l}^{\tilde{\mu}_i, \tilde{\mu}_k}, \tag{E.9}$$

whereas for the green neighbors we will have a different pairing interaction,

$$[V_{(1,2)}]_{\tilde{\mu}_j, \tilde{\mu}_l}^{\tilde{\mu}_i, \tilde{\mu}_k} = [V_{(-1,2)}]_{\tilde{\mu}_j, \tilde{\mu}_l}^{\tilde{\mu}_i, \tilde{\mu}_k} = [V_{(1,-2)}]_{\tilde{\mu}_j, \tilde{\mu}_l}^{\tilde{\mu}_i, \tilde{\mu}_k} = [V_{(-1,-2)}]_{\tilde{\mu}_j, \tilde{\mu}_l}^{\tilde{\mu}_i, \tilde{\mu}_k} \equiv [V_{x1}^{4N}]_{\tilde{\mu}_j, \tilde{\mu}_l}^{\tilde{\mu}_i, \tilde{\mu}_k}. \tag{E.10}$$

Including only the fourth neighbors, the symmetrized pairing interaction derivation is similar to the next-nearest neighbors case, except that now we will need to add eight neighbors. Therefore, in this case the equation for the gap in momentum space is given by

$$\begin{aligned}
[\Delta_{\mathbf{k}}^{4N}]_{\tilde{\mu}_j}^{\tilde{\mu}_i} = & \frac{1}{\mathcal{N}} \sum_{\mathbf{k}'} \sum_{\tilde{\mu}_k, \tilde{\mu}_l} \left\{ [V_{x2}^{4N}]_{\tilde{\mu}_j, \tilde{\mu}_l}^{\tilde{\mu}_i, \tilde{\mu}_k} 4 \cos(2k_x + 2k'_x) \cos(k_y + k'_y) \right. \\
& - [V_{x2}^{4N}]_{\tilde{\mu}_j, \tilde{\mu}_k}^{\tilde{\mu}_i, \tilde{\mu}_l} 4 \cos(2k_x - 2k'_x) \cos(k_y - k'_y) \\
& + [V_{x1}^{4N}]_{\tilde{\mu}_j, \tilde{\mu}_l}^{\tilde{\mu}_i, \tilde{\mu}_k} 4 \cos(k_x + k'_x) \cos(2k_y + 2k'_y) \\
& \left. - [V_{x1}^{4N}]_{\tilde{\mu}_j, \tilde{\mu}_k}^{\tilde{\mu}_i, \tilde{\mu}_l} 4 \cos(k_x - k'_x) \cos(2k_y - 2k'_y) \right\} \langle \hat{c}_{-\mathbf{k}'} \tilde{\mu}_l \hat{c}_{\mathbf{k}'} \tilde{\mu}_k \rangle. \tag{E.11}
\end{aligned}$$

This can be rewritten in terms of the basis functions for the different irreducible representations, leading to

$$\begin{aligned}
[\Delta_{\mathbf{k}}^{4N}]_{\tilde{\mu}_j}^{\tilde{\mu}_i} &= \frac{1}{\mathcal{N}} \sum_{\mathbf{k}'} \sum_{\tilde{\mu}_k, \tilde{\mu}_l} \left\{ [\sqrt{2} \cos 2k_x \cos k_y + \sqrt{2} \cos k_x \cos 2k_y] \right. \\
&\times \left[\left([V_{x2}^{4N}]_{\tilde{\mu}_j, \tilde{\mu}_l}^{\tilde{\mu}_i, \tilde{\mu}_k} - [V_{x2}^{4N}]_{\tilde{\mu}_j, \tilde{\mu}_k}^{\tilde{\mu}_i, \tilde{\mu}_l} \right) \sqrt{2} \cos 2k'_x \cos k'_y + \left([V_{x1}^{4N}]_{\tilde{\mu}_j, \tilde{\mu}_l}^{\tilde{\mu}_i, \tilde{\mu}_k} - [V_{x1}^{4N}]_{\tilde{\mu}_j, \tilde{\mu}_k}^{\tilde{\mu}_i, \tilde{\mu}_l} \right) \sqrt{2} \cos k'_x \cos 2k'_y \right] \\
&+ [\sqrt{2} \cos 2k_x \cos k_y - \sqrt{2} \cos k_x \cos 2k_y] \\
&\times \left[\left([V_{x2}^{4N}]_{\tilde{\mu}_j, \tilde{\mu}_l}^{\tilde{\mu}_i, \tilde{\mu}_k} - [V_{x2}^{4N}]_{\tilde{\mu}_j, \tilde{\mu}_k}^{\tilde{\mu}_i, \tilde{\mu}_l} \right) \sqrt{2} \cos 2k'_x \cos k'_y - \left([V_{x1}^{4N}]_{\tilde{\mu}_j, \tilde{\mu}_l}^{\tilde{\mu}_i, \tilde{\mu}_k} - [V_{x1}^{4N}]_{\tilde{\mu}_j, \tilde{\mu}_k}^{\tilde{\mu}_i, \tilde{\mu}_l} \right) \sqrt{2} \cos k'_x \cos 2k'_y \right] \\
&+ [\sqrt{2} \sin 2k_x \sin k_y + \sqrt{2} \sin k_x \sin 2k_y] \\
&\times \left[\left([V_{x2}^{4N}]_{\tilde{\mu}_j, \tilde{\mu}_l}^{\tilde{\mu}_i, \tilde{\mu}_k} - [V_{x2}^{4N}]_{\tilde{\mu}_j, \tilde{\mu}_k}^{\tilde{\mu}_i, \tilde{\mu}_l} \right) \sqrt{2} \sin 2k'_x \sin k'_y + \left([V_{x1}^{4N}]_{\tilde{\mu}_j, \tilde{\mu}_l}^{\tilde{\mu}_i, \tilde{\mu}_k} - [V_{x1}^{4N}]_{\tilde{\mu}_j, \tilde{\mu}_k}^{\tilde{\mu}_i, \tilde{\mu}_l} \right) \sqrt{2} \sin k'_x \sin 2k'_y \right] \\
&+ [\sqrt{2} \sin 2k_x \sin k_y - \sqrt{2} \sin k_x \sin 2k_y] \\
&\times \left[\left([V_{x2}^{4N}]_{\tilde{\mu}_j, \tilde{\mu}_l}^{\tilde{\mu}_i, \tilde{\mu}_k} - [V_{x2}^{4N}]_{\tilde{\mu}_j, \tilde{\mu}_k}^{\tilde{\mu}_i, \tilde{\mu}_l} \right) \sqrt{2} \sin 2k'_x \sin k'_y - \left([V_{x1}^{4N}]_{\tilde{\mu}_j, \tilde{\mu}_l}^{\tilde{\mu}_i, \tilde{\mu}_k} - [V_{x1}^{4N}]_{\tilde{\mu}_j, \tilde{\mu}_k}^{\tilde{\mu}_i, \tilde{\mu}_l} \right) \sqrt{2} \sin k'_x \sin 2k'_y \right] \\
&- [2i \sin k_x \cos 2k_y] \left[\left([V_{x1}^{4N}]_{\tilde{\mu}_j, \tilde{\mu}_l}^{\tilde{\mu}_i, \tilde{\mu}_k} + [V_{x1}^{4N}]_{\tilde{\mu}_j, \tilde{\mu}_k}^{\tilde{\mu}_i, \tilde{\mu}_l} \right) (-2i \sin k'_x \cos 2k'_y) \right] \\
&- [2i \sin k_y \cos 2k_x] \left[\left([V_{x2}^{4N}]_{\tilde{\mu}_j, \tilde{\mu}_l}^{\tilde{\mu}_i, \tilde{\mu}_k} + [V_{x2}^{4N}]_{\tilde{\mu}_j, \tilde{\mu}_k}^{\tilde{\mu}_i, \tilde{\mu}_l} \right) (-2i \sin k'_y \cos 2k'_x) \right] \\
&- [2i \sin 2k_x \cos k_y] \left[\left([V_{x2}^{4N}]_{\tilde{\mu}_j, \tilde{\mu}_l}^{\tilde{\mu}_i, \tilde{\mu}_k} + [V_{x2}^{4N}]_{\tilde{\mu}_j, \tilde{\mu}_k}^{\tilde{\mu}_i, \tilde{\mu}_l} \right) (-2i \sin 2k'_x \cos k'_y) \right] \\
&- [2i \sin 2k_y \cos k_x] \left[\left([V_{x1}^{4N}]_{\tilde{\mu}_j, \tilde{\mu}_l}^{\tilde{\mu}_i, \tilde{\mu}_k} + [V_{x1}^{4N}]_{\tilde{\mu}_j, \tilde{\mu}_k}^{\tilde{\mu}_i, \tilde{\mu}_l} \right) (-2i \sin 2k'_y \cos k'_x) \right] \left. \right\} \langle \hat{c}_{-\mathbf{k}'\tilde{\mu}_l} \hat{c}_{\mathbf{k}'\tilde{\mu}_k} \rangle. \quad (\text{E.12})
\end{aligned}$$

The correspondence between the IR and the basis functions is also summarized in Table 7.6. Notice that the A_{2g} irreducible representation basis function $\sqrt{2} \sin 2k_x \sin k_y - \sqrt{2} \sin k_x \sin 2k_y$ can also be expressed in the more familiar way $2\sqrt{2}(\cos k_x - \cos k_y) \sin k_x \sin k_y$, which is the basis function commonly associated to the g-wave superconducting phase.

Fifth neighbors

Recalling again Figure 7.1, we can see that the basis functions for the fifth neighbors would correspond to higher harmonics of the next-nearest neighbors case. Therefore, since the symmetry

$$[V_{(2,2)}]_{\tilde{\mu}_j, \tilde{\mu}_l}^{\tilde{\mu}_i, \tilde{\mu}_k} = [V_{(-2,2)}]_{\tilde{\mu}_j, \tilde{\mu}_l}^{\tilde{\mu}_i, \tilde{\mu}_k} = [V_{(2,-2)}]_{\tilde{\mu}_j, \tilde{\mu}_l}^{\tilde{\mu}_i, \tilde{\mu}_k} = [V_{(-2,-2)}]_{\tilde{\mu}_j, \tilde{\mu}_l}^{\tilde{\mu}_i, \tilde{\mu}_k} \equiv [V^{5N}]_{\tilde{\mu}_j, \tilde{\mu}_l}^{\tilde{\mu}_i, \tilde{\mu}_k}, \quad (\text{E.13})$$

is still preserved for the interactions in real space, similar to equation (E.5) the expression for the gap can be written as

$$\begin{aligned}
[\Delta_{\mathbf{k}}^{5N}]_{\tilde{\mu}_j}^{\tilde{\mu}_i} &= \frac{1}{\mathcal{N}} \sum_{\mathbf{k}'} \sum_{\tilde{\mu}_k, \tilde{\mu}_l} \left\{ [2 \cos 2k_x \cos 2k_y] \left[\left([V^{5N}]_{\tilde{\mu}_j, \tilde{\mu}_l}^{\tilde{\mu}_i, \tilde{\mu}_k} - [V^{5N}]_{\tilde{\mu}_j, \tilde{\mu}_k}^{\tilde{\mu}_i, \tilde{\mu}_l} \right) 2 \cos 2k'_x \cos 2k'_y \right] \right. \\
&+ [2 \sin 2k_x \sin 2k_y] \left[\left([V^{5N}]_{\tilde{\mu}_j, \tilde{\mu}_l}^{\tilde{\mu}_i, \tilde{\mu}_k} - [V^{5N}]_{\tilde{\mu}_j, \tilde{\mu}_k}^{\tilde{\mu}_i, \tilde{\mu}_l} \right) 2 \sin 2k'_x \sin 2k'_y \right] \\
&- [2i \sin 2k_x \cos 2k_y] \left[\left([V^{5N}]_{\tilde{\mu}_j, \tilde{\mu}_l}^{\tilde{\mu}_i, \tilde{\mu}_k} + [V^{5N}]_{\tilde{\mu}_j, \tilde{\mu}_k}^{\tilde{\mu}_i, \tilde{\mu}_l} \right) (-2i) \sin 2k'_x \cos 2k'_y \right] \\
&- [2i \sin 2k_y \cos 2k_x] \left[\left([V^{5N}]_{\tilde{\mu}_j, \tilde{\mu}_l}^{\tilde{\mu}_i, \tilde{\mu}_k} + [V^{5N}]_{\tilde{\mu}_j, \tilde{\mu}_k}^{\tilde{\mu}_i, \tilde{\mu}_l} \right) (-2i) \sin 2k'_y \cos 2k'_x \right] \left. \right\} \langle \hat{c}_{-\mathbf{k}'\tilde{\mu}_l} \hat{c}_{\mathbf{k}'\tilde{\mu}_k} \rangle. \quad (\text{E.14})
\end{aligned}$$

The irreducible representation corresponding to each basis function is shown in Table 7.6.

Sixth neighbors

In the same way, the sixth neighbors interaction potentials in real space fulfill

$$\begin{aligned} [V(3,0)]_{\tilde{\mu}_j, \tilde{\mu}_l}^{\tilde{\mu}_i, \tilde{\mu}_k} &= [V(-3,0)]_{\tilde{\mu}_j, \tilde{\mu}_l}^{\tilde{\mu}_i, \tilde{\mu}_k} \equiv [V_x^{6N}]_{\tilde{\mu}_j, \tilde{\mu}_l}^{\tilde{\mu}_i, \tilde{\mu}_k}, \\ [V(0,3)]_{\tilde{\mu}_j, \tilde{\mu}_l}^{\tilde{\mu}_i, \tilde{\mu}_k} &= [V(0,-3)]_{\tilde{\mu}_j, \tilde{\mu}_l}^{\tilde{\mu}_i, \tilde{\mu}_k} \equiv [V_y^{6N}]_{\tilde{\mu}_j, \tilde{\mu}_l}^{\tilde{\mu}_i, \tilde{\mu}_k}. \end{aligned} \quad (\text{E.15})$$

Therefore, the basis functions would correspond to higher harmonics of the first and third neighbors case, as indicated in Table 7.6. Analogously to those two cases, the equation for the gap is given by

$$\begin{aligned} [\Delta_{\mathbf{k}}^{6N}]_{\tilde{\mu}_j}^{\tilde{\mu}_i} &= \frac{1}{\mathcal{N}} \sum_{\mathbf{k}'} \sum_{\tilde{\mu}_k, \tilde{\mu}_l} \langle \hat{c}_{-\mathbf{k}'\tilde{\mu}_l} \hat{c}_{\mathbf{k}'\tilde{\mu}_k} \rangle \left\{ -[i\sqrt{2} \sin 3k_y] \left[-i\sqrt{2} \left([V_y^{6N}]_{\tilde{\mu}_j, \tilde{\mu}_l}^{\tilde{\mu}_i, \tilde{\mu}_k} + [V_y^{6N}]_{\tilde{\mu}_j, \tilde{\mu}_k}^{\tilde{\mu}_i, \tilde{\mu}_l} \right) \sin 3k'_y \right] \right. \\ &\quad - [i\sqrt{2} \sin 3k_x] \left[-i\sqrt{2} \left([V_x^{6N}]_{\tilde{\mu}_j, \tilde{\mu}_l}^{\tilde{\mu}_i, \tilde{\mu}_k} + [V_x^{6N}]_{\tilde{\mu}_j, \tilde{\mu}_k}^{\tilde{\mu}_i, \tilde{\mu}_l} \right) \sin 3k'_x \right] \\ &\quad + [\cos 3k_x + \cos 3k_y] \left[\left([V_x^{6N}]_{\tilde{\mu}_j, \tilde{\mu}_l}^{\tilde{\mu}_i, \tilde{\mu}_k} - [V_x^{6N}]_{\tilde{\mu}_j, \tilde{\mu}_k}^{\tilde{\mu}_i, \tilde{\mu}_l} \right) \cos 3k'_x + \left([V_y^{6N}]_{\tilde{\mu}_j, \tilde{\mu}_l}^{\tilde{\mu}_i, \tilde{\mu}_k} - [V_y^{6N}]_{\tilde{\mu}_j, \tilde{\mu}_k}^{\tilde{\mu}_i, \tilde{\mu}_l} \right) \cos 3k'_y \right] \\ &\quad \left. + [\cos 3k_x - \cos 3k_y] \left[\left([V_x^{6N}]_{\tilde{\mu}_j, \tilde{\mu}_l}^{\tilde{\mu}_i, \tilde{\mu}_k} - [V_x^{6N}]_{\tilde{\mu}_j, \tilde{\mu}_k}^{\tilde{\mu}_i, \tilde{\mu}_l} \right) \cos 3k'_x - \left([V_y^{6N}]_{\tilde{\mu}_j, \tilde{\mu}_l}^{\tilde{\mu}_i, \tilde{\mu}_k} - [V_y^{6N}]_{\tilde{\mu}_j, \tilde{\mu}_k}^{\tilde{\mu}_i, \tilde{\mu}_l} \right) \cos 3k'_y \right] \right\}. \end{aligned} \quad (\text{E.16})$$

Inclusion of the on-site interactions

Once the full picture with up to sixth neighbors is included, which corresponds to accounting for 28 neighbors, the on-site interactions must also be included to have a realistic model for Sr_2RuO_4 . However, since the interactions are repulsive, they are expected to destroy superconductivity, and it can only be stabilized by including the longer range attractive interactions. It is important to notice that the bare-interactions in equation (3.7) have to be added, as well as the on-site repulsion term originated from the spin-fluctuation pairing mechanism. As a consequence, for the on-site term, equation (7.9) can be written as

$$[\Delta^{\text{On-site}}]_{\tilde{\mu}_j}^{\tilde{\mu}_i} = \frac{1}{\mathcal{N}} \sum_{\mathbf{k}'} \sum_{\tilde{\mu}_k, \tilde{\mu}_l} \left([U]_{\tilde{\mu}_j, \tilde{\mu}_l}^{\tilde{\mu}_i, \tilde{\mu}_k} + [V(0)]_{\tilde{\mu}_j, \tilde{\mu}_l}^{\tilde{\mu}_i, \tilde{\mu}_k} - [V(0)]_{\tilde{\mu}_j, \tilde{\mu}_k}^{\tilde{\mu}_i, \tilde{\mu}_l} \right) \langle \hat{c}_{-\mathbf{k}'\tilde{\mu}_l} \hat{c}_{\mathbf{k}'\tilde{\mu}_k} \rangle. \quad (\text{E.17})$$

Since the on-site interaction term has no \mathbf{k} dependence, the corresponding form factor would be $g_{\mathbf{k}}^{\text{On-site}} = 1$, which trivially transforms as the A_{1g} irreducible representation.

Appendix F

Nodal structure for different Hund's couplings

In this Appendix, we will study the nodal structure for other Hund's coupling values. If we consider the case $J = 0$ meV, recalling Figure 8.5, the gaps corresponding to the spin-singlet and spin-triplet character are expected to have a similar energy. This is indeed what we observe in the projection of the gap on the Fermi surface (Figure F.1). Nonetheless, we also expect an almost identical contribution from the two dominant IRs, but when the contributions from all neighbors are summed the A_{1g} appears to be clearly dominant. If we compare the nodal structure with the case of $J = 12$ meV (Figure 8.8), for the dominant A_{1g} with spin singlet character the nodes in the α band are displaced now. On the contrary, for the dominant A_{1g} channel with spin triplet, nodes in the α band appear in the case $J = 0$ meV. The structure for the B_{1g} IR seems almost identical in both cases.

For completeness, the cases of $J = 24$ meV and $J = 36$ meV are also studied. Since for these Hund's couplings the spin-triplet character is almost suppressed and the B_{1g} component is smaller (see Figure 8.5), we can consider only the structure of the gap for the A_{1g} channel with spin singlet, shown in Figure F.2. For these two Hund's couplings, the nodal structure is similar to the case with $J = 12$ meV.

To understand the effect of the on-site interactions, it is also instructive to consider the leading spin-singlet irreducible representations in the case where they are not implemented, as shown in Figure F.3a, F.3b. When on-site interactions are included the order parameter is smaller, as expected since the strong on-site repulsion partially destroys superconductivity, although the leading irreducible representations are not modified. Focusing on the structure of the gap on the Fermi surface, interestingly in both cases the same nodes appear, even in the α band for the A_{1g} channel with spin-singlet character.

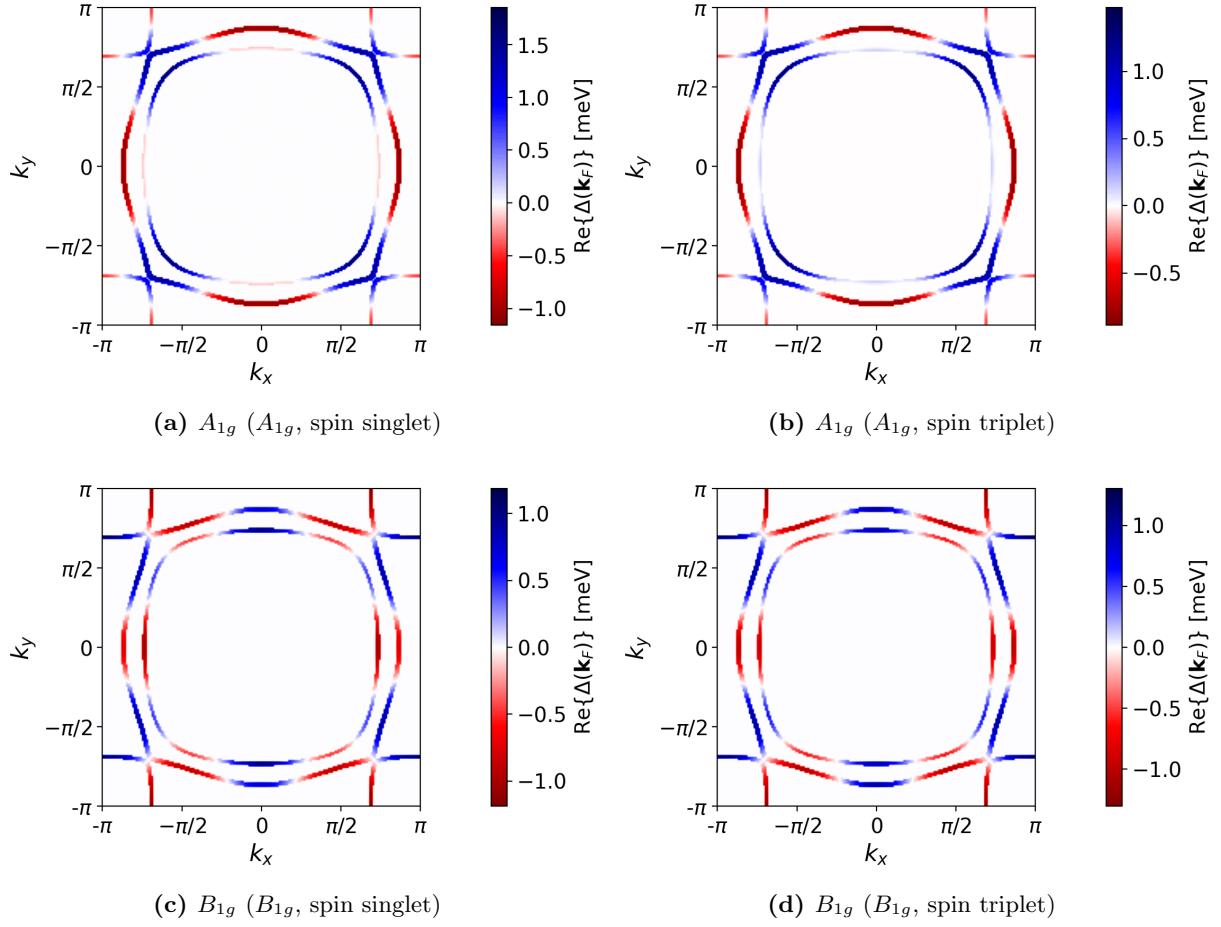


Figure F.1: Real part of the superconducting order parameter projected on the Fermi surface, where the color bar corresponds to the values of the gap. We consider $N = 81$, $k_B T = 0.01$ meV, $J = 0$ meV, $\lambda_{\text{SOC}} = 35$ meV and a boost $\alpha = 1.5$. The corresponding irreducible representation in momentum space is specified in each caption, and in parenthesis it is detailed the IR in orbital/spin space and the spin character of the particular channel.

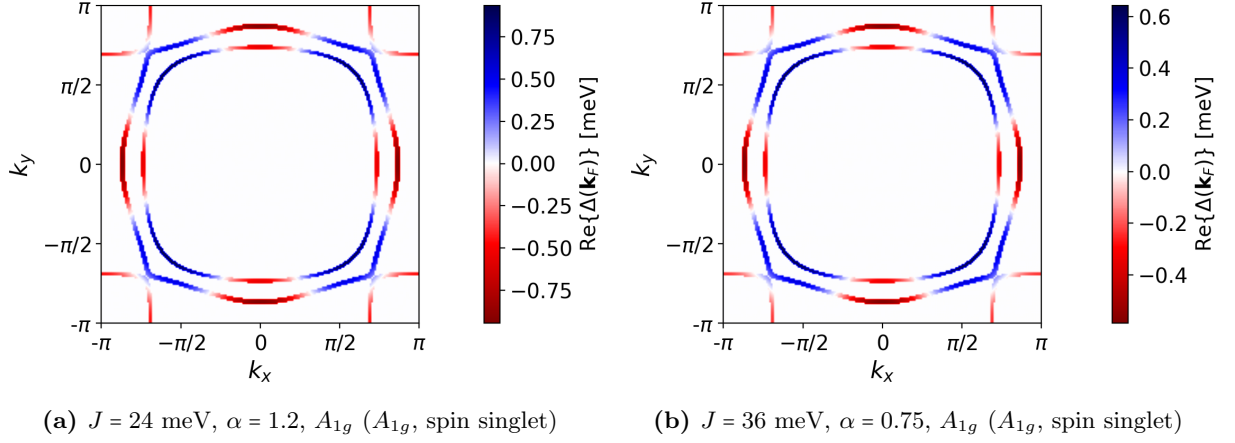


Figure F.2: Real part of the superconducting order parameter projected on the Fermi surface in the case where on-site interactions are not implemented, where the color bar corresponds to the values of the gap. We consider $N = 81$, $k_B T = 0.01$ meV, and $\lambda_{\text{SOC}} = 35$ meV in both cases, while the boost and the corresponding Hund's coupling value if specified in each caption. The irreducible representation in momentum space is also detailed, and in parenthesis it is included the IR in orbital/spin space and the spin character of the particular channel.

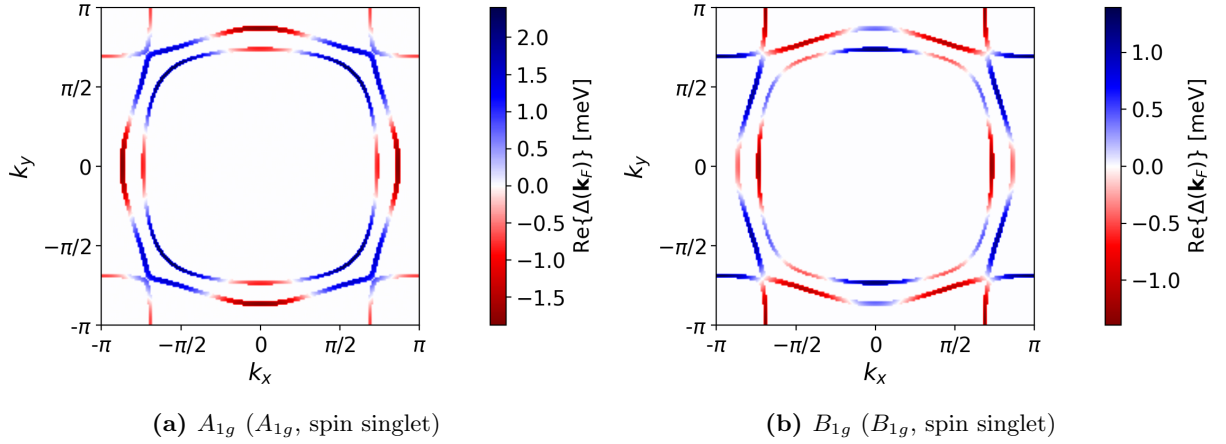


Figure F.3: Real part of the superconducting order parameter projected on the Fermi surface in the case where on-site interactions are not implemented, where the color bar corresponds to the values of the gap. We consider $N = 81$, $k_B T = 0.01$ meV, $J = 12$ meV, $\lambda_{\text{SOC}} = 35$ meV and a boost $\alpha = 1.7$. The corresponding irreducible representation in momentum space is specified in each caption, and in parenthesis it is detailed the IR in orbital/spin space and the spin character of the particular channel.